Master's Thesis in Physical Oceanography

Bottom melting of Arctic Sea Ice in the Nansen Basin due to Atlantic Water influence

Morven Muilwijk
May 2016

UNIVERSITY OF BERGEN
GEOPHYSICAL INSTITUTE

The figure on the front page illustrates the Research Vessel Lance drifting with the sea ice in the Arctic Ocean. Below the cold ocean surface layer a thick warm layer of Atlantic Water is found. Heat from this warm layer can potentially be mixed upward and possibly influence the sea ice cover.

Abstract

The hydrographic situation for a region north of Svalbard is investigated using observations from the Norwegian Young Sea Ice Cruise (N-ICE2015). Observations from January to June 2015 are compared to historical observations with a particular focus on the warm and salty Atlantic Water (AW) entering the Arctic Ocean through the Fram Strait. Here we discuss how the AW has changed over time, what governs its characteristics, and how it might influence the sea ice cover.

We find that AW characteristics north of Svalbard are mainly controlled by the distance along the inflow path, and by changes in inflowing AW temperature in the Fram Strait. AW characteristics north of Svalbard are also largely affected by local processes such as sea ice growth, melting and tidal induced mixing. Furthermore, one dimensional model results and observations show that AW has a direct impact on the sea ice cover north of Svalbard. Shallow and warm AW efficiently reduces sea ice growth and results in bottom melting throughout the whole year.

The historical observations and outcome from a fully coupled earth system model show a warming trend of AW core temperature over the last few decades. We believe that the AW warming trend in the Arctic Ocean may be part of long term multi-decadal variability, which is influenced by anthropogenic forcing. Simulations suggest that approximately 30 % of the recent warming may be attributed to global warming.

Acknowledgements

I would like to thank my supervisor Lars Henrik Smedsrud for all the good support, guidance, and inspiring discussions during the process of this thesis. It has been great working together on this project. I would also like to thank my co-supervisors Amelie Meyer and Ingrid Husøy Onarheim for valuable feedback, good ideas, and support when I needed it the most. I have learned a lot from you this last year and appreciate all the time and effort you have given me. A special thanks goes to Arild Sundfjord at the Norwegian Polar Institute for input and making it possible for me to participate in the N-ICE2015 project, and to join on the incredible voyage with R/V Lance north of Svalbard. This amazing fieldwork has been one of my life's greatest adventures so far.

Greetings to everybody with whom I was on the ship frozen into the ice, with whom I was looking for polar bears and with whom I got cold and wet feet during the cruise. A special greeting goes to H.R.H. Crown Prince Haakon and H.R.H. Crown Princess Mette-Marit who took the long journey to the Arctic to see the drastic changes with their own eyes, and who I hope felt safe while we guarded their tent on the ice during the night. Thank you Lisbeth Håvik for good company in the High North and for teaching me a lot about instrumentation and data handling. My thanks also go to Algot Peterson, Aleksi Nummelin and Helge Drange for helpful comments during the analysis of the results, and Pia Løtvedt for proofreading.

The two last years at GFI would not have been the same without the company of my great friends and study mates. Thanks for all the laughter, the joyful lunches, energetic hikes, blissful parties, skilful drone flying and endless discussions. Last but not least I would like to thank my girlfriend for standing by my side and my family who has always encouraged me to pursue my dreams.

This work is dedicated to all the children in this world who are not as fortunate to get a proper education and to learn about the beauty of nature.

Bergen, May 2016.

Contents

Chapter 1

Introduction

Global climate change and the "New Arctic"

The global climate system is warming; according to the United Nations Intergovernmental Panel on Climate Change (IPCC), each of the last three decades the earth's surface has been successively warmer than any preceding decade since 1850 (Solomon, 2007). A shrinking cryosphere with loss of Arctic sea ice remains one of the most visible signs of this warming. Sea ice trends are negative for all months and all regions of the Arctic (except the Bering Sea during winter) (Jeffries et al., 2013). The Arctic sea ice is thus one of the "canaries in the coal mine" showing that global climate change is real.

The sea ice plays an important role in the global climate system (Solomon, 2007). A critical feedback mechanism with far reaching consequences has taken effect: As white sea ice is replaced by darker ocean water, the water and air absorb more sunlight and heat up further during summer. This is known as the ice-albedo effect (Curry et al., 1995). The Arctic sea ice helps cool the planet, so its loss inevitably will affect the climate and weather beyond the Arctic itself (Grassi et al., 2013; Honda et al., 1996). Not only may sea ice loss have implications for the weather and climate, it will also have implications for ecosystems, policy, security, and economy (fisheries, oil industry, shipping, etc...) (Jeffries et al., 2013). The ice is also of high relevance due to freshwater content, its effect on ocean currents, and its role in ocean to atmosphere transfers of energy and gases like CO_2. It is clear that understanding the sea ice is important for understanding an important part of the global climate system.

The United Nations Intergovernmental Panel on Climate Change (IPCC) warned in 2007 that the impacts of climate change in the Arctic over the next century "will exceed the impacts forecast for many other regions and will produce feedbacks that will have globally significant consequences" (Parry, 2007). Nearly a decade later this sad forecast is already being borne out. The Arctic is at present probably the region which is most affected by climate change.

Since 1979, when continuous satellite records of sea ice began, the Arctic has lost more than half its volume of ice, which has been reduced, in both overall area and thickness (Comiso, 2012; Carmack et al., 2015). In September 2012 the minimum summer extent was just half the average during the 1980s and 1990s (Parkinson and Comiso, 2013). The decline from 1981 to 2010 is approximately 13.4 % per decade

(National Snow and Ice Data Centre, 2015). The sea ice system is also in transition from a system with thick multi year ice, where the ice survives several summers, to a system with thinner young ice, which melts every summer (Carmack et al., 2015). This young ice is mobile and breaks easier when storms occur. The Arctic has, as Jeffries et al. (2013) noted, entered a "new normal" state, "the new Arctic", with multiple impacts on oceanic, atmospheric, and terrestrial systems (Bhatt et al., 2014).

The causes of the sea ice loss are complex and involve many mechanisms (Jeffries et al., 2013). Most of the changes we observe in the Arctic, may be due to changes in the atmosphere but also partly due to changes in the ocean (Stroeve et al., 2011). However, regional differences are large in the Arctic, and in some areas, such as north of Svalbard, the ocean might play a larger role than in other regions (Onarheim et al., 2014).

Motivation: "Chasing the polar secrets"

Warm and salty Atlantic Water (AW) originating in the North Atlantic enters the Arctic Ocean through the Fram Strait and is present below the Arctic sea ice cover throughout the Arctic. This AW current, which is an extension of the Gulf Stream, flows north along the Norwegian coast, west of Svalbard, where it is called the West Spitsbergen Current, and finally enters the Arctic Ocean, carrying large amounts of heat. Along its flow path the AW loses heat to the atmosphere, to other water masses and to melting of sea ice. North of Svalbard, the AW is usually not in direct contact with the sea ice, but is separated from the surface by a cold, fresher layer of water. For the AW to melt sea ice, the heat must be mixed upwards or the AW must be close to the surface.

The depth of AW in the Arctic Ocean varies by region and over time. North of Svalbard, the depth is determined by a combination of:

(a) local processes: topography, distance to inflow, turbulent mixing and tidal mixing,

(b) the sea ice growth, freshwater forcing due to sea ice melt, volume and characteristics of ice imported to the area,

(c) and the changes in AW inflow characteristics.

Previously the AW entering through Fram Strait has been considered as less important because changes in the sea ice cover have mainly been connected to atmospheric forcing and greater inflow of Pacific Water through Bering Strait, and because of the strong stratification keeping the AW isolated below the sea ice (Alexeev et al., 2013). Conversely it is now suggested that AW has direct impact on melting of sea ice, especially in the region North of Svalbard (Onarheim et al., 2014; Alexeev et al., 2013; Zhang, 2015; Ivanov et al., 2016). The shrinking sea ice cover also allows an increased input of energy from wind, which potentially could assist in bringing AW heat to the surface (Peterson et al., in progress).

The AW temperature in the Arctic Ocean has increased in recent years (Polyakov et al., 2012). For example has the upper 50 - 200 m of the West Spitsbergen Current shown an overall AW warming since the mid-1960s (Alexeev et al., 2013). This warming

Figure 1.1: In Nansen's footsteps: N-ICE2015 is not the first Norwegian long polar expedition collecting oceanographic, atmospheric and biological data. It was inspired by the famous voyage of Fram by Fridtjof Nansen, who drifted across the Arctic Ocean from 1893 to 1896 in an attempt to reach the North Pole. Picture shows Nansen (second from the left) and his crew in front of Fram frozen into the sea ice. Photo from the National Library of Norway .

can either be due to natural variability on long time scales or reflect global warming and climate change. We assume that the sea ice and polar water above the AW are passively responding to the AW variability.

In this study we want to pursue the "secrets of the Atlantic Water", and investigate further how AW temperature and depth has changed over time and how it may affect the sea ice cover in the Nansen Basin north of Svalbard. Data were collected during the Norwegian Young Sea Ice Cruise (N-ICE2015), where the author spent almost four weeks on board of the research vessel R/V Lance in April 2015. The data collected during the cruise is the basis for this study, and hydrographic and current observations from a region north of Svalbard will be presented here. Model output from NorESM and a one-dimensional convection/sea ice growth model will also be discussed.

Extreme research investigating how Arctic sea ice is dwindling

N-ICE2015 is a research project which aims to understand the effects of the new, thin, first year sea ice regime in the Arctic on energy fluxes, sea ice dynamics and the associated ecosystem and global climate. To reach this goal, the Norwegian Polar Institute's research vessel R/V Lance was frozen into the ice north of Svalbard, providing exceptionally long time series of observations from mid-winter to early summer (Granskog et al., 2016). The vessel spent 111 days in the ice, tethered to different floes for several weeks at a time, collecting data altogether some 4000 nautical miles across a region north of Svalbard (Fig. 3.2). Most scientific cruises to the Arctic are conducted in summer, and winter observations are therefore sparse. The concept followed that of the famous Fram drift by Nansen (Fig. 1.1, Nansen (1902)), Russian drift stations, the Surface Heat Budget of the Arctic Ocean (SHEBA) campaign in the late 90s (Perovich

et al., 1999) and the Tara drift in 2007-2008 (Gascard et al., 2008), which all happened during a thicker ice regime (Granskog et al., 2016).

The scientific interest during the N-ICE2015 project were interdisciplinary, including physical oceanography, atmospheric science, sea ice physics and marine biochemistry. With this data, a better understanding of the whole air-ice-sea system will be possible (Granskog et al., 2016). Comparison with historical data shows that the new observations from January through June fill major gaps in available observations, and help describe important processes linking changes in regional AW heat transport and sea ice.

Hypothesis

In this study we investigate the hydrographic situation north of Svalbard during N-ICE2015, study how the AW has changed over time, understand what governs its characteristics and learn how it may influence the sea ice. We also want to find out which local processes affecting AW characteristics we can identify in the N-ICE2015 observations and in other data sets. Also, if we can identify changes in the AW over time, we want to find out how this may affect the sea ice growth and melt processes.

Hypothesis: AW characteristics north of Svalbard are partly controlled by local topography of the Yermak Plateau, partly by local processes, and by the characteristics of the inflowing AW through Fram Strait. AW at the inflow on the Yermak Plateau is becoming warmer, and further along its path north of Svalbard it is shoaling. The warming and shoaling of AW melts and limits sea ice growth in the area.

The thesis is divided into 6 chapters, where the first is the introduction. Chapter 2 describes all relevant background information, and chapter 3 the methods and data sets. In chapter 4 the results are presented and in chapter 5 these are discussed. Finally a summary of the findings and an outlook is given in chapter 6.

Chapter 2

Theoretical Background

2.1 The Arctic Ocean

The Arctic Ocean is the smallest and shallowest of the world's five major oceanic divisions, with a total area of approximately 9.4 million km^2 (4.3 % of total ocean area). Continental shelves constitute about one third of this area. The Arctic Ocean is an enclosed ocean, connected to the Pacific Ocean through the Bering Strait between Russia and Alaska, to the Atlantic Ocean through the Barents Sea and the Fram Strait between Greenland and Svalbard, and also through the Canadian Archipelago via the Baffin Bay (Fig. 2.1, Jakobsson (2002); Jones (2001); Rudels (2015)). The central Arctic Ocean is usually divided in two main basins; the Eurasian Basin on the Atlantic side and the Canadian Basin on the Pacific side, separated by the subsurface Lomonosov Ridge (Fig. 2.1). These two basins are each subdivided by less prominent ridges; the Nansen-Gakkel Ridge, which separates the Eurasian Basin into the Amundsen and Nansen basins, and the Alpha-Mendeleyev Ridge, separating the Canadian Basin into the Canada and Makarov basins. Average depth for the Arctic Ocean is approximately 1000 m. The Arctic Ocean includes the Barents, Kara, Chukchi, East Siberian, Beaufort and Laptev Seas. The only deep connection to the other world oceans is through the Fram Strait with a sill depth of 2600 m (Fig. 2.1, Jones (2001)). Throughout the year the Arctic Ocean is partly covered by sea ice. Perennial, multi year ice, historically covered 60 % of the ocean, but during the minima in 2007 and 2012, multi year ice only covered 30 % of the ocean (Comiso, 2012; NSIDC, 2013). The mean thickness of sea in the Arctic Ocean has decreased from 3-4 m to 1-2 m in time period from 1958 to 2008 (Kwok and Rothrock, 2009; Maslanik et al., 2007).

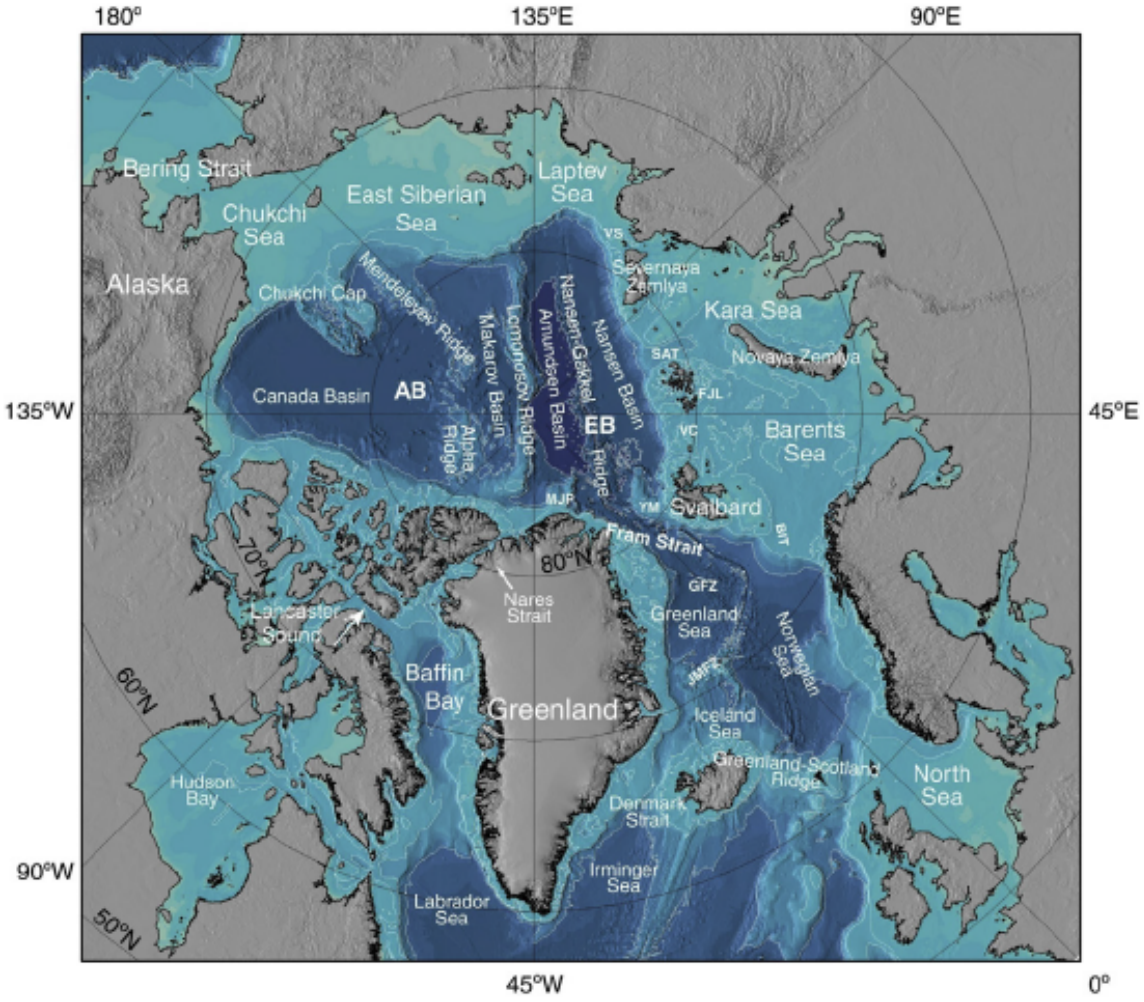

Figure 2.1: Overview map of the Arctic Ocean. From Rudels (2015)

2.2 A History of Polar Research in the Arctic Ocean

Oceanographic research in the Arctic Ocean has been limited throughout history due to the harsh environment and limited accessibility. However, early descriptions of sea ice exist in parts of the Arctic Ocean exist, and there is a very long history of whaling around Svalbard that goes back to the 1600s (van Linschoten, 1601). The first oceanographic observations in the Arctic Basin, and thus the first modern Arctic research, were done by Fridtjof Nansen in 1893-1896 during his famous voyage with Fram. Fram drifted almost three years with the pack ice in an attempt to reach the North Pole (Nansen, 1898).

Figure 2.2 shows a map of the Arctic Ocean made by Nansen in 1887, and a graph showing temperature and salinity sections from the Fram expedition. These sections show a cold and fresh surface layer overlying a warmer and saltier layer of AW below approximately 100 m. A lot of oceanographic research in the Arctic on sea ice and ocean boundary layer physics has its basis in a historic paper published in 1905 by Vagn Walfrid Ekman, who worked with Vilhelm Bjerknes and Fridtjof Nansen on a mathematical

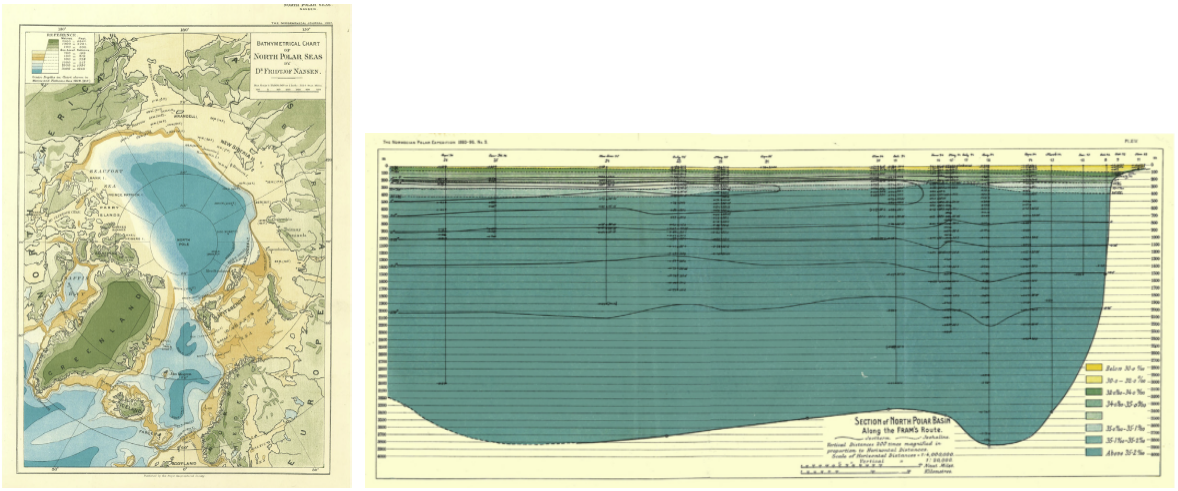

Figure 2.2: Map of the Arctic Mediterranean and a temperature (lines) and salinity (colours) section from the Fram expedition (1893-96). From Nansen (1902)

theory to explain Nansen's observations from the Fram expedition (Rudels, 2015).

The Soviet ice-breaker Sedov involuntarily almost repeated the drift of Fram between 1937 and 1940. In 1931 a famous attempt was made by Harald Sverdrup and Hubert Wilkins to reach the North Pole with the submarine Nautilus. Nautilus failed, but observations were gathered during the attempt (Sverdrup, 1931). Systematic oceanographic observations in the Arctic Ocean began in the 1930s, when Russia started the ice drift stations monitoring program (67 stations, Rudels (2015). After a gap in ship based observations the 1940s (10 stations), the first Soviet aircraft surveys that covered the basin were done (51 stations) in the 1950s. A few observations are available from the 1960s (32 stations). The 1970s were a period with many observations with seven Soviet aircraft surveys (204 stations). From these last decades, data from Soviet submarines have become available (Dmitrenko et al., 2008). Observations from the first Fram expedition, Harald Sverdrup's Nautilus mission in 1931, and Soviet climatological data will be used in comparisons further onwards in this thesis.

In the 1970s, satellites started to be used for remote sensing of oceanographic parameters, and also Arctic sea ice using passive microwave radiometers (Comiso, 2012). From the 1970s, several other countries (USA, Germany, Canada, and Norway) also started doing active research in the region, from this period on there are observational data available from ships within and around the Arctic Ocean from a number of expeditions. Compared to the other world-oceans, measurements in the Arctic Ocean are still sparse.

The contribution of ocean heat flux to the mass budget of Arctic sea ice was recognized by Maykut and Untersteiner (1971) more than 40 years ago. They ran a one dimensional thermodynamic model of sea ice, based on data from the drift of Ice Station Alpha in 1950/58. They found that in order to maintain energy balance they required a basin-averaged flux of heat from the ocean of 1-3 $\mathrm{W\,m^{-2}}$. This value is of comparable magnitude to the estimated heat transport related to the inflow from the Atlantic and Pacific through the Fram and the Bering Straits (Pnyushkov et al., 2015; Shimada

et al., 2006; Woodgate et al., 2012).

The ocean heat flux and many other oceanographic processes in the Arctic Ocean have been studied in detail over the past few decades, some of which will be presented, in the following chapters. However, determining the ocean's role in the evolution of the Arctic sea ice pack is difficult given the typically short field program and scarce historical data. Over recent years, there has been larger availability of measurements, not only from ships, but also from Ice Thethered Profiler (ITP), buoys, drifters, gliders, remote sensing and others. Still, access to the Arctic Ocean remains limited, including difficult logistics and restrictions related to territorial issues (Carmack et al., 2015).

2.3 Arctic Sea Ice

2.3.1 Characteristics and Recent Changes

Depending on the season, a large part of the Arctic Ocean is covered by sea ice. The ice cover in the Northern Hemisphere shows large seasonal variability, with sea ice extent varying from about $6 \cdot 10^6$ km^2 in summer to $15 \cdot 10^6$ km^2 in winter (Comiso, 2012). The Arctic Ocean with its $9.4 \cdot 10^6$ km^2 is almost completely ice covered throughout winter. The sea ice is relatively thin ($\sim$ 2 m) and appears sensitive to perturbations from ocean and atmosphere. Therefore changes in sea ice may be signs of climate change. Sea ice is to a large extent controlling fluxes of heat, moisture, and momentum at the ocean-atmosphere interface. Ice growth only occurs when the whole mixed layer has reached freezing temperature. Depending on wind stress and surface conditions, either frazil ice or congelation ice is formed. Further ice growth happens from below and is determined by the energy balance at the lower boundary. Sea ice melts from the top only if there is a positive heat gain from the atmosphere. It will melt from below if the oceanic heat flux exceeds the upward conductive heat flux. This bottom melting can arise because heat from deep down in the ocean, as for example warm AW, is mixed upwards, but also from warm solar heated surface waters advected under the ice (Eicken, 2003). Winds can push the ice into regions where there is more of this heat available. All together the factors that influence the Arctic sea ice cover are wind velocity, ocean heat flux, radiation, sensible and latent heat fluxes, currents and waves.

The global distribution of sea ice concentrations has been observed at 25 km resolution daily since October 1978 from satellite passive microwave sensing data (Comiso, 2012; Stammerjohn et al., 2012). In these studies one distinguishes between sea ice extent, which is defined as the sum of ice-covered areas with concentrations of 15 % or greater, and sea ice area, which is defined as the summarized product of the ice concentration and its area for each element within the ice extent (Carmack et al., 2015).

In recent years the Arctic sea ice pack has undergone large changes and has been shrinking dramatically. Data of monthly anomalies from November 1978 to December 2012 show an overall annual negative trend of 3.8 % in sea ice extent per decade (Carmack et al., 2015). Considering September values only (containing the annual sea ice extent minimum), and extending the record to September 2015, the rate is -13.4

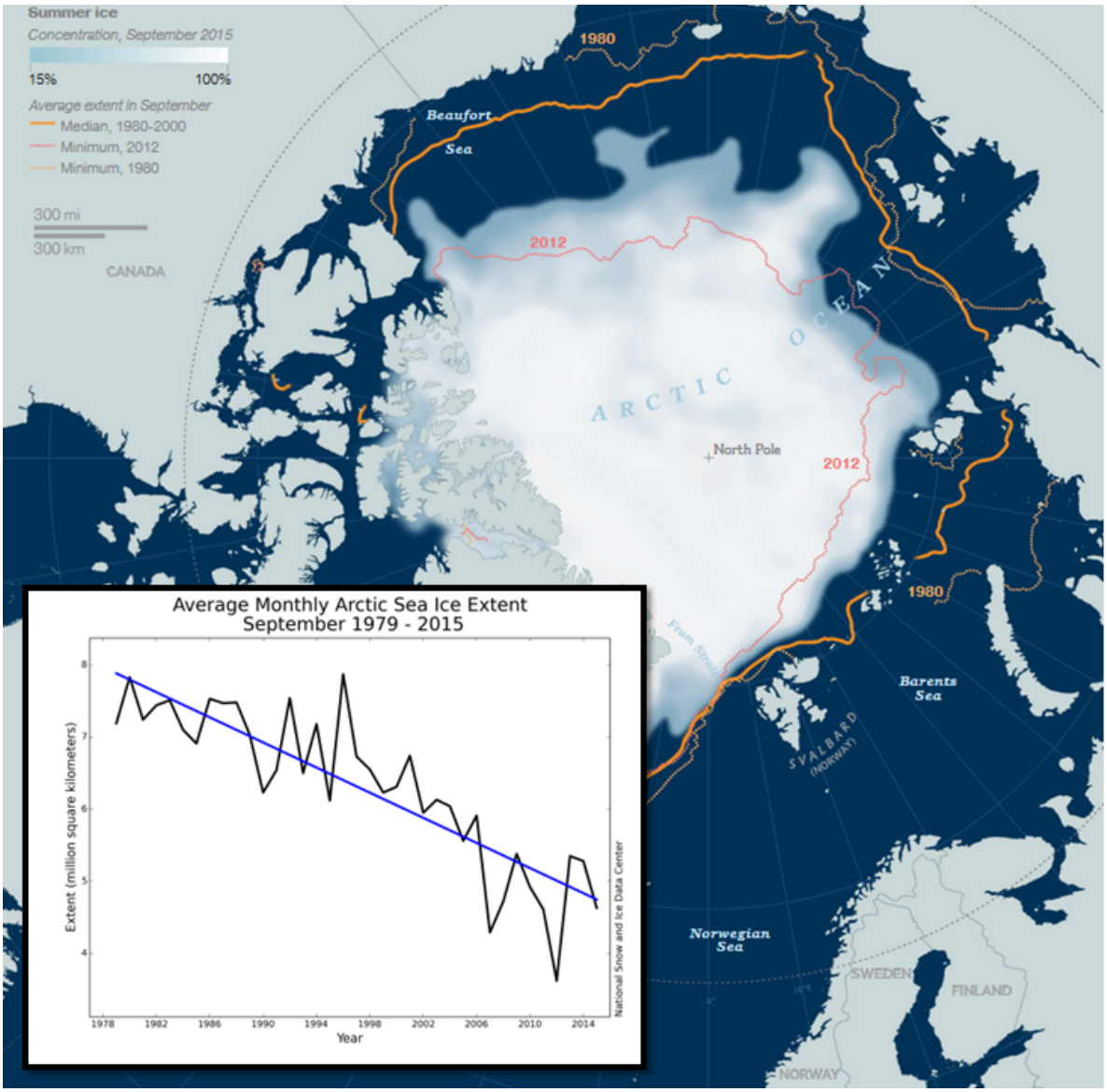

Figure 2.3: Map showing summer summer sea ice concentration (September) for 2015 compared to the mean sea ice extent (outer limit of area with at least 15 % ice) from 1980-2000 (thick yellow line), the minimum sea extent in 2012 (dashed orange line) and the minimum in 1980 (dashed yellow line). The inset shows the decline in monthly average September sea ice extent from 1979 to 2015 from satellite observations. From 1981 to 2015 the decline shown is 13.4 % per decade. Map courtesy National Geographic (`http://ngm.nationalgeographic.com/2016/01/arctic-ice-shrinking-graphic-environment-text`) and inset figure courtesy National Snow and Ice Data Center (`http://nsidc.org/arcticseaicenews/2015/10/2015-melt-season-in-review/`).

% per decade (Fig. 2.3). Looking at ice extent and area alone does not give a proper representation of the current situation and changes. One also has to look at changes in sea ice thickness and age. The sea ice is usually divided into categories related to its age, the most important categories being first year sea ice and perennial sea ice.

Perennial sea ice has survived at least one summer. The thick component of the perennial ice, called multi year ice, has its extent and area declining at an even more rapid rate of 15.1 % and 17.2 % per decade respectively (Comiso, 2012; NSIDC, 2013). This means that the average thickness of the Arctic sea ice cover is declining. This drastic change in perennial and multi year ice has been considered as an event that could trigger an irreversible change in the Arctic sea ice cover (Lindsay et al., 2009; Amstrup et al., 2010). The degradation of multi year ice has led to the existence of a seasonal ice cover over some areas in the Arctic Ocean after 2007 (Kwok and Rothrock, 2009; Ivanov and Watanabe, 2013). In general changes in the Arctic sea ice cover have been largest during summer. However, in three recent winters, 2012, 2013 and 2014, the ice concentrations along the AW pathway north-east of Svalbard have been extremely low. The ice covered area for the western Nansen Basin for February 2012-2014 was about 70 % of the average February value calculated for the 1979-2005 time interval (Ivanov et al., 2016).

The Arctic sea ice cover is strongly related to surface air temperatures, which are rising in the Arctic at about 3 times the global average (Ivanov et al., 2016). The sea ice cover is also weakly correlated to the Arctic Oscillation, as an indication of the main atmospheric circulation in the area (Comiso, 2012). An eight to nine year cycle is apparent in the multi year sea ice record. This could partly explain the slight increase in multi year ice extent in 2009-2011 (Comiso, 2012). Although extreme atmospheric forcing was likely an important driver of the reduction in 2007-2008 (Zhang et al., 2008), the ice loss would probably not have been so large if the ice pack had not already been weakened over the last decades. The sea ice reduction results from a complex interplay between the dynamics and thermodynamics of the atmosphere, sea ice and ocean (Polyakov et al., 2010). The ice-albedo feedback mechanism is considered to be the major feedback leading to accelerated warming in the Arctic (Perovich et al., 2007). This feedback is based on the fact that reduction of ice and snow leads to decreased albedo and then again further warming (Stouffer, 1980).

The satellite observations of sea ice concentration have uncertainties as high as ± 1 million km^2 (Ivanova et al., 2014). Measurements of thickness, and hence volume, rely on geophysical parameters that introduce large uncertainties. Ice draft data from submarines and upward-looking moored sonars (Rothrock et al., 2008; Kwok et al., 2009), together with estimates from satellite altimetry (Kwok et al., 2009; Laxon et al., 2013) and airborne electromagnetic sensing (Haas et al., 2010) show that the general overall thickness and hence volume has decreased rapidly recently. Between 1980 and 2008 it is revealed that the average sea ice thickness has decreased by 1.75 m (Kwok and Morison, 2011). Studies of uncertainties however show that the decline in sea ice volume may be less dramatic than shown in some studies and that uncertainties in thickness can be as high as 0.28 m in February/March and 0.21 m in October/November (Zygmuntowska et al., 2014). Also the ice volume does not shrink every year. Between autumn 2010 and 2012, there was a decline in volume of 14 percent, which is still in keeping with the long term decline. On the other side, 33 % and 25 % more ice volume was observed in autumn 2013 and 2014, respectively, relative to the 2010-2012 seasonal

mean, which offsets earlier losses (Tilling et al., 2015).

The drift of Arctic sea ice has been closely monitored by using satellite tracking (Kwok et al., 1998), buoys (Rigor et al., 2000) and usage of Doppler sonar instruments (Melling and Moore, 1995). The average drift speed of sea ice has increased by 4.5 % per decade between 1978 and 2007 (Rampal et al., 2009). The largest trends in drift speeds were found between 2001 and 2009 and could not be explained by increases in mean wind speeds. They coincide with years of rapid thinning, suggesting a responses to change in mechanics due to thinner ice with less resistance to deformation (Kwok et al., 2013). There seems to be no scientific consensus on whether there is significant increase in outflow of Arctic sea ice through the Fram Strait in the period studied between 1979 and 2013. Recent studies of high resolution radar satellite imagery of sea ice drift, show an increasing trend of 7 % per decade (Halvorsen et al., 2015; Smedsrud et al., 2011). Other studies show no significant increase in export of Arctic sea ice through the Fram Strait (Spreen et al., 2011; Kwok et al., 2013). Wind stress is a major atmospheric force affecting the sea ice, its location and divergence, but this factor will not be studied in detail in this thesis.

The consequences of sea ice loss in the Arctic Ocean are many, and they are potentially far-reaching: anomalies affect the atmospheric circulation patterns locally and likely remotely (Honda et al., 1996; Grassi et al., 2013), and could influence mid-latitude weather patterns, although the evidence for this is still unclear (Francis and Vavrus, 2012; Barnes, 2013; Screen et al., 2013; Mori et al., 2014). The observed changes that have been observed have been attributed both to anthropogenic forcing and natural variability (Lindsay, 2005). Many studies conclude that both internal and external forcings are needed to explain the change in sea ice, but that the recent reduction is strongly related to global warming and human influence (Serreze et al., 2006; Polyakov et al., 2010; Bekryaev et al., 2010; Comiso, 2012).

2.3.2 Sea Ice physics: growth and melt

The process of sea ice growth and melt is fully dependent on the heat fluxes in and out of the ice and can be explained by a simple set of equations based on Stefan's Law (Stefan, 1889). The following description is based on Eicken (2003) and Ivanov et al. (2016).

If sea water is to freeze, it must first be cooled to the freezing point, which for water with salinity 34 (psu) is at -1.86 °C. Pure seawater, lacking solid impurities that can act as nuclei for ice crystal formation, can be cooled below the freezing point (supercooling). Due to an abundance of impurities however, an initial ice layer quickly forms when water in the Arctic reaches the freezing point. Associated with this process of transition from water to ice, is a latent heat of freezing, which for pure ice is 334 Jg^{-1} (Yen et al., 1991). For sea ice, Maykut (1985) approximated the latent heat as;

$$L_{ice} = L_{fresh}(1 - 0.03 \cdot S_{ice}). \tag{2.1}$$

Here L_{ice} is the latent heat of sea ice, L_{fresh} the latent heat of freshwater, and S_{ice} the salinity of the sea ice. The initial ice cover has many forms and stages, but once it

reaches a developed ice cover, heat released from bottom freezing and cooling of the ice is transferred to the upper surface of the ice cover and ultimately released to the atmosphere. This transfer rate is determined by the thermal properties of the ice and the energy balance at the top and bottom. This energy balance for the sea ice can be explained as:

$$(1-\alpha)F_r - I_0 + F_l \Uparrow + F_l \Downarrow + F_s + F_e - F_c + F_m = 0. \tag{2.2}$$

Here the individual terms are: incoming solar short wave flux, F_r; the short wave flux penetrating the ice/water, I_0; the incoming and outgoing long wave flux, F_l; the turbulent atmospheric sensible heat and latent heat fluxes F_s and F_e respectively; heat due to melting at surface, F_m and the conductive heat flux from the interior of the snow/ice, F_c (often written as dq/dt). α represents the sea ice albedo.

A proper mathematical treatment of this equation requires numerical techniques because the individual terms depend either directly or indirectly upon surface temperature, which in turn determines the conductive heat flux and hence the ice growth (Steele and Flato, 2000). It is however possible to make some simplifications and arrive at a simple model for ice growth based upon equation 2.2. The conductive heat flux in equation 2.2 can be thought of as a residual term that responds to changes in the other fluxes into and out of the surface layer by inducing variable rates of growth or melt at the ice bottom. Assuming a linear temperature gradient for ice of thickness H, this conductive heat flux is according to Eicken (2003) given by:

$$F_c = -\lambda_{si}\left(\frac{T_0 - T_f}{H}\right), \tag{2.3}$$

where T_f is the freezing temperature, T_0 the surface temperature, and λ_{si} is the thermal conductivity of the ice. The latter is a fairly complicated function of brine (salt water) volume and temperature, but an approximation was suggested by Untersteiner (1964):

$$\lambda_{ice} \approx \lambda_{fresh} + \beta S_{ice}/T_{ice}, \tag{2.4}$$

where β is a constant (0.117 $\mathrm{JM^{-1}K^{-1}s^{-1}psu^{-1}{}^{\circ}C}$). Equation 2.3 is slightly more complicated when one takes into account a snow cover on top of the ice, which in our study is neglected. The ice growth or melt rate can in turn be estimated by the energy balance at the lower boundary of the ice. Here F_c is equal at the top and bottom of the ice and is together with the oceanic heat flux F_w (often written as $\langle w'T'\rangle_0$) balanced by the release or uptake of latent heat, L_{ice}, during freezing or melting for a thickness change of dH/dT for ice of density ρ_i:

$$\frac{dH}{dt}\rho_i L_{ice} + F_c + F_w = 0 \tag{2.5}$$

From the equations following Eicken (2003) we can see that quantification of the oceanic heat flux F_w towards the ice is very important for sea ice growth and melt. Figure 2.4 gives an illustration of the process described above.

During the Arctic winter the contribution from the short wave radiation F_r and I_0 in equation 2.2 is negligible because of the polar night. As is the heat due to melting at the surface, F_m, and the latent heat flux, F_e. The net balance of long wave radiation (incoming minus outgoing) is usually (if air temperatures are below freezing) positive if the positive direction is defined upwards (Ivanov et al., 2016). All these variables vary over time and in space. In any case the total heat flux at the air-ice interface is usually positive during winter, favouring ice growth. From equation 2.5 follows that since the thickness change of ice during winter is not constant there must be a heat flux from the ocean mixed layer towards the ice lower boundary (Ivanov et al., 2016). Because we experience melting and prevented ice growth during winter in some areas in the Arctic Ocean (Onarheim et al., 2014), this oceanic heat flux must be larger than the other positive heat fluxes in some areas. Such increase of oceanic heat flux, F_w, must be due to increased mixing of heat from below. This process was suggested by Rudels et al. (1999a), and the processes responsible for bringing up heat will be described in the following chapters.

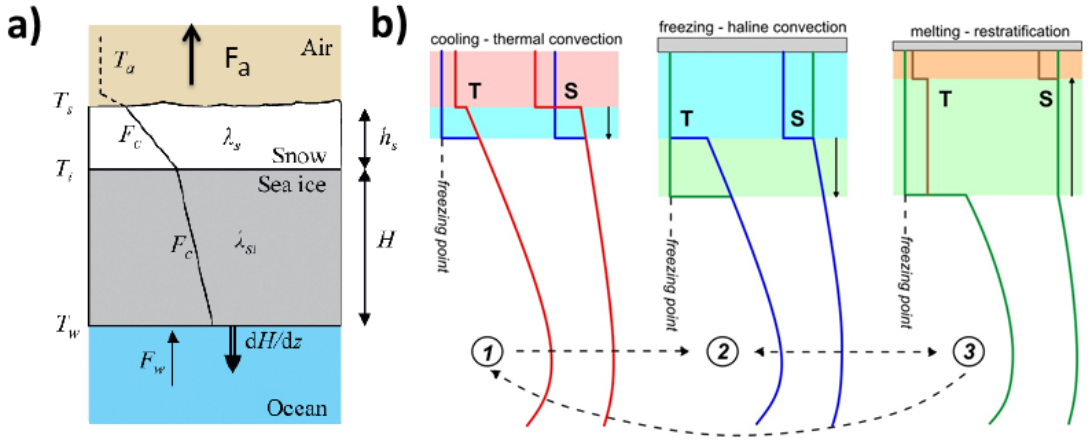

Figure 2.4: a) Illustration of a two-layer model of sea ice growth. Heat lost to the atmosphere will lead to ice growth (Equation 2.5). Here F_c is the conductive heat flux through the ice and snow, F_w the oceanic heat flux, F_a the heat flux to the air, and λ the thermal conductivity for ice and snow. Figure from Eicken (2003). b) Illustration of the thermal and haline convection processes during ice growth and the restratification process during sea ice melt. In step one the the mixed layer is completely cooled to the freezing point which will gradually deepen the mixed layer (Kraus and Turner, 1967), in step two ice formation starts, brine (salt water) is released, and haline convection leads to a deepening of the mixed layer, in step three sea ice melts, restratifies the mixed layer with a thin fresh layer on top, creating a new thin mixed layer on top of the old one. Figure from Ivanov et al. (2016). T is the temperature profile and S is the salinity profile.

Haline convection

Convection during the ice growth process occurs in two regimes: thermal (Kraus and Turner, 1967) and haline (Rudels et al., 1999b). Thermal convection is induced by

cooling of the surface layer, which gradually deepens the upper mixed layer until it drops below the freezing point and initiates ice growth (Fig. 2.4 b)). When the ice grows, the actual ice crystals consist of pure water, but some brine will be trapped in small pockets within the ice. The remaining, approximately two thirds of the salt from the frozen water is released from the ice as cold heavy brine. This brine mixes with the underlying water making it more saline and heavier. As the density of the top-layer increases, it will gradually deepen through convection (Fig. 2.4 b)). This convection must reach at least down to the depth were the density is equal to the density of the newly mixed layer. Often the convection reaches deeper than this, eroding the pycnocline and thus mixing heavier water upward. This is one process, together with many others, that can also be responsible for bringing up warmer water to the surface mixed layer.

2.4 Arctic Ocean Hydrography and Water Masses

The Arctic Ocean can mainly be divided into three layers; the Polar Surface Water layer (PSW) reaching from the surface to 200 m, the intermediate layer between 200 m and 800 m depth including Atlantic Water (AW) and Pacific Water (PW), and the deep layer including various bottom waters below 800 m (Rudels, 2015).

Table 2.1: Definitions of water masses following (Rudels et al., 2000). In this thesis there will be made no distinction between AW and MAW, and for simplification AW is defined as all waters at intermediate depth warmer than 0°C. *σ is the potential density relative to 0 dbar, 500 dbar ($\sigma_{0.5}$) or 1500 dbar ($\sigma_{1.5}$), and θ is the conservative temperature.*

Water mass	**Specifics**
PSW (Polar Surface Water)	$\sigma_0 < 27.7, \theta < 0°\text{C}$
WPSW (Warm Polar Surface Water)	$\sigma_0 < 27.7, \theta > 0°\text{C}$
AW (Atlantic Water)	$27.70 < \sigma_0 < 27.97, \theta > 2°\text{C} + \sigma_0 > 27.97,$ $\sigma_{0.5} < 30.444$ and $\theta > 0°\text{C}$.
MAW (Modified Atlantic Water)	$27.70 < \sigma_0 < 27.97, \theta < 0°\text{C}, S < 34.676 + 0.232\theta,$ or $27.97 < \sigma_0$ and $\sigma_{0.5} < 30.444, 0°\text{C} < \theta$
AIW (Arctic Intermediate Water)	$27.97 < \sigma_0, \sigma_{0.5} < 35.142, \theta < 0°\text{C}$
CBDW (Canadian Basin Deep Water)	$30.44 < \sigma_{0.5}, \sigma_{1.5} < 35.142$
EBDW (Eurasian Basin Deep Water)	$35.142 < \sigma_{1.5}$

We will first describe the upper ocean layer, then the intermediate layer, and finally the deep layers. There is more evaporation than precipitation in the Atlantic Ocean, and some of the freshwater falls as precipitations in the Pacific Ocean, or is carried by rivers into the Pacific Ocean. A significant pathway for return of freshwater from the Pacific Ocean to the Atlantic Ocean is through the Arctic Ocean (Jones, 2001). There is also a substantial inflow of warm and buoyant freshwater through direct river input into the Arctic Ocean (Serreze et al., 2006; Carmack et al., 2015). Based on model studies, it is expected that the freshwater input to the Arctic will increase in the future as the

hydrological cycle accelerates and high latitude precipitation and river runoff increases (Nummelin et al., 2015). Projections show that the Arctic runoff can increase by 30% by the end of the century (Lehner et al., 2012). A fully coupled climate model showed that this increasing river runoff will strengthen the stratification in the Arctic Ocean, warm the halocline and AW, and spin up the cyclonic circulation of AW (Nummelin et al., 2016).

Sea ice formation though brine rejection over broad continental shelves is one of the major sources for water mass transformation in the Arctic Ocean (Aagaard et al., 1985). In the Barents Sea alone, cooling results in the continues formation of 2 Sv of Cold Deep Water (Årthun et al., 2011). The surface mixed layer exists across the whole Arctic Ocean and with a wide range in salinity and temperatures close to the freezing point, extending down to 25-50 m (Rudels, 2015; Jones, 2001). The mixed layer is a medium for storage, distribution and release of seasonal heat acquired at the ocean surface. The depth of the surface mixed layer is determined by both thermodynamic (ice melt and growth and atmosphere-ice-ocean heat and water exchange (Lemke and Manley, 1984)) and dynamic (wind forced (Rainville and Woodgate, 2009) or tidal driven (Fer et al., 2015)) processes. Rudels et al. (1996) states that the mixed layer in the Nansen Basin northeast of Svalbard is formed as a result of AW cooling and freshening of the upper part of the water column.

At intermediate depth AW and PW are found with generally higher temperatures than surrounding water masses. AW is a warm, salty water mass defined as water warmer than 0 °C and salinity 34.8-35 psu and has its temperature maximum between 200 m and 900 m depth (Rudels, 2015). The AW will be discussed in more detail in the following chapters. In the Canadian Basin there is an injection of relatively fresh and warm water of Pacific origin (PW) at intermediate depths. This PW is characterized by low salinities (< 33 psu), a temperature maximum warmer than -1 °C, low density, and relatively high heat content (Steele, 2004). In the Canadian Basin the PW is situated between the AW and the PSW, hereby strengthening stratification and limiting heat exchange (McLaughlin et al., 2004). The inflow of PW varies seasonally: warmer and fresher water during summer entering at depths of 40-80m and colder more saline water entering during winter at depths of 80-220 m (Weingartner et al., 2005; Woodgate et al., 2005).

AW is separated from the surface by a cold layer called the cold halocline. The origin of the Lower Halocline Water is uncertain, but several processes have been suggested. For example formation through brine rejection topped with fresh cold waters (Aagaard, 1981), or injection of cold salty shelf waters (Steele and Boyd, 1998). It is proposed that formation of the halocline starts when the warm AW meets the ice edge, and becomes cooled and freshens (Rudels et al., 1996). The inflowing water then undergoes cycles of freezing and melting with convection to the top of the Atlantic layer, until fresher water from the Laptev Sea provides a cap that prevents further convection (Jones, 2001).

Below 800 m and the 0 °C isotherm the deep water masses are rather uniform in salinity and temperature, and they take up about 60 % of the total Arctic Ocean volume (Aagaard et al., 1985). Separated by the Lomonosov Ridge we find Eurasian

Deep Water (EBDW) and Canadian Basin Deep Water (CBDW). Helland Hansen and Nansen stated already in 1906 that most of the deep water masses are produced in the Arctic Ocean, north of the Greenland-Scotland ridge and cannot flow out due to the sills (Nansen, 1906). The Greenland Sea Deep water (GSDW) is the coldest and freshest. Below this follows slightly warmer and saltier Norwegian Sea Deep Water (NSDW). Further down there is more saline and warmer water in the Eurasian Basin (EBDW), whereas the warmest and saltiest deep water is found in the Canadian Basin (CBDW) (Aagaard et al., 1981, 1985; Schauer et al., 2002). Dense water produced in the Arctic Ocean provides North Atlantic Deep Water that overflows southwards on the Greenland-Scotland ridge, and contributes to the global overturning circulation (Swift et al., 1997; Rudels, 2015; Aagaard et al., 1985).

2.5 Arctic Ocean Circulation

In the Arctic Ocean, the large scale intermediate circulation, including the AW, is cyclonic, with separate cyclonic cells in the smaller basins (Fig. 2.5). Surface circulation is cyclonic in the Eurasian Basin and in the Nordic Seas, but anticyclonic in the Canadian Basin, a feature commonly referred to as the Beaufort Gyre. This vanishes at intermediate depths (Talley et al., 2012). The Arctic Ocean provides a pathway between the Pacific and the Atlantic but also modifies waters and is the source for several water masses. A combination of observations and simulations show that the inflow of water to the Arctic Ocean through the narrow Bering Strait has a transport of approximately 0.8 Sv, while the inflows through the Fram Strait and the Barents Sea are 4-7 Sv (Schauer and Beszczynska-Möller, 2009) and 3.4 Sv (Smedsrud et al., 2010) respectively. Input from rivers is small (0.1 Sv) but important. Nearly all outflow is through the western Fram Strait (7-9 Sv) or the complex channels of the Canadian Archipelago (1.5-3 Sv) (Rudels, 2015; Aagaard et al., 1985).

The circulation of the intermediate layers is dominated by the narrow topographically steered Arctic Circumpolar Boundary Currents along the continental slope and the cyclonic gyres (Aagard and E.C. Carmack et al., 1989). AW originating from the North Atlantic flows around the Arctic Ocean along the continental slope by two branches of the boundary current. One branch enters through the Fram Strait (Schauer, 2004; Fahrbach et al., 2001) while the other flows into the Barents Sea and enters the deep Arctic Ocean through the 600 m deep St. Anna Trough in the northern Kara Sea. North of the Kara Sea these branches converge and follow the shelf slope (Schauer et al., 2002). The merged branches follow the Eurasian Basin bathymetry in a cyclonic way as a narrow topographically trapped boundary current with an annual mean speed of 1-5 $\mathrm{m\,s^{-1}}$. This boundary current divides into two branches over the Lomonosov Ridge (Woodgate et al., 2001; Karcher, 2003; Polyakov, 2005); one branch continuing towards the Makarov Basin and the second branch turning back towards the Fram Strait (Woodgate, 2013). The circulation pattern of AW and surface waters is shown in Figure 2.5. Rudels et al. (1996) postulated that the illustration of AW diving beneath out-flowing low salinity PSW, as it enters the Arctic Ocean is misleading. A part of

the mixed layer may follow the ice while another part may follow the AW to the East. The flow of the mixed layer north of Svalbard will be discussed in further detail in this thesis.

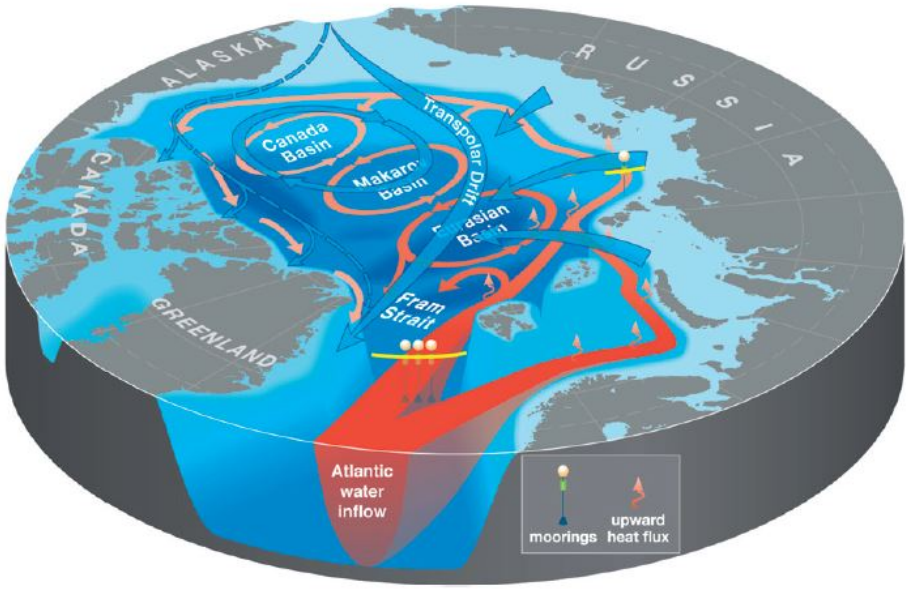

Figure 2.5: Circulation of cold surface water (blue arrows) and AW (red arrows) in the Arctic Ocean. The Lomonosov Ridge, running from Siberia to Greenland, separates the Makarov and Eurasian Basins. Another midocean ridge, the Nansen-Gakkel Ridge, divides the Eurasian Basin in the Nansen Basin and the Amundsen Basin. The transpolar drift direction of the sea ice is also marked with a blue arrow. Figure from Polyakov et al. (2012).

Further into the Arctic Ocean, away from the shelves, topography plays less of a role and eddy structures are more common (Hunkins, 1974). These mesoscale eddies play an important role in upper-ocean lateral and vertical fluxes of heat, mass and momentum impacting the ocean interior (Hunkins, 1974).

The Arctic Ocean deep circulation is, like the intermediate nearly barotropic, but below 1700 m it is not well investigated. Residence time of these deep waters is long, perhaps 100 years or more and the circulation is presumed to be cyclonic (Jones, 2001). Water below 2500 m is mostly of Atlantic origin (Anderson et al., 1994), but bottom waters in the Eurasian Basin are too dense to have entered directly through the Fram Strait. These likely originate from shelf slope plumes triggered by a flow of dense water from the Barents Sea (Årthun et al., 2011).

Arctic sea ice is produced on the shelves. It generally circulates in the Beaufort Gyre and follows the Transpolar Drift which is the broad drift across the Arctic Ocean from the Siberian region to Greenland. About 15 % of the sea ice inside the basin is exported from the Arctic Ocean through the Fram Strait (Smedsrud et al., 2016).

2.6 Atlantic Water in the Arctic Ocean

2.6.1 Atlantic Water

Warm and salty waters (0-3 °C and salinity > 34.7 psu) originating in the North Atlantic enters the Arctic Ocean through the Fram Strait and the western Barents Sea (Aagard and E.C. Carmack et al., 1989; McLaughlin et al., 2009). For the Fram Strait Branch temperature and salinity decrease along its path. As it cools it also deepens. The upper interface between the cold halocline and the AW deepens from 100 m near the Fram Strait to 180 m in the Laptev Sea, to deeper than 200 m on the Eurasian side of the Lomonosov Ridge, and 300 m in the Beaufort Gyre (Aasen, 2009). In this study, the maximum temperature detected for each profile and with salinity greater than 34.7 psu, is called AW core temperature (Lique and Steele, 2012). AW carries a vast amount of heat, corresponding to the volume transport of approximately 9 Sv through the Fram Strait. It is a northward heat transport that varies seasonally from $\sim$ 28 TW in winter to $\sim$ 46 TW in summer. Some heat is recirculated but the net annual heat transport into the Arctic Ocean through AW is estimated to be 40 TW (Schauer and Beszczynska-Möller, 2009). Until recently, maximum temperatures were 2-3 °C in the Nansen Basin, but in the Canadian Basin, this had decreased to 0.5 °C. This shows that AW heat is lost along the AW pathway through the Arctic Ocean (Polyakov et al., 2010).

2.6.2 Atlantic Water seasonal variability

Early discussions regarding the concept of the AW layer in the Arctic Ocean did not admit significant seasonal variations of the thermohaline properties in this intermediate water (Dmitrenko et al., 2006). No harmonic cycle has been reported in the Canada and Makarov Basins, suggesting that the amplitude of seasonal variation in AW is strongly space dependent (Lique and Steele, 2012). In recent years existence of a strong seasonal cycle is demonstrated on the Atlantic side (Schauer, 2004) (Fig. 2.6), with seasonal temperature variability throughout the whole water column contributing up to 50 % of the total variance. The seasonal signal is shown to propagate through the 600 km transit from the Fram Strait through the Arctic Ocean and to intermediate depths. The seasonal salinity signal is strongest closest to the AW core and strongly reduced towards the surface, while for temperature the biggest seasonal signal is found at 70 m (Dmitrenko et al., 2006; Ivanov et al., 2009). The annual temperature maximum in the upper ocean (above 215 m) is reached in mid-November, when the ocean in this region is normally covered by ice (Ivanov et al., 2009). Clear separation between “summer” (warmer and saltier) and “winter” (colder and fresher) AW types is revealed there. The range of seasonal temperature change close to the core is estimated between 0.92 °C and 1.35 °C, even though maximum recorded seasonal variation is between 2.90 °C and 4.05 °C (Ivanov et al., 2009). The range of seasonal variability is the same order of magnitude as the range of the local mean AW heat content, suggesting its significance in seasonal changes of upward vertical heat fluxes from the AW core towards the surface. It should be noted that not all studies have found the existence of a seasonal cycle, for

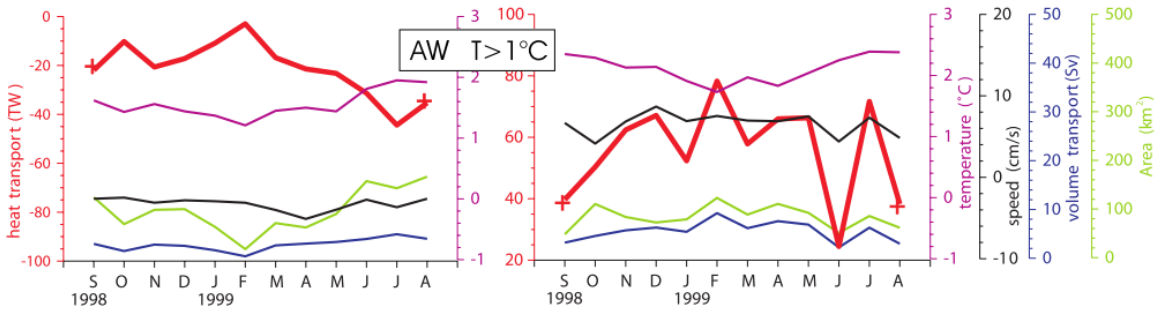

Figure 2.6: Time series of monthly mean values during the period 1998/1999 from moorings located in the Fram Strait (Schauer, 2004), which illustrate seasonal variability in the AW. The left panel shows AW flowing southward at the western side of the Fram Strait, while the right panel shows AW flowing northward in the West Spitsbergen Current. AW is here defined as water warmer than 1 °C. In the right panel we see a seasonal difference in inflowing AW temperature (pink) of almost 0.8 °C. The thick red line is calculated heat transport, blue is volume transport, black is the average velocity, and green is the associated cross section area. Figure from (Schauer, 2004).

example a year-long mooring observation at the eastern Laptev Sea slope provided no evidence of an annual cycle (Woodgate et al., 2001), neither did the multi-year mooring at the North Pole Environmental Observatory (Dmitrenko et al., 2006).

2.6.3 Atlantic Water long term change

Atlantic Water Warming

The AW layer in the Arctic Ocean has been subject to changes over the past decades. The first sign of strong warming within the AW layer was found in the Nansen Basin in 1990 (Rudels, 1991). Analysis of modern and historical data demonstrate that the temperature of the AW layer at intermediate depths (150-900 m) has increased in recent decades. In 1993, measurements from the Canadian icebreaker CCGS Larsen found warmer AW in the Makarov Basin near the Mendeleyev ridge (Carmack et al., 1995). In the eastern part of the Eurasian Basin the R/V Polarstern observed warming AW during cruises in 1993, 1995, and 1996 (Schauer et al., 1997, 2002; Rudels et al., 2000). More recent data show that even stronger warming started in the 1970s and was particularly strong in the 1990s and 2000s (Polyakov et al., 2012). AW core temperatures of the West Spitsbergen Current (WSC) have been measured annually (August) since 1977 by the Norwegian Institute of Marine Research (Fig. 4.7). These data indicate an overall warming of AW of 1.1 °C since 1979.

Not all studies agree on a warming trend in the Eurasian Basin, for example Bourgain and Gascard (2012) did not identify warming in their analysis of temperature data from 1997-2008. On the other hand a clear warming signal was observed in the same period by Polyakov (2005) (Fig. 2.7) and Ivanov et al. (2009). A year with extremely high AW temperatures was 2007. In this year, temperature anomalies, relative to climatological data, of 1 °C and higher were found in the Eurasian and Makarov basins

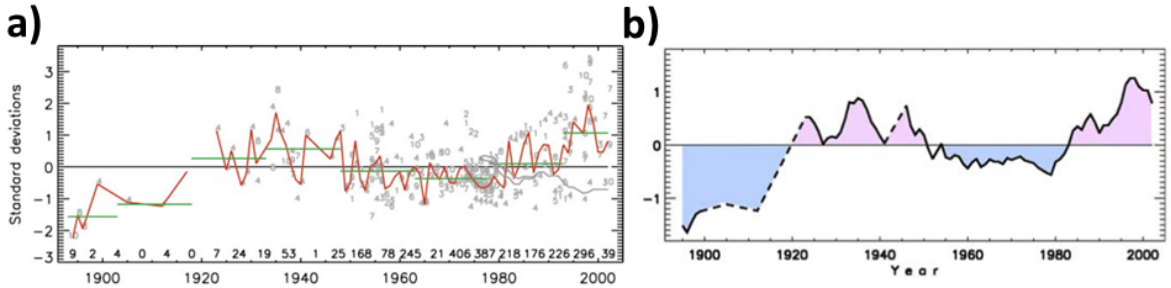

Figure 2.7: a) Long term variability of the AW temperature. Gray numbers present normalised values of AW core temperature anomalies for 10 regions in the Arctic Ocean as outlined in Fig. 1 in Polyakov et al. (2004). The green horizontal lines show 15 year means. Figure from Polyakov et al. (2004). b) 6 year running mean of normalised AW core temperature variability from the same regions as in a). Prolonged warm (red shading) and cold (blue shading) periods are associated with long term variability. Dashed segments represent gaps in the record. Figure from Polyakov (2005). Both figures indicate a long term oscillation, and warming in the last three decades.

(Polyakov et al., 2010). This is in accordance with findings from Perovich et al. (2008), who showed that in spring 2007 the core temperature of AW near the North Pole had increased by 0.5 °C. Data collected near the vicinity of Svalbard in 2006 also showed AW temperatures of a magnitude unprecedented in the history of local observations (Ivanov et al., 2009).

Warm pulses

The AW warming is not constant over time. A local maximum of 1 °C was observed in the mid-1990s (Polyakov et al., 2010), followed by an intervening minimum where the warming slowed or slightly reversed in the late 1990s (Boyd and Steele, 2002). Remnants of this signal arrived in the Canadian Basin in the early 2000s (Shimada, 2004). It appears that the warming of AW can be observed as pulses. For example, the AW temperature in the Fram Strait was lower in 1997 than in the mid 1980s (Rudels et al., 2000), and north of the Laptev Sea it was reduced from the high values in 1993, 1995 and 1996. Again an increase was observed in the Fram Strait just after in 1998, indicating a new warm pulse (Dmitrenko et al., 2006, 2008; Polyakov, 2005).

Low frequency oscillations

Long term oscillations have also been documented (Polyakov et al., 2004; Polyakov, 2005; Polyakov et al., 2009; Smedsrud et al., 2013). Over the twentieth century, the AW temperature records show two warmer periods, in the 1930s-40s and in recent decades, and two colder periods, early in the 1900s and in the 1960s-70s. It is suggested that the variations may be dominated by low frequency oscillations over a 50-80 year time scale (Polyakov et al., 2004) (Fig. 2.7). Some observed changes have been correlated with the North Atlantic Oscillation (Jones, 2001), and some shifts in atmospheric circulation

patterns have resulted in increased transport and temperature of AW heat through the Fram Strait (Rudels et al., 2000).

Global and Atlantic Water warming

Recent extreme warming of the AW inflow has also been attributed to current global warming events (Levitus et al., 2000; Dulvy et al., 2008). The current increase of temperatures in the AW core demonstrates anomalies stronger than previously observed (Polyakov et al., 2012). This warming is likely the strongest in the past 2000 years (Spielhagen et al., 2011), and is likely connected to anthropogenic forcing (Polyakov et al., 2010; Banks et al., 2000; Barnett et al., 2001, 2005; Kay et al., 2011). Observations show that also the temperature of AW flowing back to the Norwegian Sea has been anomalously high (Holliday et al., 2008), supporting the hypothesis that the Arctic Ocean is in transition to a new, warmer state (Dmitrenko et al., 2008).

Atlantic Water shoaling and retreat of the cold halocline

The warming of AW has been associated with a substantial shoaling in the Eurasian Basin (up to 75-90 m) of the upper boundary of the AW layer in the central Arctic Ocean. The warming has also weakened the Eurasian Basin upper ocean stratification (Polyakov et al., 2010). In the region north of Svalbard the interface between the AW and the layer above has a large year to year variability of approximately 20-30 m (Aasen, 2009). The interface was at record shallow depths in the 1990s, 80 $\pm$ 10 m, and is still shallow with values approximately 30 $\pm$ 10 m lower than historical data (Aasen, 2009). This shoaling, and following decrease in thickness of low salinity upper layer may also prevent the formation of a halocline. This situation was described by Steele and Boyd (1998) as the retreat of the cold halocline layer. Studies from a fully coupled climate model and a one dimensional model also show that the expected increase in freshwater runoff, that is described in Section 2.4, will most likely lead to a warmer and higher AW layer (Nummelin et al., 2015, 2016). Figure 2.8 shows model results from a one dimensional model illustrating that increased river runoff will give a stronger salinity stratification which can support stronger (inverse) temperature stratification, and lead to warmer AW at depth (Nummelin et al., 2015). According to Polyakov et al. (2010), the warming of the AW has an impact on the overlying upper layers in the Eurasian Basin, and it also has implications for the sea ice cover (Ivanov et al., 2016).

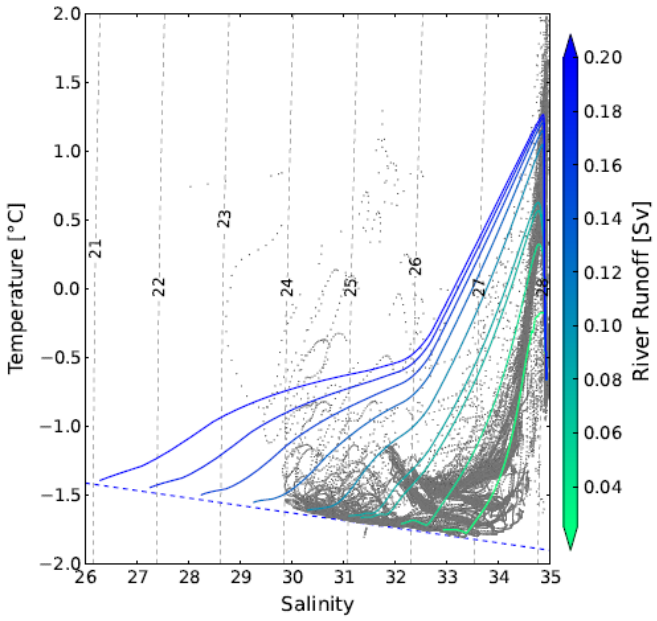

Figure 2.8: T-S diagram for the Arctic Ocean. The solid lines show the simulated steady state result from 1-D runoff model experiments, with colors indicating the runoff value. The black dots show observed climatological conditions (PHC3.0 from (Steele et al., 2001)). Figure from Nummelin et al. (2015).

2.7 Atlantic Water warming and sea ice bottom melting

2.7.1 Heat transport into the Arctic Ocean

The transport of heat to the Arctic Ocean is complex, and it involves several sources through top and bottom boundaries, advection, and vertical fluxes between the different layers. The first detailed volume, heat and salt budgets for the Arctic Ocean were formulated during the 1960s and 1970s (Mosby, 1962; Timofeyev, 1964; Aagaard and Greisman, 1975).

Most of the oceanic heat enters the Arctic Ocean through the Fram Strait as AW and through the Bering Strait as PW. Additional heat comes as sensible and radiative vertical fluxes into the upper ocean through thin ice, open water and leads, and as summer pulses of warm river water. Each of these have a seasonal cycle. The seasonal and shorter term variability of the atmospheric heat fluxes can be in order of 100 W m^{-2} (Persson, 2011). During summer these fluxes can be large but during winter they are small, zero or negative when the net long wave radiation and turbulent sensible heat fluxes cool the surface (Carmack et al., 2015).

Estimates of ocean heat transport into the Arctic Ocean from the Fram Strait between 1997 and 1999 vary between 28 TW and 46 TW (Schauer, 2004). Distributing this over the whole Arctic ocean deeper than 200 m, gives a vertical heat flux of 3.5-5.9 W m^{-2}. The heat transport associated with river discharge into the Arctic Ocean is 3

TW averaged over a whole year, which is about 10 % of the AW and PW (Whitefield et al., 2015). The oceanic heat advection may contribute to the observed reduction of Arctic sea ice, as will be discussed in this study. As global temperatures keep rising, heat transport into the Arctic Ocean may increase, and the sea ice cover may continue to shrink, but there are limits to how fast this can happen (Smedsrud et al., 2008).

2.7.2 Observed and simulated Atlantic Water influence on Arctic Sea Ice

Previously the AW entering through the Fram Strait has been considered as less important for the recent sea ice loss than PW. This is because changes in the sea ice cover have been connected to greater inflow of PW through Bering Strait and an increase in the atmospheric heat transport. Conversely it is now suggested that AW may have a direct impact on melting of sea ice and also hinders the growth of new ice (Alexeev et al., 2013; Ivanov et al., 2016).

Loss of sea ice in the Arctic Ocean has in general been largest during summer. In contrast, north of Svalbard, sea ice concentrations have decreased most during winter. Winter ice loss in this region is nearly 10 % per decade and is probably linked to the 0.3 °C warming per decade of AW in this region (Onarheim et al., 2014). This challenges our present understanding of how heat reaches the ice base from its original sources, such as AW and PW inflow, or summer sensible heat and short wave radiative fluxes at the ocean-ice interface. Small changes in ocean heat pathways plus advective input from the Atlantic and Pacific oceans and rivers could have a significant influence on current and future ice cover (Carmack et al., 2015).

Many new polynyas mirror the AW pathway, and dynamical forcing alone is unlikely to have contributed to such a steady decay in sea ice cover. Examples of this were seen especially in 2012, 2013 and 2014 (Ivanov et al., 2016). The rates of heat entrained from the ocean interior to the surface mixed layer follow an advective pattern of spots near the source locations (Fram Strait and Bering Strait) and further downstream following the main ocean pathways. In the Eurasian Basin the upward heat flux to the sea ice is highest along the AW pathway and where the AW is in direct contact with the surface layer (McPhee, 2003; Sirevaag, 2009). The AW has greatest effect on sea ice melting during summer when the temperature reaches its maximum and the warm water pool sits closest to the ice (Ivanov et al., 2016). The warm pool sits closer to the ice in summer because there is less wind during summer and hence less mixing which thicknes the mixed layer and pushes down the upper AW interface. There is also no freezing during summer which causes brine release and thickens the mixed layer.

A reduction in summer ice leads to an increase in accumulation of solar heat in the upper ocean (Perovich et al., 2008). This heat will slow down ice formation mostly during the following winter, making seasonal ice thinner in spring, or it may be released to the air above (Ivanov et al., 2016). The vertical structure of water masses and especially the density stratification below the mixed layer may be key factors affecting the fate of this summer heat (Steele et al., 2011).

Under ice-depleted conditions in summer, cooling and freshening of the upper AW layer slows down, as less ice melts per area. This water is better preconditioned for deep-reaching thermohaline convection during the next winter because of the weakened stratification (smaller temperature gradient). The winter driven convection can then more easily bring up a larger amount of sensible heat than the previous year. This increased heat flux due to more summer open ocean water is a possible positive feedback to the whole bottom melt and hindering of ice growth process (Ivanov et al., 2016).

The contribution from increased heat flux from deep AW on direct bottom melting of sea ice has been discussed a lot in recent years (Piechura and Walczowski, 2009; Onarheim et al., 2014). Model studies suggest that periods of increased heat fluxes lead to enhanced melting (Sandø et al., 2014). A reanalysis study using the Pan-Arctic Ice-Ocean Modeling and Assimilation Systems (PIOMAS) suggested volume loss rates of $2.8 \cdot 10^2 \mathrm{km}^3$ per year between 1979 and 2010 for the entire Arctic sea ice pack (Schweiger et al., 2011). If this loss is interpreted as a purely thermodynamic response to changing heat transfers from the atmosphere and/or ocean, the required net energy heat flux into the ice averaged over this period is about 1 $\mathrm{W\,m^{-2}}$ (Kwok and Morison, 2011). As the sea ice gets thinner, it becomes more fragile and mobile, facilitating the creation of more open water areas. This again supports increased convection and turbulence which further entrains even more warm and salty water from deeper layers (Ivanov et al., 2016).

To summarize, observations suggest that throughout most of the Arctic Ocean the vertical heat fluxes from the interior towards the mixed layer are generally weak (Padman and Dillon, 1987; Rainville and Winsor, 2008). But in some places, sometimes away from steep topography, AW heat reaching the overlying layers may be important and may impact the sea ice cover (Polyakov et al., 2012). It may not contribute to direct bottom melting everywhere, but keeps the ocean surface ice free in some areas (Ivanov et al., 2016). Different mixing and convection processes are responsible for bringing this heat up towards the sea ice, and understanding them is crucial for determining the impact of AW on sea ice. Figure 2.9 shows a schematic overview of the processes that influence sea ice in the Arctic Ocean (Carmack et al., 2015).

2.7.3 Vertical mixing and turbulence

To have an effect on the sea ice cover, the AW heat has to be mixed upwards to the ice. Vertical mixing and turbulence are complex processes. There exists little consensus on a precise definition of fluid dynamical turbulence, but one often used is is defined by Hinze (1975): "Turbulent fluid motion is an irregular condition of flow in which the various quantities show random variations with time and space coordinates, so that statistically distinct average values can be discerned." When different motion occurs between a sea ice cover and the upper ocean, momentum is exchanged across a turbulent boundary layer. If there are melting or ice growth processes at the ice ocean interface, this turbulent layer will also transport heat and salt. This again can induce further mixing and convection (McPhee et al., 2008). The most effective mechanisms

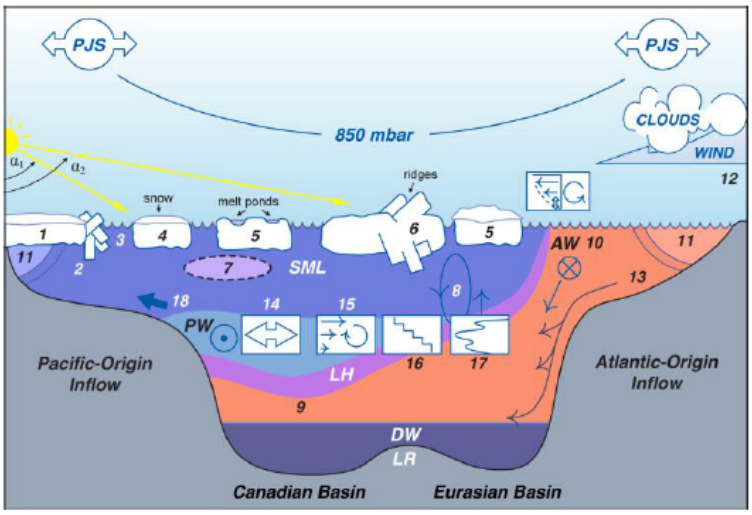

Figure 2.9: Schematic diagram showing the Arctic Ocean (shelves and basins) and key processes that affect the oceanic heat fluxes and hence the sea ice. 1-5 illustrates different types of ice in the Arctic Ocean. Oceanic processes are: 7) creation of near surface temperature maximum due to trapped solar heating, 8) free convection, 9) subduction and circulation of PSW/PW, 10) circulation of AW, 11) coastal trapped flow of river inflow, 12) wind forcing, 13) deep water formation, 14) mixing due to tides and internal waves, 15) mixing due to shear, 16) double diffusion and the related staircases, 17) thermohaline intrusions, and 18) shelf-break upwelling. DW stands for deep water and LR stands for the Lomonosov Ridge. Figure from Carmack et al. (2015).

for vertical mixing and hence upward heat transport in the upper Arctic Ocean are shear driven turbulence, convection due to brine release, tidal induced internal wave mixing, and double diffusion (Carmack et al., 2015) (Fig. 2.9).

Shear driven turbulence comes from the generation of shear instabilities which happens due to different vertical or horizontal current velocities (Fig. 2.9). Gradients of vertical current velocities often occur at the interface between different layers and are also influenced by the frictional stress from the ice on the ocean in the uppermost layer. Many different types of shear-flow instabilities are known (Thorpe, 2007).

Below the surface mixed layer, the column is usually non-turbulent, with vertical mixing rates close to molecular levels. Bathymetry plays an important role when it comes to mixing and hence entrainment of heat. For example large fluxes of heat towards the ice have been found over the Yermak Platau where AW is close to the mixed layer and mixing rates are high due to the effect of tidal flow over this topographic feature (McPhee, 2003; Fer et al., 2015). In general, the breaking of internal waves is a major source of turbulence-driven mixing in the ocean and hence also upward heat fluxes (Fer et al., 2015). One generation mechanism of such internal waves is the response to barotropic tidal flow of a stratified water column over topography, such as continental sloped, isolated ridges, or areas of increased seafloor roughness (Garrett and Kunze, 2007). This tidally driven mixing has large spatial variability but appears to be very energetic and efficient locally (Fer et al., 2015).

Another effective way of mixing in the Arctic Ocean is convection due to brine release when the surface layer freezes. During this process there is also a heat loss which induces thermohaline convection, but for the same heat loss the density increase due to brine rejection is one order of magnitude larger than that due to temperature decrease alone (Rudels, 1991). This process happens only during the freezing of sea ice and not during melting. Usually such convection reaches down through the mixed layer until it reaches the pycnocline, but it can also form very dense waters that sink deeper if the convection goes to the bottom (Årthun et al., 2011).

Double diffusion is another mixing mechanism that is important in the polar regions. This term describes what occurs when scalar properties in a fluid diffuse at a different rate. In cold seawater, for example, molecular thermal diffusivity is about 200 times greater than salt diffusivity. If a cold, fresh parcel was placed next to a relative warm and saline parcel the change in temperature with time relative to the initial difference in temperature would be far larger than the change in salinity relative to its initial difference (Schmitt, 1994). Since the density of seawater depends on temperature and salinity such differences can lead to vertical fluid motion and mixing. Under sea ice, double diffusive processes are different whether ice is melting or freezing. When sea ice melts a slightly fresher, cold layer of water is formed on top of a slightly warmer and saline ocean layer. This is called a diffusive layering instability. Because of the difference in diffusion rates, the thickness of the upward diffusion of heat exceeds (in density terms) the downward molecular diffusion of salt, resulting in a downward density flux that drives convection (Ruddick and Gargett, 2003). In other words, when the warmer water below cools and keeps its initial salinity it becomes heavier, submerges to a larger depth and generates eddy motion (Bukreev, 2007). This is the vertically reversed process of salt fingering. Salt fingering occurs when relatively warm and salty water overlie relatively colder and fresher water. However, both these processes result in a downward density flux and convection. Lateral thermohaline intrusions, that also lead to mixing, are known to be driven by double diffusion, and are formed by lateral motions across ocean fronts (Ruddick and Kerr, 2003).

In a different context, double diffusion in a very thin layer close to the ice/ocean boundary is important for the heat and mass balance of sea ice, because the small melting and freezing rates observed under the ice depend on exchange of heat and salt. Here double diffusion limits melt rates because the salt exchange limits the heat exchange (Sirevaag, 2009; McPhee et al., 2008). During freezing processes double diffusion leads to an increased production of supercooled water, because heat would be extracted faster from the ocean than salt would be be injected (Steele et al., 1989).

Chapter 3

Methods and Data

The observations presented here are sampled during the "Norwegian Young Sea Ice Cruise" (N-ICE2015), an ice-drift project completed between January and June 2015 (Granskog et al., 2016). The observations include hydrographic measurements, current time series, micro-structure profiles, ice-ocean boundary layer turbulence measurements, meteorological observations and satellite observed sea ice concentrations.

Different calculations were performed to investigate and visualize these results. In this chapter, the study area, the different instruments, the data processing and calculations are described. Observational data and model data were analysed using the numerical computing environment Matlab R2015a. Figures were made using personally developed scripts and maps using the *m-mapV1.4* mapping toolbox created by Rich Powlowicz (`http://www.eos.ubc.ca/~rich/map.html`). When nothing else is specified, analysis has been done in Matlab. Climatological data was analysed and binned using Ocean Data View (ODV) V.4.7.3. ODV is a proprietary, freely available software package for analysis and visualization of oceanographic data based upon DIVA software (`http://odv.awi.de/`). The program was used to plot profiles, sections and contour maps.

3.1 The N-ICE2015 project

During this project, a region north of the Svalbard archipelago was investigated (Fig. 3.1). Links and reference were sometimes made to the whole Arctic Ocean or other regions in the Arctic, but our area of interest is bounded in the south by 80°N, to the north by 84 °N, and lies within the zonal band 0-30 °E. Hence it includes a large portion of the AW inflow to the Arctic Ocean by the Western Spitsbergen Current (Fig. 2.5). This area of interest is hereafter referred to as the "N-ICE2015 study area". The N-ICE2015 study area is divided in three distinct regions which are determined by bathymetry and labelled as "Basin", "Slope" and "Plateau". The Basin consists of all areas with water depth greater than 2000m including both the Sofia Deep and parts of the Nansen Basin. The Slope is defined as areas with water depth between 1000m and 2000m, while the Plateau makes reference to the marginal Yermak Plateau north-west of Svalbard and is defined by depths shallower than 1000m.

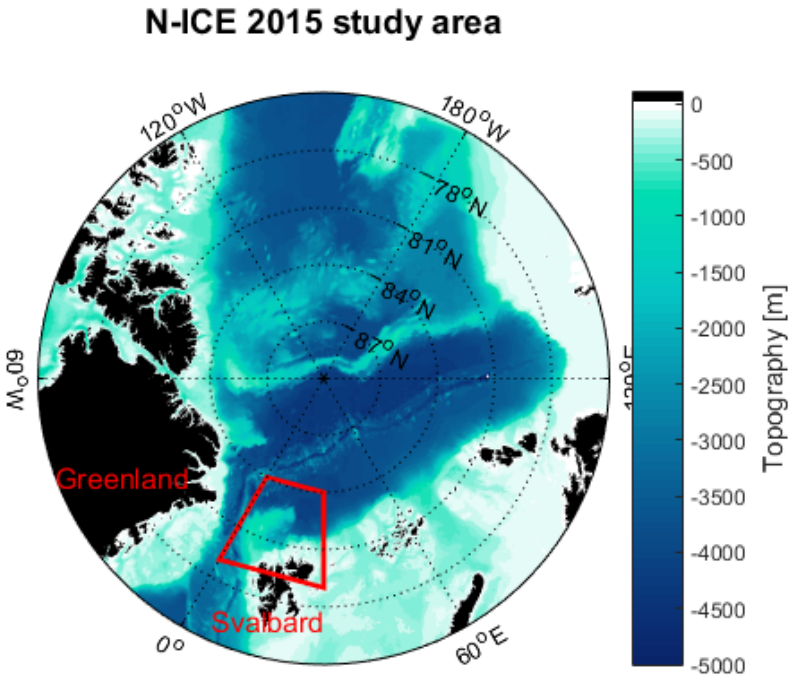

Figure 3.1: Map of the Arctic Ocean with the N-ICE2015 study area (red box) and overlying topography in color scale ranging from 0 m to 5000 m depth.

Sea ice is present in all seasons in all three regions, making it a good place to investigate air-ice-sea interactions. AW can be found at various depths throughout the whole region. It is therefore also a good location to study the processes that involve AW and its influence on the sea ice cover.

Between January and June 2015, the Norwegian research vessel Lance completed four drifts in the Arctic sea ice (Fig. 3.2). For each drift period the vessel was frozen into the ice and drifted following the wind and currents. On each floe an ice camp was set up and oceanographic, as well as atmospheric, ice, snow, and biology observations were collected (Granskog et al., 2016). At the beginning of the first three drifts the R/V Lance was accompanied into the ice by the icebreaker K/V Svalbard from the Norwegian Coast Guard. The drift ended when the ice broke up or the ship reached the ice edge. Hereafter, the four drifts are numbered 1-4 with the accompanying drift periods respectively ranging between Jan. 15 - Feb. 21, Feb. 24 - Mar. 19, Apr. 18 - June 5 and June 7 - June 22. These periods cover both winter and early spring season in the Arctic. In this study spring season is defined after 25th May, when extensive melting due to atmospheric forcing starts (Personal communication Amelie Meyer, Jan 2016). Specific areas of interest are where the bathymetry changes quickly, more specifically where the ship crosses the Slope from the Basin to the Plateau. Figure 3.2 shows some of these locations.

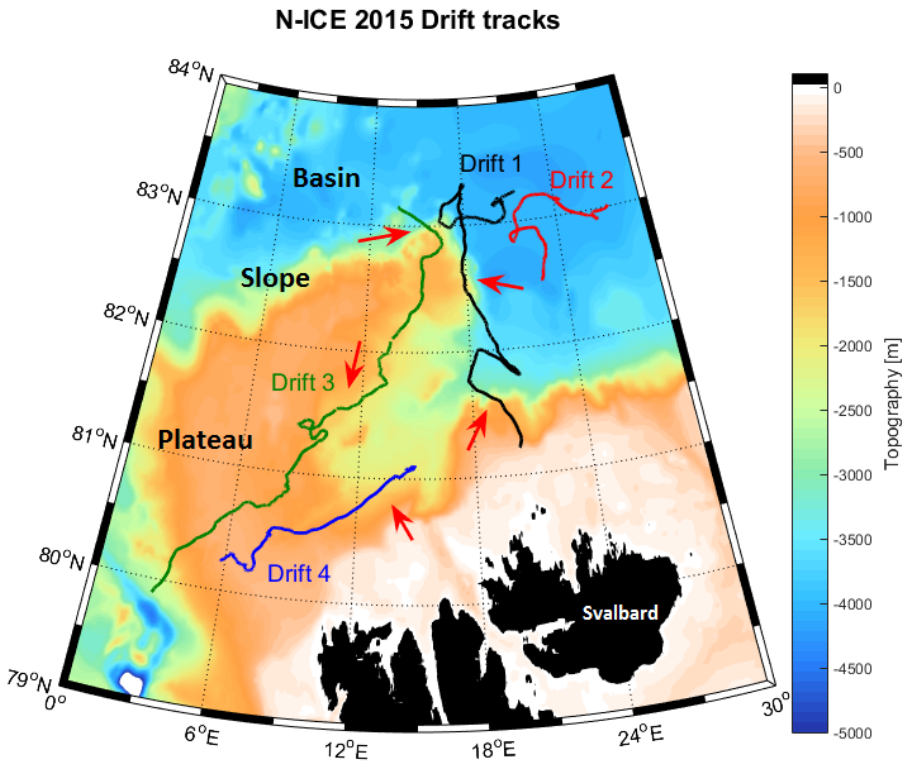

Figure 3.2: Map of the N-ICE2015 study area with tracks drifts 1-4 overlying topography in color scale ranging from 0 m to 5000 m depth. All drifts are in a south-western direction. Locations with fast bathymetry change along the Lance drift track are shown by red arrows.

3.2 Observations

Hydrographic measurements were acquired from the ship CTD (Conductivity, Temperature, Depth) instrument, and on-ice CTD instrument placed inside a tent about 500m away from the ship (Fig. 3.3 shows the typical camp layout). The current time series originate from vessel mounted and under-ice Acoustic Doppler Current Profilers (ADCP). Turbulence observations were made by Turbulence Instrument Clusters (TIC) at the Hut, and the micro-structure profiler (MSS) vertically down to 300 m in the Haven tent (Fig. 3.3). In this section the different instruments and other data sources are described in detail.

3.2.1 CTD

The ship based CTD was used for deep casts through a hole made in the ice next to the ship. This ship-CTD rosette (SBE32 12-bottle carousel)(Seabird Electronics, Seatle, USA) was equipped with 11 Niskin bottles for water samples, a lowered downward-looking 300kHz Workhorse Sentinel ADCP (Teledyne Technologies, Thousand Oaks, USA) and two pumped Seabird SBE911 plus sensors. Table 3.1 shows the specifications of the CTD-sensors. Other sensors include oxygen, fluorescence and Coloured Dissolved Organic Matter (CDOM). Salinity estimates were calibrated against water samples taken from the Niskin bottles and analysed with a Portasal salinometer (Guild-

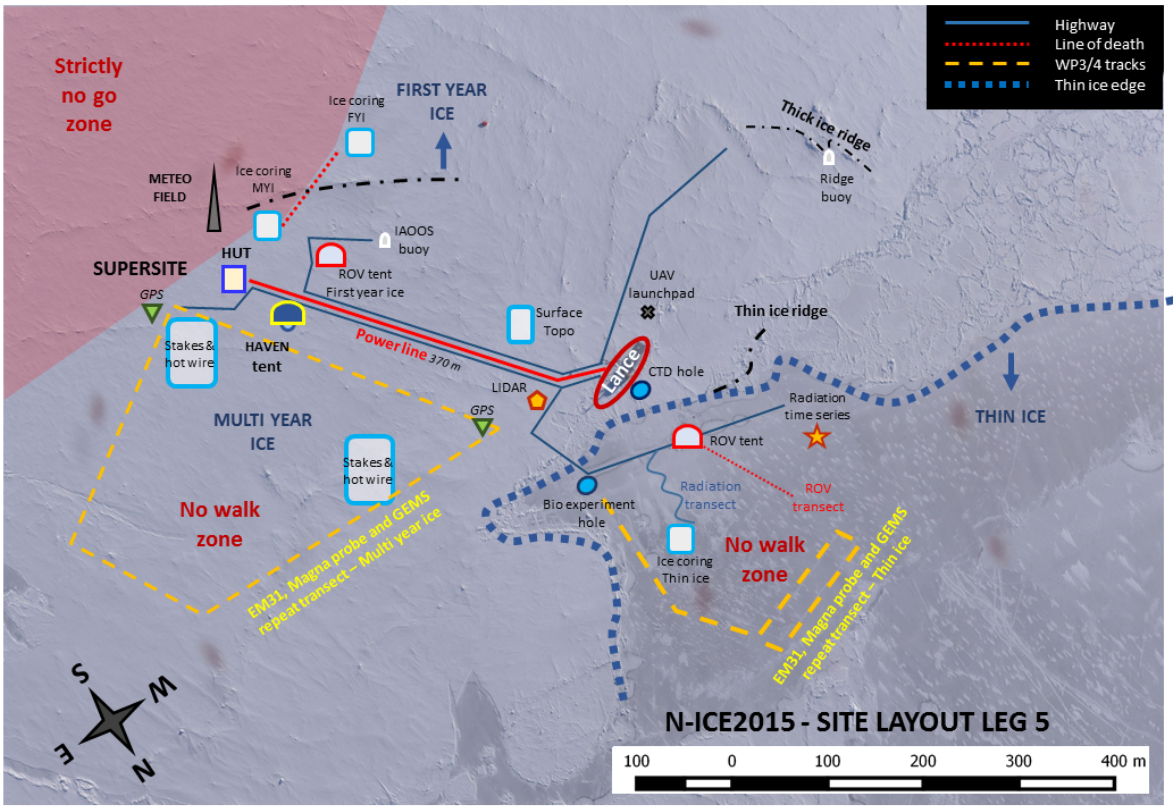

Figure 3.3: Illustrated map of the N-ICE2015 camp layout during drift 3 (similar for other drifts). RV Lance is situated in the center of camp, while the "Haven" tent where the on-ice CTD was located, and the "Hut" where the TIC was located are found at the "Supersite" approximately 400-500 m away from the ship. The compass rose is indicative for most of drift 3 but towards the end of the drift, the floe turned around and orientation changed. Figure courtesy of Amelie Meyer, Norwegian Polar Institute.

line, Smiths Falls, Canada) onboard the ship. All sensors were also calibrated before and after the cruise at the Seabird company. The dual CTD means there are two temperature and two conductivity sensors measuring simultaneously. When the two sensors are compared against each other failure can be detected.

Table 3.1: Range, accuracy and resolution of the ship-based SBE911 plus CTD system (Seabird Electronics, SBE911 datasheet, 2015)

Sensor	Range	Accuracy	Resolution
Temperature	-5 - 35 °C	± 0.001 °C	0.0002 °C
Pressure	0-10,340 dbar	± 0.015 % of range	0.001 % of scale
Conductivity	0-7 S/m	± 0.0003 S/m	0.00004 S/m

Ship-based CTD casts were planned weekly, but this could not be achieved throughout the whole campaign due to difficulty in maintaining an open hole at the ship side in thick sea ice. A total of 51 casts were done, from which 12 were in between floes, as shown in more details in Table 3.2. Figure 4.1 shows a map with the location of

the different CTD stations along the drift track. Parameters from the instrument were binned at 1m depth intervals down to maximum depth of 4091m. As part of this study a manual quality control was performed on each profile, removing and flagging bad data and possible sensor errors. Corrected "metadata" (time, location) was provided by the Norwegian Polar Institute.

Table 3.2: Distribution of ship-based CTD casts during the N-ICE2015 campaign.

Drift	**Nr. of casts**	**1000 m < casts < 2000 m**	**Casts > 2000 m**	**Comments**
Drift 1	10	3	3	None
Drift 2	5	3	2	Couldn't open hole on the floe
Drift 3	24	6	0	Three casts on shelf, 24 while ship was frozen in the ice
Drift 4	14	2	1	None

Secondary CTD measurements were done by a so called on-ice CTD, a Multi Water Sampler (MWS-12) rosette (Hydro-Bios, Kiel, Germany) equipped with a non-pumped conductivity, temperature and pressure sensor. Specifications of the CT-450 500 sensors are given in Table 3.3. The on-ice CTD was located in the "Haven tent" at the ice-camp approximately 200-400 m from the ship. Figure 3.3 shows a map of the standard ice-camp and the approximate location of the "Haven tent" during Drift 3. On-ice CTD casts were performed approximately twice a week throughout the campaign, where the sampler was winched through a hole in the ice to a maximum depth of 1000m. On a typical on-ice CTD day three casts were done, of which two shallow biological casts and one deeper chemistry or oceanography cast. Figure 4.1 shows the location of the on-ice CTD stations along the drift track, and table 3.4 gives an overview of the distribution of observations. Quality of the Hydro-Bios temperature sensor is good, however the salinity sensor experienced a large linear drift during the cruise. The drift in salinity was corrected for by comparison of bottle samples and fitting of a linear calibration function (Section 3.4.2). The datasets from the two CTD instruments were not merged because of the large difference in accuracy between the sensors.

Table 3.3: Range, and accuracy of the on-ice Hydro-Bios CTD sensors (Hydro-Bios, MWS 12 datasheet, 2015)

Sensor	**Range**	**Accuracy**
Temperature	-2 - 32 °C	± 0.005 °C
Pressure	0-3000 dbar	0.1 % of range
Conductivity	0-65 S/m	± 0.01 S/m

Other hydrographic measurements such as temperature include ten TinyTags Aquatic 2 TG4100 (Gemini Data Loggers, Chichester, UK), which were moored under the ice at 10m depth intervals together with a Microcat CTD SBE37 (Seabird Electronics, Seatle, USA) at 110m depth. These measurements have been used for quality control of the

Table 3.4: Distribution of on-ice CTD casts during the N-ICE2015 campaign.

Drift	Nr. of casts	Casts deeper than 50m	Comments
Drift 1	21	20	none
Drift 2	19	16	none
Drift 3	38	28	none
Drift 4	13	11	100m cable lost

other CTD data. The Tinytags have good temporal coverage, but limited accuracy and vertical distribution. Their measuring interval was set to 10 min.

3.2.2 ADCP

The current measurements analysed in this study were obtained from two different instruments: a Vessel Mounted RDI 150kHz Acoustic Doppler Current Profiler (VMADCP) and a sub-ice moored RDI 75kHz Long Ranger Acoustic Doppler Current Profiler (ADCP) both produced by Teledyne Technologies (Thousand Oaks, USA). The VMADCP is in general used for the upper layers ($\approx$ 100-200 m) while the Long Ranger is used for studying the deeper layers ($\approx$ 500 m).

An ADCP uses the Doppler shift principle to measure current velocity. The ADCP has transducers which transmit and receive acoustic pulses. These pulses are scattered and reflected by particles in the water column, e.g. phytoplankton or suspended sediments. These particles are assumed to move passively with the currents. Pulses reflected back by a moving particle will have a different frequency than those previously emitted. This frequency shift is called the Doppler-shift and depends on the speed and direction of the moving particle. If the particle moves away from the instrument, the reflected sound has a higher frequency. As the particle moves towards the instrument the opposite occurs. Using this information, the current velocity can be calculated.

Only a part of the pulse beam is reflected. The range of the signal is dependent on frequency of the instrument, where lower frequencies give further range but lower accuracy and higher frequencies give higher accuracies but shorter range. At least three acoustic transducers are needed to obtain a three dimensional velocity vector at different depths. Figure 3.4 shows the ADCP (Long Ranger).

RDI Long Ranger

The RDI Long Ranger is a low frequency ADCP with a 4 beam design where the beams are sent out at 20° angle relative to the vertical plane (Fig. 3.4). Three beams measure horizontal and vertical velocities to obtain u, v, w, where u and v are the horizontal components and w is the vertical component. The fourth beam is used to see if flow is close to horizontal homogeneity and to ensure the measurements are accurate. The beam width of the Long Ranger is 4°. More detailed specifications and the instrument set up are given in Table 3.5 (Teledyne, RDI Long Ranger datasheet, 2013).

Figure 3.4: Picture of the RDI Long Ranger 75kHz from Teledyne, RDI (Long Ranger datasheet, 2013)

Table 3.5: Instrument specifications and setup of the RDI 75kHz Long Ranger (Teledyne, RDI Long Ranger datasheet, 2013)

Sensor	**Range**	**Accuracy**	**Resolution**
Velocity	± 5 m/s	$\pm 1\% \pm 5$ mm/s	1 mm/s
Compass	$0 - 360°$	$\pm 2°$	0.01°
Tilt	$\pm 50°$	$\pm 0.5°$	$\pm 1.0°$
Measuring interval:	Varying for each drift		
Bin size:	8 m		
Ping count:	1 Hz		

The RDI Long Ranger was deployed downward-looking under the ice during drift 1, 3 and 4. Details for sampling days are given in Table 3.6. Processing of the raw data from the Long Ranger was done using the RDI manufactured program WinADCP. Data was binned in 8 m bins, interpolated, dedrifted and a quality control was performed by Ingrid Onarheim (UiB). Bad data were selected using set criteria: $u/v/w > 10$ m/s, pitch/roll $> |20°|$, Average echo intensity < 40, percentage good for 3 and 4 beams < 50. The first cell of the Long Ranger is at 17 m depth. Dedrifting was done by calculating the drift speed of the ship and subtracting this from the observed velocity. The Long Ranger measures down to approximately 500 m.

Table 3.6: Deployment details of the RDI 75kHz Long Ranger

Drift	**Sampling days**	**Deployment date**	**Recovery date**
Drift 1	5	11 Feb.	16 Feb.
Drift 2	0	-	-
Drift 3	31	03. May	04. June
Drift 4	8	11. June	19. June

VMADCP

The Vessel Mounted RDI 150kHz ADCP measured currents directly below the drifting vessel throughout most of the campaign. Data were obtained for all drifts except for a period between March 2nd and March 19th where the ship was lifted up by drifting ice

that accumulated under the ship hull, blocking the ADCP sensors. The RDI 150 kHz has a range of approximately 400 m and uses one single transducer with 30° angle and 4 different beams. Compass and tilt data were retrieved from the ship's navigational data. Specifications and setup of the VMADCP are given in table 3.7. In this study the VMADCP is only used for quality control and comparison with Long Ranger Data.

Table 3.7: Instrument specifications and setup of the Vessel Mounted RDI 150kHz ADCP (Teledyne, RDI VMADCP datasheet, 2009).

Sensor	**Range**	**Accuracy**	**Resolution**
Velocity	$-5-9$ m/s	$\pm 1.0\% \pm 0.5$ m/s	1 mm/s
Measuring interval	300 s		
Bin size	8 m		
Ping rate	1.5 Hz		

3.2.3 Turbulence Instrument Cluster

Heat fluxes and turbulence in the upper ocean and at the ice-ocean interface were measured using a Turbulence Instrument Cluster (TIC) developed by McPhee Research (`http://mcpheeresearch.com/`). Detailed boundary layer turbulence or micro structure are not deeply discussed in this study, but mean heat fluxes to the ice retrieved by the TIC are used.

The TIC is an eddy co-variance system with simultaneous high frequency (sampled at 24 Hz, averaged to 2 Hz) measurements of temperature, conductivity, micro conductivity, and currents (sampled at 512 Hz, averaged to 2 Hz) at two depths, separated by 4 m. Figure 3.5 shows a sketch of the TIC which consisted of a mast with Seabird temperature, pressure and conductivity sensors, a compass and two Acoustic Doppler Velocity meters (ADV, Sontek, San Diego, USA) with an underwater processing module (UPM). This system is capable of measuring velocity and temperature fluctuations well into the inertial subrange. Turbulent fluxes are calculated using an advective transformation (Reynolds analogy) to estimate ensemble mean deviatory products from the zero lag (in time) covariances. The method assumes a spectral gap between turbulent fluctuations and other time-varying phenomena (McPhee, 2002; McPhee et al., 2008; Sirevaag, 2009).

TIC instruments were deployed successfully during all four drifts. The instrument clusters measured at approximately 1-3 m and 5-7 m depth. Details about sampling periods are given in table 3.8 and a sketch is given in figure 3.5. In this study the TIC is only used to compare under ice heat fluxes and friction velocity with Long Ranger and CTD data for drift 3 and 4. Data analysis and calculations were performed by Algot Peterson (Peterson et al., in progress).

Table 3.8: Deployment dates and type of TIC deployed during N-ICE2015. NP means TIC from the Norwegian Polar Institute and UiB means the TIC from the University of Bergen.

Drift	Deployment details
Drift 1	25 days of sampling (NP)
Drift 2	9 days of sampling (UiB)
Drift 3	40 days of sampling (UiB)
Drift 4	10 days of sampling (UiB)

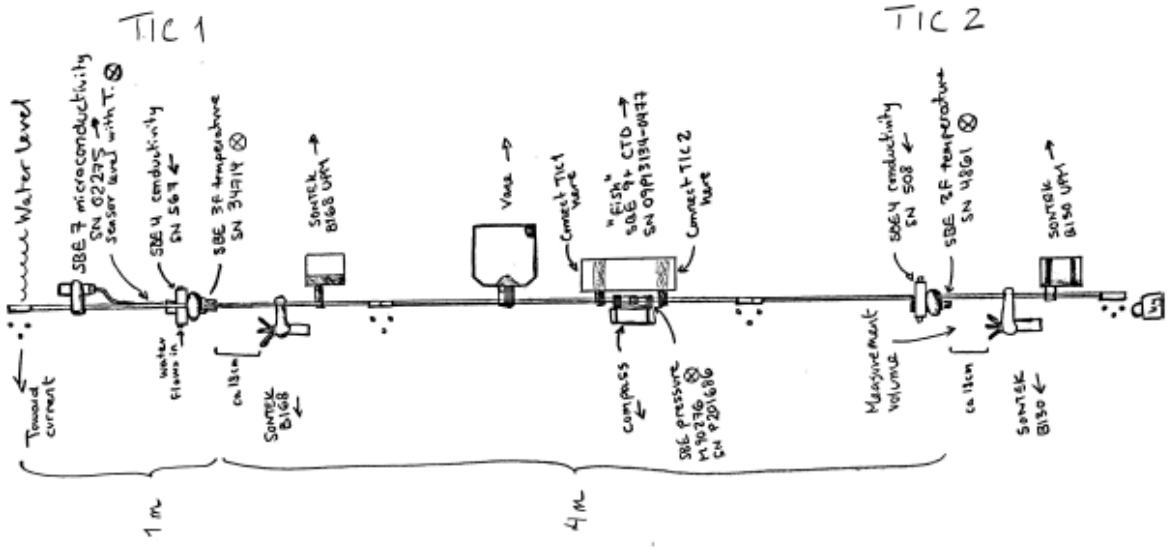

Figure 3.5: Schematic overview of the TIC set-up. TIC 1 is closest to the ice, and is the one used in this study. Tic 2 had malfunctioning sensors and has not been used in this study. Figure courtesy Algot Peterson (Peterson et al., in progress)

3.2.4 Atmospheric data

Wind speeds from the ship's meteorological system were obtained for comparison with current data. Data were downloaded as one minute mean and converted from knots to meters per seconds.

3.2.5 Historical data

A climatological data set of temperature and salinity from the Polar science center Hydrographic Climatology (PHC3.0) and World Ocean Atlas (WOA) was downloaded and analysed. Several historical data sets and climatologies have been created for the Arctic Ocean and the world oceans over the past decades with different resolution in different regions. The quality and accuracy of the climatology depends on the amount of data collected for the various times and regions, and also the methods used for data sampling and interpolation. Historical data coverage in the Arctic Ocean is a challenge but the PHC3.0 updated from Steele et al. (2001), together with the WOA from Locarnini et al. (2013) appears to have good data coverage in our region of interest

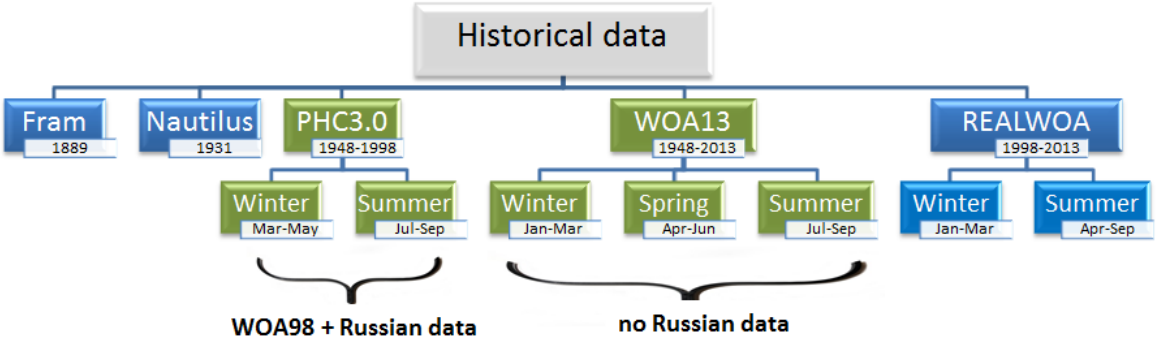

Figure 3.6: Schematic overview of the different historical datasets used in this study. Climatologies of World Ocean Atlas 2013 (WOA13) and the PHC3.0 are compared with real observations from the N-ICE2015 area between 1998 and 2013 (REALWOA) and observations from the Fram and Nautilus expeditions as described in Chapter 2.2. Green colours indicate gridded and interpolated climatologies, while blue colours indicate profiles.

(Fig. 3.8. This study will mainly analyse the PHC3.0 and WOA 2013 as historical data sets, but comparisons will also be made to other observations from the World Ocean Atlas Database (Fig. 3.6).

The PHC3.0 is a combination of the global 1998 WOA (Antonov et al., 1998) and the National Snow and Ice Data Center's Environmental Working Group Joint U.S.-Russian Atlas of the Arctic Ocean (AOA) (Timokhov and Tanis, 1997), and selected Canadian observations provided by the Bedford Institute of Oceanography. The climatology provides temperature and salinity data at 1 ° x 1 ° intervals, down to a depth of 5500m, at 33 incremental depths (0-1200 m) and with a coverage in time from 1948 to 1998. The product gives both monthly, seasonal and annual fields. PHC3.0 is the third and latest update of the original PHC2.0 and was published in 2005 (Steele et al., 2001). Updates from the PHC2.0 2001 version include the elimination of discontinuities, correction of density inversions and a new optimal interpolation method (Steele, 2003).

Figure 3.8 a) shows the distribution of all historical surface temperature observations used in the 1998 WOA. Two periods are shown: March-May and July-September. From this figure it is clear that the data in the Arctic Ocean are scarce, although the situation is better in the summer than in winter. Figure 3.8 b) also shows the distribution and availability of data points from the AOA in the Arctic Ocean for the time period 1950-89. Many of these measurements were collected on year-round Soviet drifting ice camps (the "North Pole stations"), as part of an annual aircraft-based spring time survey (the "Sever" project), and from American autonomous drifting buoys (Echert et al., 1989). Most observations were taken in the 1970s and 1980s, and were put together for the purpose of disseminating previously classified data from the region (Steele et al., 2001). It appears that the AOA fills some of the gaps in the WOA data set, and therefore the two were merged together using optimal interpolation.

The WOA13 includes more recent data than the PHC3.0 and is therefore included for comparison. Its timespan reaches from 1955 to 2012 and is an expansion of the WOA09

and WOA98. The one degree resolution and depth field is similar to PHC3.0 and WOA98 but it is also possible to get data in quarter degree resolution. New for WOA13 is that it not only includes the objectively analysed mean but also statistical fields such as statistical mean, standard deviations and standard error. In the N-ICE2015 area the total number of casts in WOA13 after 1998 was 4092 spread over 44 different cruises/drifts. The number of observations included in WOA13 in our region of interest before 1998 was a total of 4944 casts spread over 267 different cruises/drifts. Although WOA13 does not include EWG's AOA, it contains a number of observations more recent than the PHC3.0 and is therefore included in this study. Two datasets are downloaded from the World Ocean Atlas; one is the interpolated and gridded climatology (WOA13) and the other are raw, not interpolated or gridded observations in our region from 1998 to 2013 (hereafter referred to as REALWOA)(4092 casts). For putting the thesis in a historical context a short comparison is made with observations from the Fram and Nautilus expeditions as mentioned in section 2.2.

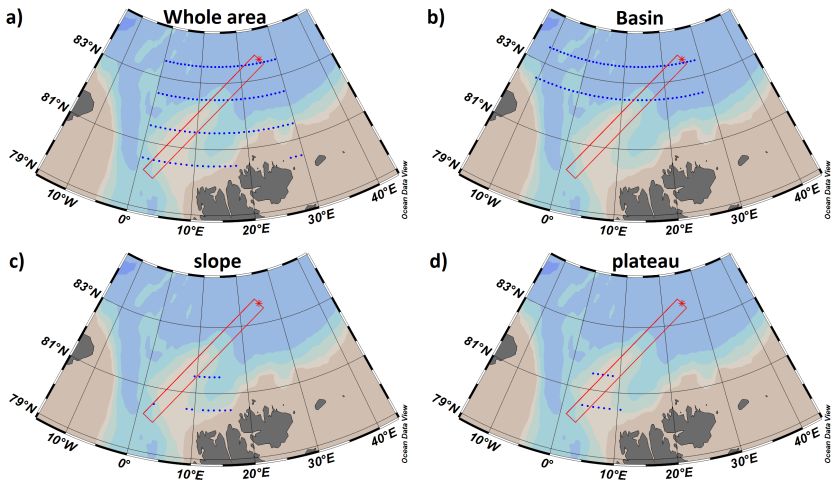

Figure 3.7: Maps showing the gridded climatological data that has been spatially averaged for our climatology. Panel a) the whole N-ICE2015 area, b) Basin, c) Slope and d) the Plateau as defined in section 3.1. The red box marks the approximate area of the N-ICE2015 drift. The blue dots is each horizontally averaged grid point with a mean climatological "vertical profile".

Analysis of the PHC3.0 climatology

The PHC3.0 climatology set was analysed using the visualisation program Ocean Data View (ODV). Seasonal and monthly data were downloaded and divided in four distinct subsets (Whole Area, Yermak Plateau (16 grid points), Nansen Basin (91 grid points) and Slope(15 gridpoints)) following the depth criteria defined in Chapter 3.2.1 (Fig. 3.7). From each of these subsets a mean climatological "vertical profile" of the gridded field was calculated. Following this calculation the standard deviation (σ) was also calculated for the different depths using the standard definition:

$$\sigma = \sqrt{\frac{1}{N}[(x_1 - \mu)^2 + (x_2 - \mu)^2 + ... + (x_N - \mu)^2]}, \quad \mu = \frac{1}{N}(x_1 + ... + x_N). \tag{3.1}$$

Here N was the number of profiles, and $x_1, x_2, ..$ the finite data set of observations at every depth level. The climatological means were investigated, and properties such as heat content, freshwater content, AW core temperature, AW depth and mixed layer depth were calculated. These results have been compared to the observations from the N-ICE2015 campaign.

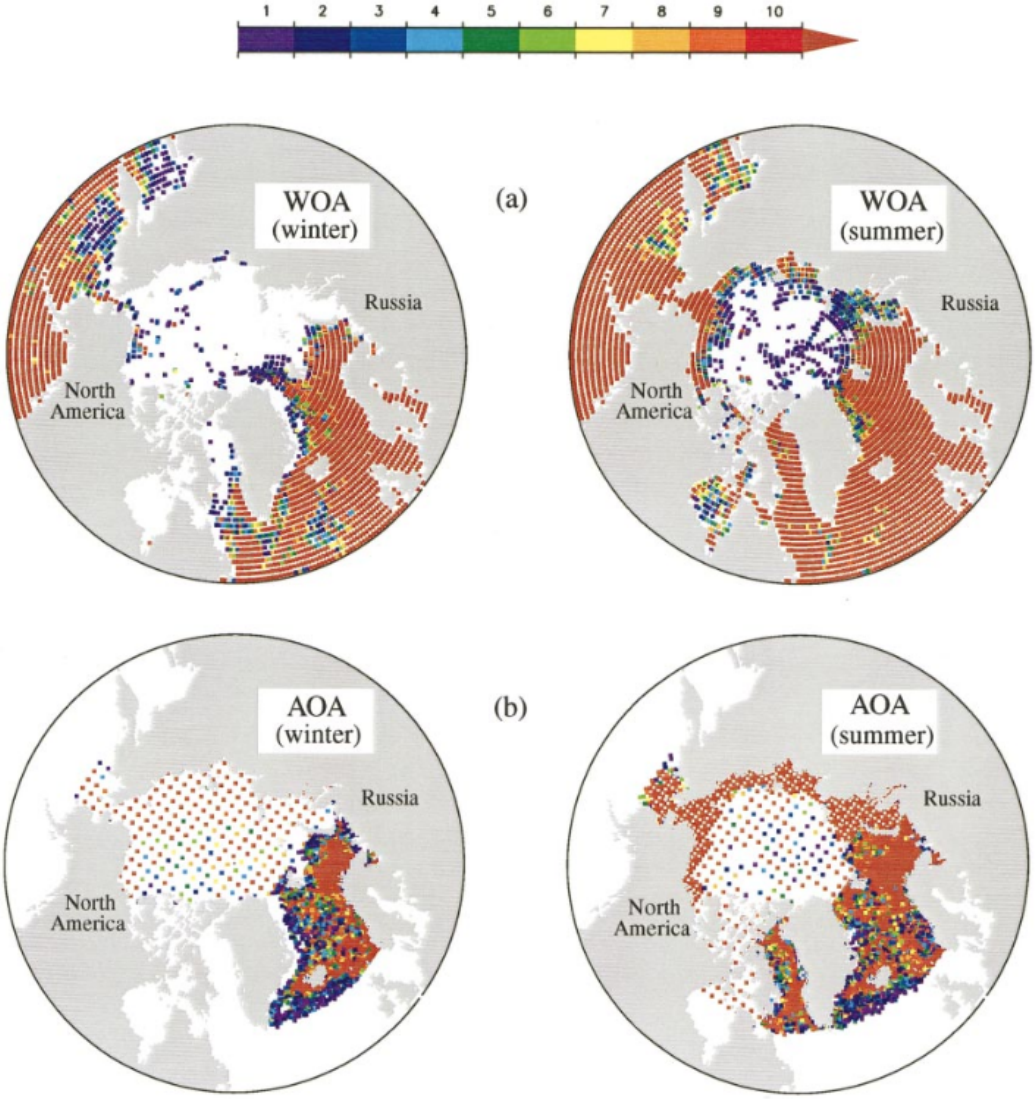

Figure 3.8: Available observations in the PHC3.0 climatology: number of surface temperature observations in the Arctic Ocean (color scale) used in a) WOA98 Antonov et al. (1998) and b) Arctic Ocean Atlas (AOA) Timokhov and Tanis (1997). The AOA provides gridded interpolated products for winter (Mar-May) and summer (Jul-Sep) averages; these definitions have also been used for the WOA98 data. Figure from: Steele et al. (2001).

Analysis of the World Ocean Atlas 2013 climatology

The datasets from WOA13 and the observations from the REALWOA dataset were analysed in similar manner as the PHC climatology. REALWOA was also binned regionally. This dataset consisted of data obtained from 44 different cruises/platforms

and a total of 4092 casts. On these cruises most data were obtained during spring and summer but some data were obtained during winter, especially in the southern part of the N-ICE2015 area and Plateau. No winter observations are available for the Slope, and little for the Basin. However, one drifter from the North Pole Environmental Observatory (NPEO) drifted in 2003 through the N-ICE2015 area and straight over the Plateau, following closely the Lance drift track in the time period of December-March. This is one of the few other winter observations from this area and is therefore included in our comparison. There may have been other cruises in the N-ICE2015 area, also during winter, from which observations are not included in any of these datasets because they are not available.

Historical Fram Strait measurements

Historical measurements of AW core-temperature have been performed yearly since 1977 by the Norwegian Institute of Marine Research (IMR) in the southern part of Fram Strait, west of Sørkapp (see Fig. 4.7). Measurements are taken at this station yearly in August. Data were downloaded from the ICES Report on Ocean Climate (IROC)(Beszczynska-Möller and Stephen R. Dye, 2006) web page.

Fram and Nautilus observations

Profiles of temperature and salinity from the Fram expedition led by Nansen (1893-1895) (Collett and Nansen, 1901) and submarine Nautilus expedition led by Sir Hubert Wilkins and described by oceanographer Harald Ulrik Sverdrup in 1931 (Wilkins et al., 1931) are made available through the World Ocean Atlas Database as Excel documents.

3.3 Models

3.3.1 1-D Sea ice growth model

A one-dimensional sea ice growth and convection model was used and adapted to investigate the effect of oceanic heat on a yearly sea ice growth cycle. The model, created by Elin Darelius and Frank Nilsen at UNIS in 2004, is based on the empirical ice growth relationship from Stefan's Law as discussed in the previous chapter, combined with theoretical calculations of convection depth as described by Gade (1994) (Darelius and Nilsen, 2004). The model is formulated for a vertical water column and does not take into account horizontal advection of water and ice. Atmospheric temperature above the ocean surface is the only forcing. Initial conditions are initial temperature and salinity profiles, initial ice thickness and snow depth. The model output gives full temperature, salinity and sea ice thickness development over time. The simulation process can be divided into three main stages which are repeated continuously; 1. Cooling, 2. Freezing, 3. Brine release and convection.

1. Cooling:
The surface mixed layer of the initial water column is cooled down to the freezing point due to cold air temperatures. If there is no mixed layer present, a theoretical wind forced mixed layer of 10 m is assumed and created. The heat loss at the water surface is estimated as:

$$W_{sensible} = -C_H \cdot \rho_{air} \cdot c_{air} \cdot U_{10}(T_{air} - T_{surface}). \tag{3.2}$$

Here the drag coefficient, C_H, was set to $1.5 \cdot 10^{-3}$, and the density and heat capacity of air, ρ_{air} and c_{air} is 1.275 kg/m^3 and 1004 J/K/kg respectively. The wind forcing (U_{10}) is set to a constant mean of 7 m/s. Real observed wind speed could be added, but atmospheric data from the ship were made available too late for this study. The flux is assumed to first cool down the water column. Then, when cooled down to the freezing point, the flux initiates freezing, i.e. the up-mixed heat from the last time-step has to be "used up" before freezing can start.

2. Freezing:
Once the surface layer is cooled down to its freezing point, freezing will start. The ice sheet is in thermal balance with its surroundings and thus the ice growth can be calculated following equation 2.5. During freezing it is assumed that there is no thermal inertia in the ice, no internal heat source and the surface temperature equals the surface air temperature. The ocean heat flux will either melt ice at the bottom of the ice-cover or be conducted up through the ice. The model is capable of simulating the effect of an insulating snow cover on the ice However, this is neglected in this study because we are more interested in the sensitivity of ice regarding oceanic changes.

3. Brine release and convection:
When seawater freezes, about one third of the dissolved salt is incorporated into the ice, while the rest is released into the underlying water, as described in Chapter 2.3. Vertical circulation or convection is induced by the sinking cold and saline brine that mixes with the underlying water, thereby increasing its salinity and density. As the density of the top-layer increases, it will gradually deepen to a depth were the density is equal to the density of the new mixed layer or deeper. This process can also bring up heat into the mixed layer. For calculation of the convection depth, the model allows two different predictions; Zubov-Defant (ZD) and Ball Kraus Turner (BKT). Theory and observations indicate that the true convection depth is somewhere in between the ZD and the BKT predictions (Darelius and Nilsen, 2004). For this study we have chosen to only use the BKT model because it is easiest to adapt while modifying the initialization. It also gives a slightly more realistic explanation to the process. In the BKT prediction all potential energy in the system is conserved and none is lost to turbulence. The sinking water penetrates the pycnocline and its potential energy is transformed first to kinetic energy and then back to potential energy as heavier water is lifted up and

mixed. The convection depth D is chosen such that $E_{before} - E_{after}$ is minimized (Ball, 1960; Kraus and Turner, 1967).

$$E_{before} = Q_s \cdot D + \int_0^D z\rho(z)gdz, \tag{3.3}$$

$$E_{after} = z\rho' gdz = \frac{\rho' gD}{2}, \tag{3.4}$$

where Q_s is the flux of the salt from the ice, D is the convection depth and ρ' is the new density after mixing.

Once the convection depth is calculated new salinity and temperature profiles are found and the amount of up-mixed heat is calculated using equation 3.5. This, together with new ice thickness, is stored, and the whole process is repeated.

$$F_{upmixed} = \sum \rho c_p (T(z_{convection} - T_{freeze}(z_{convection}))\Delta z. \tag{3.5}$$

The model assumptions and simplifications have made the ice growth and related convection as simple as possible. Some important assumptions are:

- **One dimension:** The model assumes no lateral exchange of heat or salt. Attempts were made to advect in heat at intermediate depth but without good results.
- **Snow:** Snow varies extensively in value, but is neglected i this study.
- **Stefan's Law:** Penetrating radiation, internal heat sources and thermal inertia (Stefan, 1889) are assumed small enough to ignore.
- **Surface temperature:** The surface temperature is assumed equal to the surface air temperature which in this study is set to constant -20°C, similar to the mean observation from N-ICE2015.
- **Pressure dependency:** Effect of pressure on density is neglected.
- **Sea ice properties:** Latent heat of fusion and conductivity are treated as constants, while they vary with sea ice salinity and temperature in nature.
- **Conservation of volume:** Depth is kept constant; no water is removed when ice is frozen but instead salt is added.
- **Melting:** No melting is considered when enough heat is mixed upwards. The heat mixed upwards only limits ice growth. Melting of ice would create a stable fresh layer under the ice that is not captured in the model. The model is therefore representative for the N-ICE2015 area until May 25 when melting was observed.

1-D Model initialisation

The model was initialised with several different oceanic columns. Baseline mean temperature and salinity profiles from the PHC3.0 climatalogy for the N-ICE2015 area were

used. Subsequently a comparison was made with mean profiles from the N-ICE2015 observations for the whole area, Basin, Slope and Plateau.

For further analysis the PHC3.0 standard profiles were modified. A set of profiles was created where the AW ($T > 0$°C) in the PHC3.0 profiles was gradually warmed by 0.1 °C steps up to 2 °C. This warming is not necessarily realistic but done to study the effect warming AW could have on the ice growth process. By increasing the temperature, density decreases, and to prevent the column from becoming vertically unstable salt was added. For each bin the difference in density due to the temperature increase was calculated and compensated for by adding the exact amount of salt to keep the density stable ($\rho_{difference} = f(T_{increase}, S_{increase})$). The salinity difference was calculated using the equation of state in the GSW-toolbox in MATLAB. Another calculation was performed to find the depth at which the AW would be stable if heated but no salt was added ($z_{stable} = z_{\rho=\rho(T_{new},S_{old})}$). Here z_ρ is the extent of the upper limit of the AW.

Secondly, a new set of initial profiles was created where the AW layer is lifted up from 124 m (PHC3.0) with 10 m increments and brought closer to the surface. These profiles were made by cutting the column above the AW layer, keeping all surface properties intact. The model code had to be slightly adapted to function with the modified inputs. For example; the method for finding the depth of the mixed layer in each previous step before cooling starts had to be changed. Here a density gradient definition was added that will be explained further in section 3.4.4. The effect of different initial ice thickness was also calculated. More detailed specifics about the model and its calculations are given in Darelius and Nilsen (2004).

3.3.2 NorESM model

Fully coupled 3-D model simulations were also used in this study to assist with the evaluation of AW variability and its influence on the Arctic sea ice cover. The Norwegian Earth System Model (NorESM) is a global, coupled model system for the physical climate system. The model can be run with various degrees of interactions with bio-geo-chemical processes in the earth system (Bentsen et al., 2013). NorESM was developed as a multi-institutional research project EarthClim (`http://folk.uib.no/ngfhd/EarthClim/`) and is based upon the development of the Bergen Climate Model (Furevik et al. (2003); Otteraa et al. (2009)) at the Bjerknes Center for Climate Research, and aerosol cloud radiation interaction schemes from the Meteorological Institute in Oslo (Seland et al., 2008).

The model also builds upon the Community Climate System Model version 4 (CCSM4) (Gent et al., 2011) but is different because of the isopycnic coordinate ocean model and the advanced chemistry interaction schemes. In general the ocean and ice components have a 1° resolution, but NorESM has high resolution in the Svalbard region ($\approx$ 0.5°)(Alexeev et al., 2013). NorESM is one of fifteen global ocean-sea-ice models in the framework of the Coordinated Ocean-ice Reference Experiments, phase II (CORE-II). Most of these models are the ocean and sea ice components in the Coupled Model Intercomparison Project Phase 5 (CMIP5) (Ilıcak et al., 2016). NorESM historical

CMIP5 (Taylor et al., 2012) simulations show good results for Arctic sea ice in general (Langehaug et al., 2013), and have previously indicated sea ice bottom melting near Svalbard (Ivanov et al., 2016). Simulations were performed at the Bjerknes Center for Climate Research at the University of Bergen, and analysed at the Bjerknes Center. The historical CMIP5 ensambles CV1 was used in this study.

Simulations were retrieved from the data disks at the Geophysical Institute of the University of Bergen and analysed on the server *SKD/cyclone* because of the large amount of data. Temperature, salinity, current velocity and sea ice bottom melting were analysed. The model run was performed with time steps of 15 minutes but variables are stored as monthly averages. Yearly means were made of data ranging from 1950 to 2005. Data were analysed spatially, and spatially averaged for smaller regions such as the N-ICE2015 area and Fram Strait. AW depth and core-temperature were investigated from the model results. AW depth has a rough resolution as the the model operates with 70 depth levels throughout the whole water column. The depths are isopycnal levels that are later interpolated and binned at given depth levels. Near the surface, vertical spacing between the levels is 5 m, below 30 m this increases to 10 m, below 50 m it increases to 12.5 m and below 150 m it increases to 25 m. At greater depths the layer thickness increases even more. (The analysis of AW-depth is therefore not as accurate as from observational data and is therefore difficult to compare). The AW core temperature is calculated as the highest temperature found from all the different layers, and this is also an approximation. Mixed layer depth was not captured well by the model due to the rough vertical spacing.

Spatial correlation between variables were computed by reshaping the 2-D fields to vectors and back, to investigate temporal changes in AW characteristics and trends, to study the current velocity field in the N-ICE2015 area, and to correlate changes in AW with changes in the Arctic sea ice cover.

3.3.3 Tidal Analysis

A harmonic tidal analysis was done for the given times and positions of the Long Ranger current velocity measurements, using the AOTIM5-Inverse tidal model developed by the Earth and Space Research Institute `https://www.esr.org/polar_tide_models/Model_AOTIM5.html` (Padman and Erofeeva, 2004). This is a high resolution (5-km grid) linear-dynamics model of Arctic Ocean barotropic tides. Accompanied with the Matlab TMD Toolbox, the model simulates a mean tidal velocity of the most energetic tides (M2, S2, O1 and K1)(Fig. 3.9). This model specifically takes into account local bathymetry at higher resolution than previous models. Tidal velocity was calculated along the N-ICE2015 drift tracks and compared with observed current velocity.

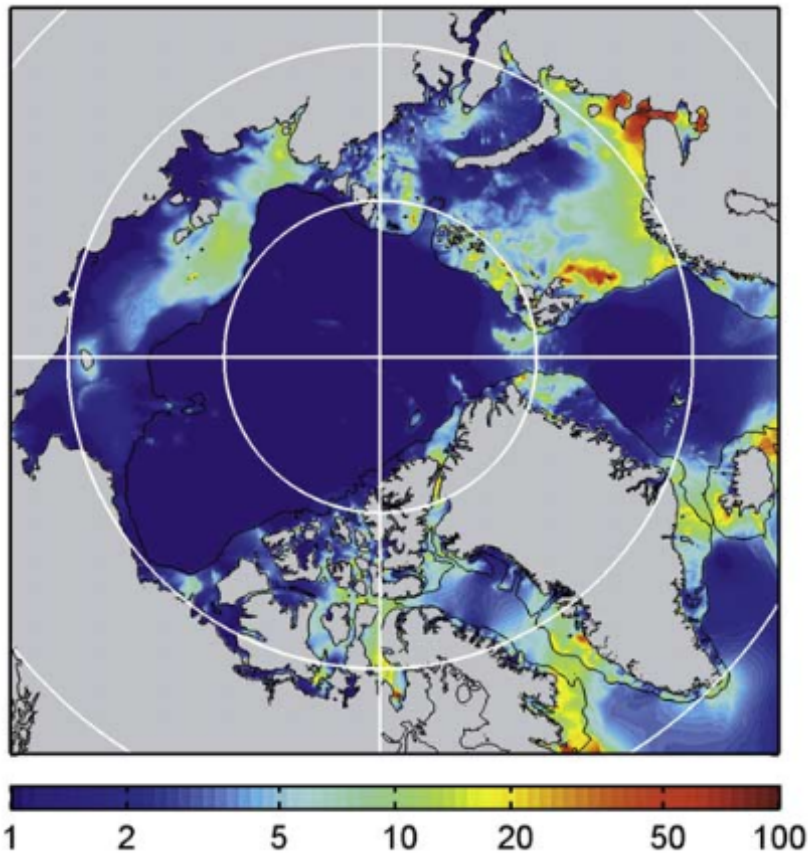

Figure 3.9: Mean tidal current speed (cm/s) based on simulating 14 days of hourly total tidal speed from the main constituent in the inverse AOTIM5. Figure from Padman and Erofeeva (2004).

3.4 Calculations and data analysis

3.4.1 TEOS-10

All hydrographic data in this study is presented in accordance to the International Thermodynamic Equation Of State - 2010 (TEOS-10) framework (McDougall et al., 2010). In practice this means that salinity is presented as absolute salinity, S_A, and temperature as conservative temperature, Θ. It has previously been common to use the MATLAB "SEAWATER" toolbox which was based on the EOS-80 properties of seawater (Fofonoff, 1985). This toolbox has now been replaced by the Gibbs SeaWater (GSW) Oceanographic Toolbox developed by the SCOR/IAPSO Working Group 127 and adopted by the Intergovernmental Oceanographic Commission (IOC) to be used in future scientific publications (McDougall and Barker, 2011).

The new TEOS-10 framework allows for all the thermodynamic properties of pure water, ice, seawater and moist air to be evaluated in a self-consistent manner. In this framework, the effects of the variations in salinity composition around the world oceans are accounted for. These spatial variations of salt composition cause density differences that are equivalent to at least ten times the precision of Practical Salinity (psu) being

measured (McDougall and Barker, 2011). The Gibbs function approach of TEOS-10 allows the calculation of internal energy, entropy, enthalpy, potential enthalpy and the chemical potentials of seawater as well as the freezing temperature, and the latent heats of melting and of evaporation.

The salinity argument introduced by TEOS-10, Absolute Salinity, is measured in SI units [g/kg] and is together with the newly introduced variable Conservative Temperature, (°C) dependent on longitude and latitude. Salinity is still measured and stored as Practical Salinity S_p, but for calculations or visualization it is converted to Absolute Salinity using the toolbox function **gsw-SA-from-SP**. This function interpolates the global Absolute Salinity Anomaly Ratio (R^δ) data set and then uses this to calculate S_A from S_p.

$$S_A = \frac{35.16504 g kg^{-1}}{35} S_p (1 + R^\delta). \tag{3.6}$$

In this expression (35.16504 $\mathrm{gkg}^{-1}/35$)S_p is the reference salinity, which is the best estimate of Absolute Salinity of a Standard Seawater sample.

For the past 30 years, under EOS-80 it has been common to present the "raw" data of Practical Salinity S_p, in situ temperature T and pressure p and to use an algorithm to calculate potential temperature and density. The new Conservative Temperature Θ is similar to potential temperature. In both cases one takes a seawater parcel at an arbitrary pressure and decreases the pressure on the parcel in an adiabatic and isohaline manner until the pressure equals surface pressure $p = 0$ dbar. The temperature at the end of this process is defined as the potential temperature. The enthalpy at the end of this experiment is defined to be the potential enthalpy h_0, and Conservative Temperature Θ is the potential enthalpy divided by the fixed heat capacity $c_p^0 = 3991.86795711963$ $\mathrm{Jkg}^{-1}\mathrm{K}^{-1}$. The Conservative Temperature has the advantage of more accurately representing the "heat content" of seawater (McDougall and Barker, 2011) and is calculated using the toolbox function **gsw-CT-from-t**.

Potential enthalpy (McDougall, 2003) is defined as the sum of internal energy and is related to in situ enthalpy, h, by

$$h_0(S, \theta, p_r) = h(S, \theta, p) - \int_{p_r}^{p} 1/\rho(S, \theta, p')dp'. \tag{3.7}$$

Figure 3.10 shows the differences between TEOS-10 and EOS-80 for the N-ICE2015 data in a T-S diagram. The difference between potential temperature and Conservative Temperature can be as large as $\Delta\Theta = 1.4$°C but is typically no more than ± 0.1°C. The largest influence of the variable seawater composition occurs in the Northern Pacific and the anomalies are relatively small in the Arctic.

3.4.2 CTD data analysis

A detailed quality control of T-S properties from both the ship and on-ice CTD was performed. The ship's CTD profiles were checked manually and huge spikes near the

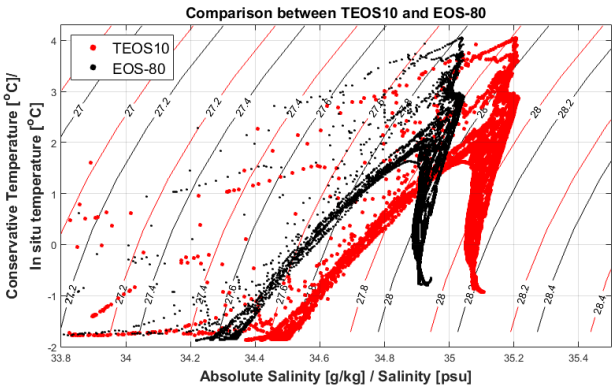

Figure 3.10: T-S diagram showing both the TEOS-10 equation of state (McDougall et al., 2010) and the EOS-80 equation of state (Fofonoff, 1985) for the N-ICE2015 ship CTD data.

surface, likely due to bubbles or the instrument not being rinsed before deployment, were removed. The ship's CTD data were also calibrated after the sensors were recalibrated by the manufacturer. Stations that were taken during steaming in between floes while not attached to a drifting floe were ignored. The on-ice CTD salinity had less accuracy than the ship's CTD sensor but also had a large drift throughout the period. The drift was nearly linear. Several methods were attempted to correct these salinity profiles. Calibration was tried against the closest ship CTD profile, and also to force the surface measurements to be at the freezing point, with no success. Finally we chose to calculate the mean error between the laboratory salinity measured from the bottles from each profile. The vertical error for each profile was near uniform allowing us to subtract the mean error from the whole profile (panel b), Fig. 3.11). After calibration, the error was below 0.05, from previously 0.45, but the sensor accuracy is still less than the ship CTD sensors. Another likely reason for the accuracy to be lower is that the system is not pumped. Some profiles from the on-ice CTD had salinity measurements that were completely off and could not be fixed. These showed large instabilities and were likely because the sensors were not rinsed properly or something got stuck in the sensor. These profiles were removed completely (Fig. 3.13).

To create sections of the on-ice CTD data from the drift, the data were interpolated first over depth to 400 m and then over time. Temporal coverage was evaluated and a daily interpolation chosen. The right panels in figure 3.12 give an example of temperature measurements before interpolation for the four drifts. Panels on the left side present the same data after interpolation. A quality control of this interpolation means checking that no features not present in the original data have occurred due to interpolation. In our case interpolation was overall satisfactory.

3.4.3 Atlantic Water characteristics from observations

The depth of the Atlantic Layer is defined as the depth of the upper 0°C isotherm. Where the maximum Conservative Temperature is found, we define the depth of the AW core, and AW layer thickness is then the distance between the upper and lower 0°C

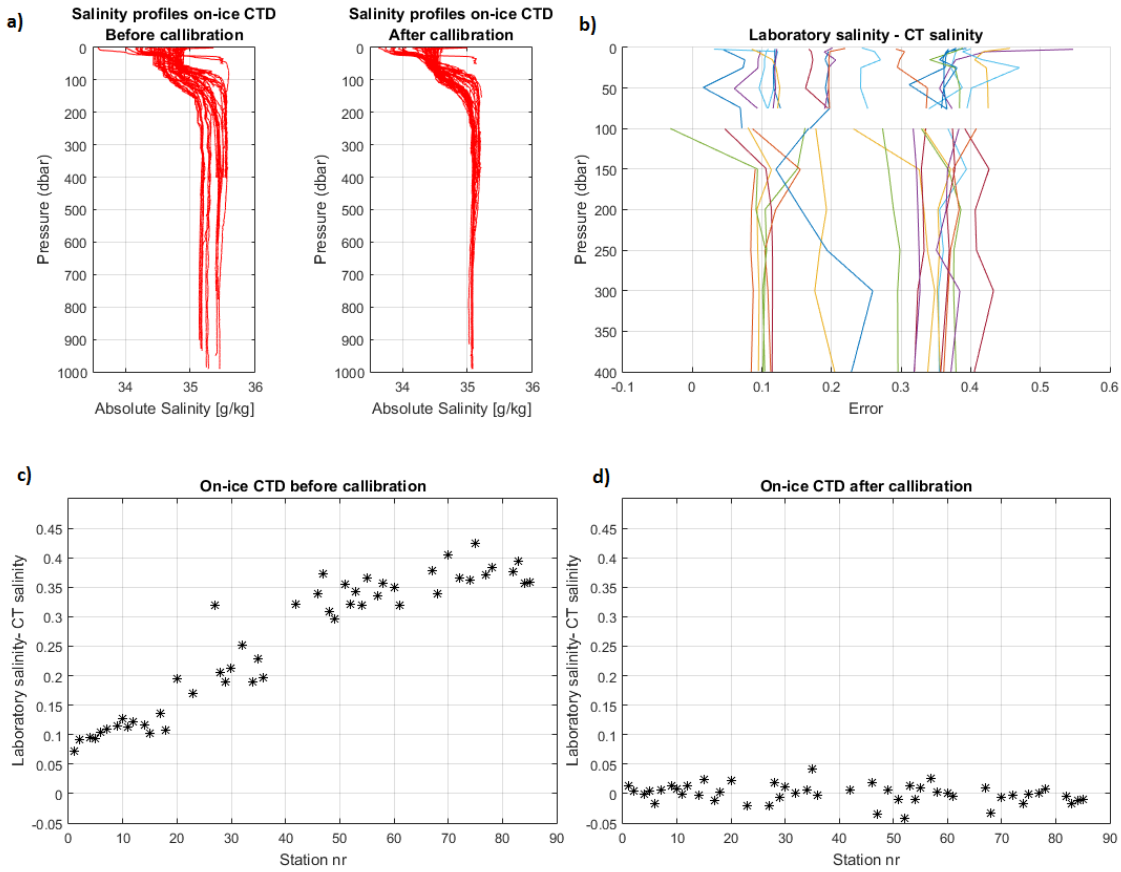

Figure 3.11: a) Salinity profiles from on-ice CTD before and after calibration against laboratory salinity from bottles. b) Vertical error between laboratory salinity and CT salinity at given depths from different bottles. c) Vertical mean error in salinity over time d) Vertical mean error in salinity over time after calibration.

isotherms (Rudels et al., 2000; Talley et al., 2012).

3.4.4 Mixed layer depth

Following the gradient definition of Nilsen and Falck (2006), the mixed layer depth is defined as the depth where the density gradient exceeds a given value, for density

$$\frac{\Delta\sigma_t}{\Delta z} > \left(\frac{\delta\sigma_t}{\delta z}\right)_C, \tag{3.8}$$

where $\Delta\sigma_t$ is the difference of the density anomaly ($\sigma_t = \rho - 1000\text{kgm}^{-3}$) over a vertical distance (z), and $(\delta\sigma_t/\delta z)_C$) is the specified gradient criterion (C stands for criterion). The specific gradient criterion was in our study set to 0.01 $\text{kgm}^{(-3)}$.

For all CTD profiles this gradient criterion was checked manually. In cases where the salinity and temperature profiles do not give a conclusive answer, the mixed layer depth is set manually from (subjective) inspection of the density profile following Pickart and Clarke (2002). Especially during the melt season after the 25th of May, manual inspection was used more because the density gradient exceeded the criterion too quickly.

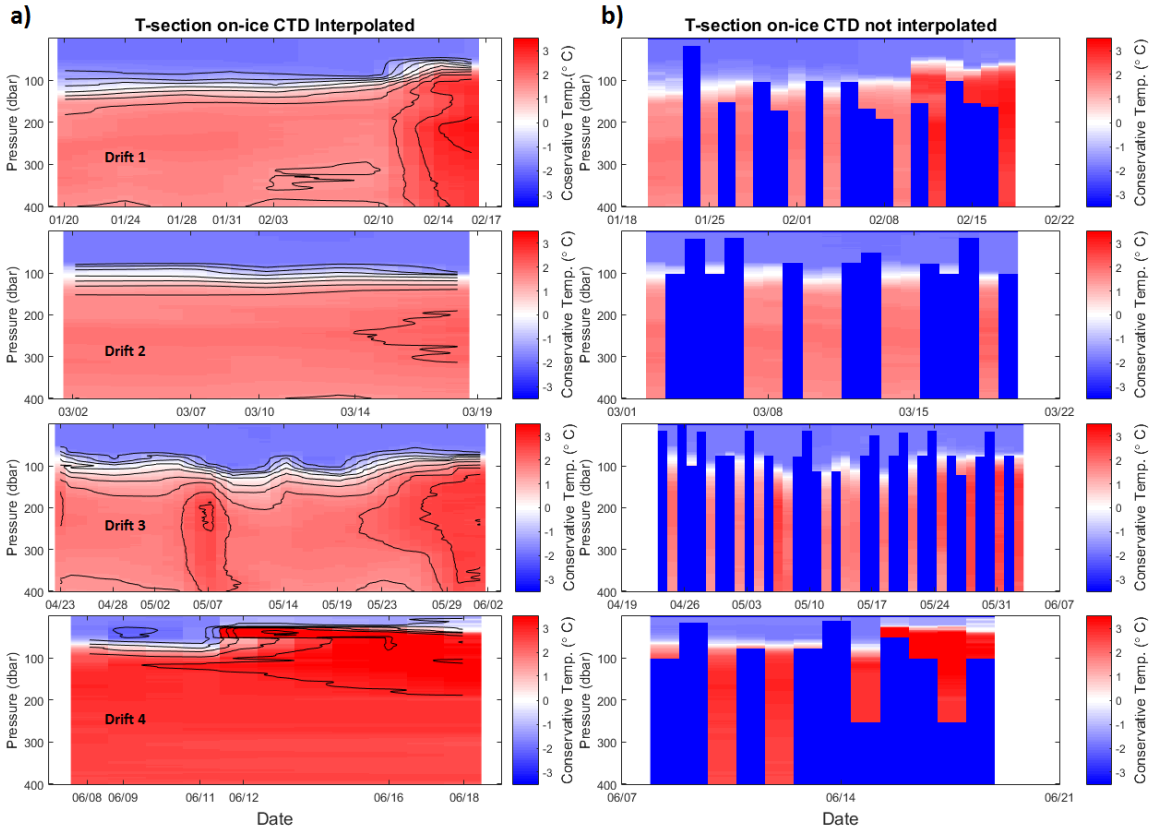

Figure 3.12: a) Daily and depth interpolated temperature sections for all four drifts from the on-ice CTD. b) Non-interpolated temperature sections for all four drifts from the on-ice CTD. Blue squares denote NaN values, where no observations exist.

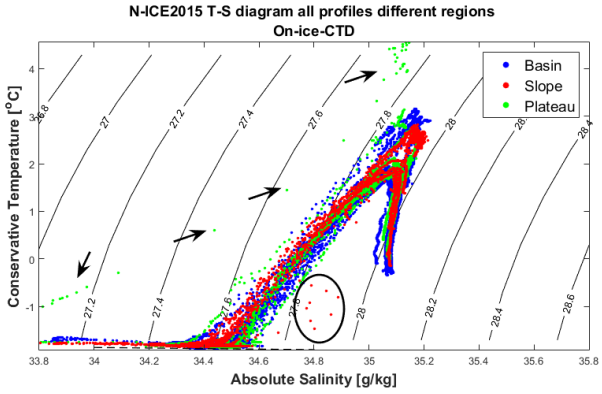

Figure 3.13: Example of manual quality control after despiking and calibration: Regional T-S diagram from the on-ice CTD data showing one bad profile (circled) that was removed. Arrows point at a profile that was particularly examined because of the large difference from the rest, this was found to be a normal profile but with very warm surface waters because it was the last profile taken in June.

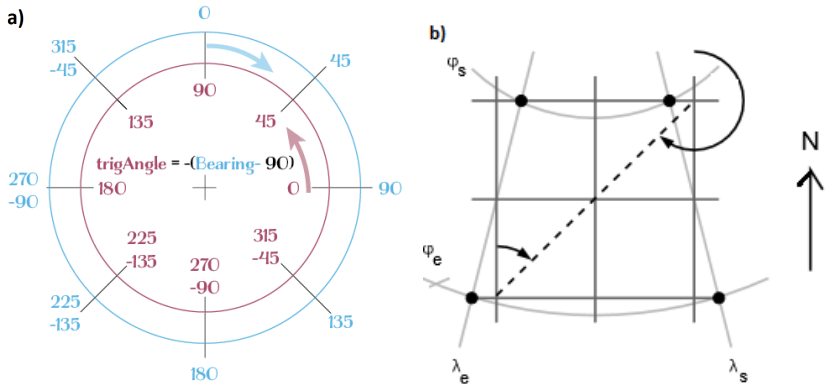

Figure 3.14: a) Sketch illustrating the difference between current direction in degrees north (bearing) and the cartesian coordinate system. Figure from `stackoverflow.com`. *b) Sketch illustrating the problem of placing a rectangular grid on spherical coordinates which explains why we have to use equation 3.12. Figure from* `http://www.eas.slu.edu/`.

Attempts with different criteria were tried but manual inspection remained the best solution.

3.4.5 Long Ranger ADCP analysis

Absolute velocity (V) and current direction (θ) were calculated from the u and v vectors obtained from the Long Ranger ADCP using the following:

$$V = \sqrt{|v|^2 + |u|^2}. \tag{3.9}$$

$$\theta = 90 - ((tan^{-1}(\frac{u}{v})) \cdot 180 \cdot \pi), \theta < 0 = \theta + 360 \tag{3.10}$$

Here θ is the current direction in degrees north (° N) defined with $\theta = 90°$ as flow directly towards the East (also called the bearing)(Fig. 3.14). The drift speed of the ship was calculated using the ship navigational data, taking into account the spherical coordinates and distance between the given coordinates for each time step;

$$\Delta x = 111195(m/°)(\phi_a - \phi_b), \Delta y = 111195(m/deg)(\lambda_a - \lambda_b)cos(\frac{(\phi_a - \phi_b)}{2}) \tag{3.11}$$

$$V = \frac{\Delta S}{\Delta t} = \frac{\sqrt{\Delta x^2 + \Delta y^2}}{\Delta t}. \tag{3.12}$$

A running mean of the current data were calculated using the nan-ignoring 24 hour box window in the Matlab code `nanmoving_average`:

$$Y(i) = \sum \frac{X(j)}{2M+1}, j = (i - M) : (i + M), i = 1 : length(X) \tag{3.13}$$

The shear between the uppermost water layer and ice was calculated as:

$$V_{ship/ice}(relative\ to\ ground) - V_{water}(relative\ to\ ground). \tag{3.14}$$

This was compared to the not-dedrifted Long Ranger velocity data that should be giving the same result.

3.4.6 Heat and freshwater content

Using the N-ICE2015 hydrographic data, heat content, also called enthalpy, was calculated. This is defined as the total heat stored in the water mass and equals the sum of the internal energy in the system and the product of the volume and pressure. The heat content was calculated relative to a reference water with density $\rho_{ref} = \rho(T_{ref}, S_{ref})$ as

$$H = \rho_{ref} c_p \int_{h1}^{h2} (T - T_{ref}) dz, \tag{3.15}$$

where h1 and h2 are the upper and lower boundaries of the different layers. Here T is the measured *in situ* temperature, T_{ref} the reference temperature, S_{ref} the reference salinity, ρ_{ref} the reference density, and $c_p = c_p(T_{ref}, S_{ref}, p = 0)$ is the specific heat of seawater at the surface ($3991,87$ JK$^{\circ -1}$kg^{-1}). The reference temperature was defined as 0°C as this defines the top of the AW layer. As reference salinity 35 g/kg was adopted, because this is a typical mean salinity for inflowing AW. For the upper layer the integration was performed from the surface (h1) down to an integration depth (h2) of 200 m. Because the surface layer is colder than the AW and the reference temperature, heat content values are generally negative. Only negative values for heat content were counted, i.e. only the heat in the layer above the reference isotherm and hence above the AW layer. The integration was done with the trapezoidal method using the Matlab function *trapz*. The function *trapz* performs numerical integration by approximating the integration over an interval by breaking down the area into trapezoids with more easily computable areas. The approximation is given by:

$$\int_a^b f(z)dz \approx \frac{b-a}{2N} \sum_{n=1}^{N} (f(z_n) + f(z_{n+1})) = \frac{b-a}{2N} [f(z_1) + 2f(z_2) + ... + 2f(z_N) + f(z_{N+1})], \tag{3.16}$$

where the spacing between each point is equal to the scalar value $\frac{b-a}{2N}$ and x is the depth.

The freshwater content was calculated in a similar fashion as the heat content using

$$F = \int_{h1}^{h2} \frac{S_{ref} - S}{S} dz, \tag{3.17}$$

where S is the Absolute Salinity and h1 and h2 are the upper and lower boundaries of the different layers investigated. Freshwater content was calculated for an upper layer from the surface (h1) down to the depth of the reference salinity. The integration depth was set to be constant at 200 m (h2) but only positive values of freshwater content down to the depth of the reference salinity (35 g/kg) were counted. This results in a value of total freshwater content in the layer above the reference salinity that is not affected by upward or downward moving AW.

3.4.7 Stability

The Brunt-Väisälä frequency (N), or buoyancy frequency was calculated as:

$$N^2 = -\frac{g}{\rho_0} \frac{\delta \rho(z)}{\delta z}. \tag{3.18}$$

Here $\frac{\delta\rho(z)}{\delta z}$ is the density gradient, g the standard gravitational acceleration ($g \approx 9.81\text{m/s}^2$) and ρ_0 the mean density of seawater at the surface. The Brunt-Väisälä frequency is the angular frequency at which a vertically displaced parcel will oscillate within a vertically stable environment. Regions with high buoyancy frequency are vertically more stable. If acceleration is returned to the initial position ($N^2 > 0$), the stratification is said to be stable. If the acceleration is away from the initial position ($N^2 < 0$), the stratification is unstable. In this case overturning or convection generally ensues (Thorpe, 2007).

3.4.8 Turbulent Instrument Cluster (TIC) analysis

In this study 3 hour average values of calculated heat flux and friction velocity at 1 m below the lower sea ice boundary were used from the TIC. Data were provided by Algot Peterson, who performed the calculations.
Heat is transferred from one level in a fluid to another in a similar way as momentum. The vertical flux of heat depends on the ability of eddies to carry water of higher temperature upwards or water of lower temperature downwards, which is often inhibited by buoyancy forces derived from stratification. Heat fluxes are often derived from parametrizations, but in our study they are calculated directly from TIC covariance measurements using:

$$H_f = \rho c_p < T'w' >, \tag{3.19}$$

where T' is the temperature fluctuation about a temporal mean (15 min), ρ the seawater density, and c_p the specific heat capacity of seawater. The product $\rho c_p T'$ is the heat fluctuation per unit volume of fluid corresponding to the temperature change T', and multiplied with the deviatory vertical speed w' it gives the vertical flux of heat carried upwards in W/m^2 (Thorpe, 2007).

Friction velocity is a form of shear stress, or Reynolds stress which is rewritten using units of velocity. Its stress is equal to the mean rate of transfer of momentum across a surface by turbulent motion and hence a direct measurement of turbulence. The friction velocity is calculated directly from covariance of horizontal and vertical velocity:

$$u^* = \sqrt[4]{(< u'w' >)^2 + (< v'w' >)^2}, \tag{3.20}$$

where u, v and w are measured from the ADV on the TIC. TIC data and turbulence measurements are not the main focus of this study and are here used to emphasize some points and to supplement other results.

3.4.9 Linear trend

Linear trends are calculated in a least square sense which minimizes the vertical deviations of the data points from the fitted line (Thomson and Emery, 2004). The coefficient of the first order polynomial gives the slope of the regression line. The coefficient of the polynomial, $\hat{x}$, is given as

$$\hat{x} = \frac{x - \bar{x}}{\theta_x}, \tag{3.21}$$

where $\bar{x}$ is the mean of x and θ_x is the standard deviation of x. The 95 % confidence interval was calculated using the MATLAB `regstats` package and the function `regression_line_ci` downloaded from `mathworks.com`. The trend error was calculated as the smallest and largest possible trend within the 95 % confidence band (Fig. 3.15). *P-values* are extracted from the `regstats` package in order to quantify statistically whether there is any significant relationship between the x and y values. This is done by testing the null hypothesis that the regression coefficient, β, equals zero. If the *p-value* is smaller than 0.05, we have 95% confidence that there is a linear relationship between the x and y values (Hogg et al., 2010).

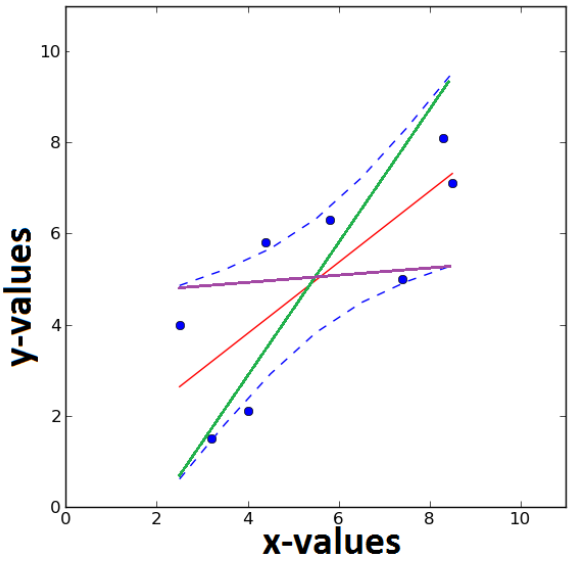

Figure 3.15: Illustration of a linear fit on sample observations (blue dots). The red line is the linear fit and the blue lines denote the 95 % confidence interval. The green line is the largest possible trend within the confidence interval and the purple, the smallest. Figure adapted from `mathworks.com`.

3.4.10 "Gade-line" calculation

A simplified analytical calculation was performed to investigate the near surface salinity after sea ice melting (Chapter 5.2.5). Assuming all heat from a water mass, m_w, is used to melt a mass of sea ice, dm_i, and disregarding heating of ice, conservation of heat gives:

$$cm_w \Delta T_f = L dm_i, \tag{3.22}$$

where c is specific heat capacity of seawater (~ 4000 Jkg^{-1}), L is latent heat of fusion for ice ($\sim 3.3 \cdot 10^5$ Jkg^{-1}), and ΔT is the difference in temperature between the water mass and the freezing temperature below the ice. Conservation of salt gives:

$$dm_i S_i + m_w S_w = (m_w + dm_i)(S_w - \Delta S), \tag{3.23}$$

where S_i is the salinity of the sea ice, S_w is the salinity of the water mass, and ΔS is the change in water mass salinity after melting has occurred. From these two equations we obtain:

$$\Delta S = \frac{S_w - S_i}{(1 + \frac{L}{c\Delta T_f})}. \tag{3.24}$$

Chapter 4

Results

In this chapter results from the N-ICE2015 hydrography and current observations, existing climatologies, the 1-D model, and the NorESM model are presented.

4.1 Hydrography

The hydrographic properties in the N-ICE2015 area are described here, both regionally and seasonally. Figure 4.1 shows a map of the Arctic Ocean with CTD stations from N-ICE2015 for both the ship and on-ice CTD profiles. From these profiles and from the statistics in Table 4.1 we see that the conservative temperature ranges between -1.818 °C and 4.048 °C, and the absolute salinity has values ranging from 32.427 g/kg to 35.214 g/kg. Table 4.1 provides further details about the temperature and salinity measurements. The water column consists of a colder (near freezing) and fresher Polar Surface Water (PSW). Below the well mixed surface layer and a strong thermocline we find a warmer and saltier layer of Atlantic Water (AW) (Table 4.1). Warmest water is found in the AW core that increases up to 4 °C in early June over the Plateau (Fig. 4.3). Deeper below the AW layer we find colder and saltier deep waters.

The distribution of water masses, from the ship and on-ice CTD in T-S space, is shown in Figure 4.2 following the definitions of Rudels et al. (2000). From the T-S diagrams we observe cold PSW and warm PSW (mainly from May on the Yermak Plateau) overlying AW and Modified Atlantic Water (MAW). Below approximately 900 m, Arctic Intermediate Water (AIW) is found with potential density anomalies higher than $\sigma_\theta = 28$. The deeper ship CTD profiles provide evidence of some Canadian Basin Deep Water (CBDW) and Eurasian Basin Deep Water (EBDW) below 1500 m. Scatter in the tail of the deepest measurements in the T-S diagram from the on-ice CTD (Fig. 4.2 b)) is due to the poor quality of the conductivity sensor (Chapter 3.4.2).

An overview of the hydrographic conditions is given in the temporal section shown in Figure 4.3, where the the on-ice CTD data are divided into the four different drift periods. Panels a) and b) clearly show the variation in vertical distribution of salinity and temperature, however, because of the nature of a drift project it is difficult to say whether observed variations are due to temporal or regional changes. A warmer AW layer is observed during drift 4 and it is also closer to the surface. As shown in Figure

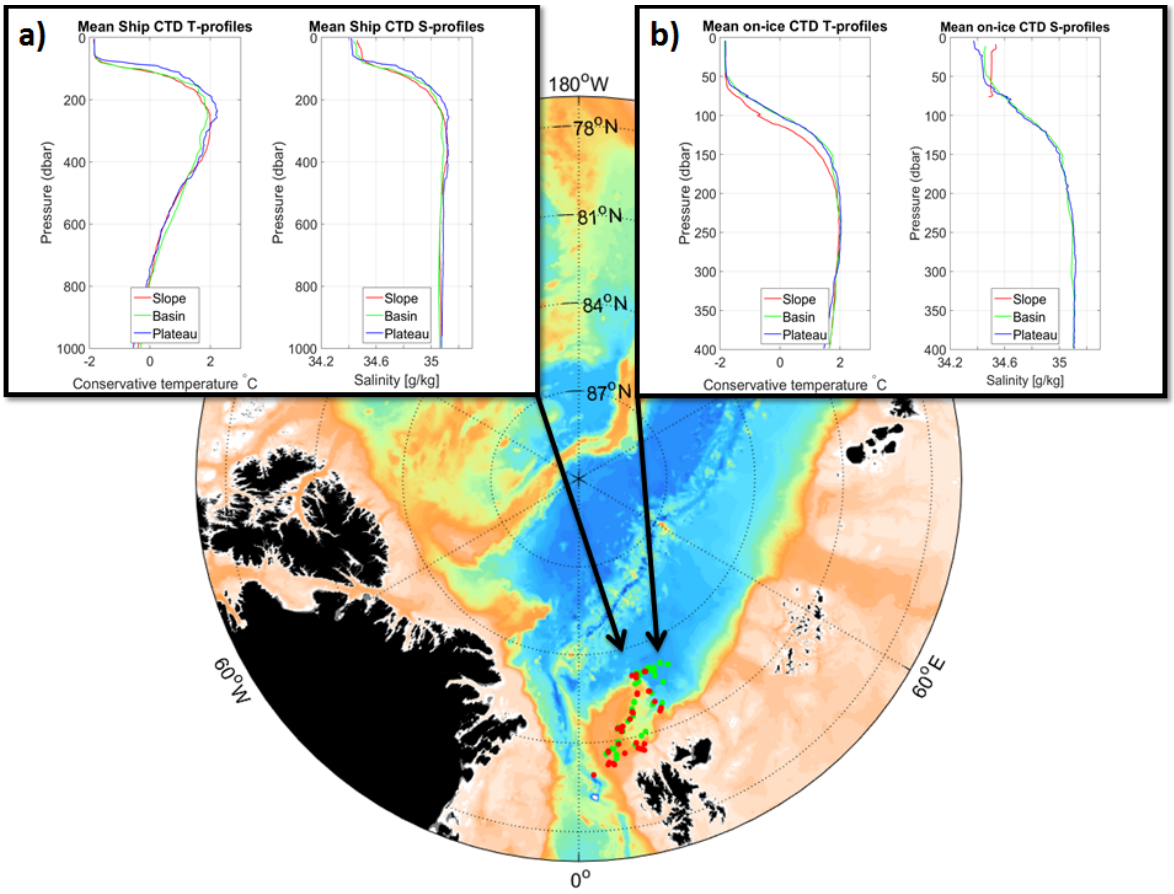

Figure 4.1: Map of the Arctic Ocean showing CTD stations during the N-ICE2015 campaign. Ship CTD stations are marked in red and on-ice CTD stations are marked in green. The color shading shows depth with the 4000 m to 5000 m deep basin as dark blue. Inset a) shows a mean of all ship CTD temperature and salinity profiles from the 3 distinct regions from Jan-June plotted down to a depth of 1000 m. Inset b) shows a mean of all on-ice CTD temperature and salinity profiles for the separate regions from January-June down to a depth of 400 m.

4.3 most measurements from drift 1 and 2 are conducted over the Basin and Slope while drift 3 and 4 are mainly over the Plateau. Besides the warming during drift 3 and 4, particularly warm AW which is also close to the surface can be observed by the end of drift 1 and around May 10th. The interface between the AW and the upper layer is clearly visible as a strong thermocline between approximately 80 m and 150 m depth. The 0 °C isotherm, determining the depth of the AW layer, is shown as a white line (Rudels et al. (2000), $AW > 0$°C, no difference is made between AW and MAW). Lower salinities in the surface layer are found throughout the end of drift 3 and 4 (Fig. 4.3) indicating increased melting in these periods. Due to problems with the salinity sensor on the on-ice CTD during drift 4 there was not sufficient data to plot a proper salinity section for this drift and it is therefore left blank (Chapter 3.4.2).

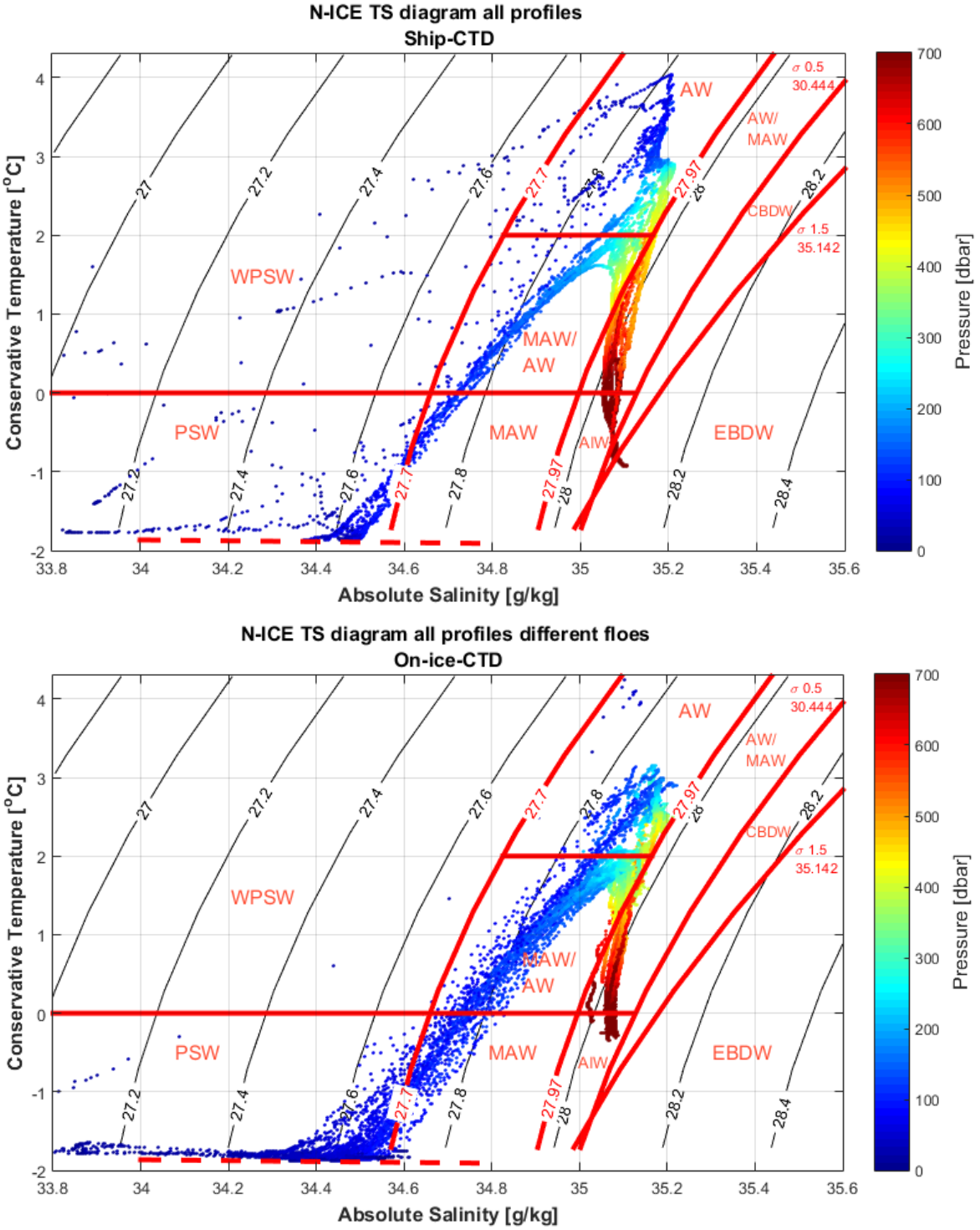

Figure 4.2: T-S diagram from all ship and on-ice CTD profiles. Water masses are defined according to Rudels et al. (2000), and given in Table 2.1 in Chapter 3. The dashed line represents the freezing point. In this study no difference is made between AW and MAW, and AW is defined as $AW > 0°\mathrm{C}, \theta = 27.7 < AW < \theta_{0.5} = 30.444$. *Although measurements go deeper, the colourbar is set to go to 700 m. All deeper values are red. At 1 °C the variance in salinity from the on-ice CTD is ∼ 0.18 g/kg, while the accuracy is 0.09 g/kg. Approximately half the observed variance in salinity from the on-ice CTD may be due to low accuracy. Because the accuracy of the on-ice CTD is very different from the ship CTD, the two T-S diagrams are not merged.*

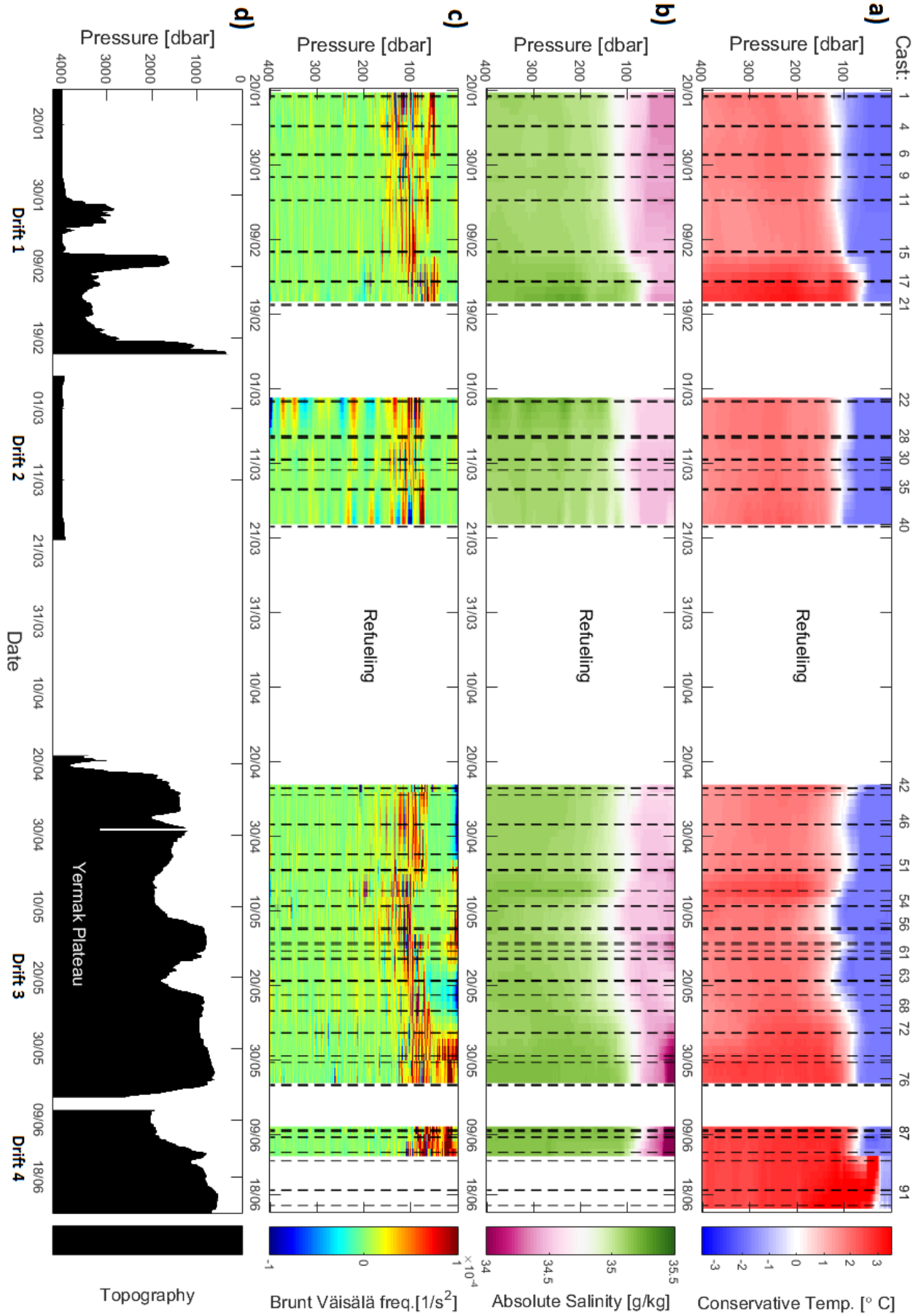

Figure 4.3: Caption next page.

Figure 4.3: (Previous page.) Temporal section from on-ice CTD daily and depth interpolated (upper 400 m). a) Conservative Temperature (colorbar is customised and forced between -3 °C and 3 °C to illustrate the upper limit of the AW with white color), b) Absolute Salinity, c) Brunt Väisälä Frequency, and d) bottom topography from mapped topography at the given locations. CTD cast locations are marked with dashed lines and cast number. The section is divided in 4 different drifts separated by periods of repositioning and refueling. A total of 91 profiles went into making this section, and it was decided not to make a similar section from the ship CTD data because both the temporal and spatial spacing between the different stations were considered too large to make a good and informative section. The total number of ship CTD casts is fewer, and also several were taken with more than one week in between.

Table 4.1: N-ICE2015 hydrography observation characteristics from on-ice and ship CTD combined. Here the spring season is defined from the 25th of May onwards, when melting season begins, as will be discussed in Chapter 5.

	Winter			**Spring**		
	Mean	**Max**	**Min**	**Mean**	**Max**	**Min**
Mixed layer depth	66 m	96 m	5 m	21 m	75 m	3 m
Near surface temp.	-1.83°C	-1.52°C	-1.82°C	-1.19°C	0.81°C	-1.83°C
Near surface sal. [g/kg]	34.38	34.61	34.20	33.71	34.39	32.43
AW layer depth	107 m	136 m	57 m	56 m	89 m	2 m
AW core temp.	2.06°C	3.27°C	1.62°C	3.22°C	4.05°C	2.50°C

Sections of Brunt Väisälä frequencies show the stability of the water column (Fig. 4.3). Frequencies are highest, i.e. the water column is most stable in the interface between the AW and the surface layer. This strong stratification prevents mixing across the interface. The layers above and below are homogeneous and therefore have low buoyancy frequencies. The stratification is highest over the Plateau during drift 3 and 4.

Figure 4.1 and the regional profiles in Figure 4.4 show that regional differences in temperature and salinity properties exist but are small. On the Plateau, the AW is slightly warmer and closer to the surface than in the Basin and on the Slope. Coldest waters are found in the Basin. Also the saltiest waters are found on the Plateau, while in general the Slope has fresher waters than the Basin. There are clearly two regimes in the observations. One period has deeper and colder AW and a deeper saltier mixed layer, when the drift was mostly in deeper waters (Fig. 4.3). A second period has a fresher, shallower mixed layer, and warmer and shallower AW, when the drift was mostly on the Plateau. The fresh and shallow mixed layer is observed during spring. Whether the observed changes are seasonal or regional is discussed in Chapter 5. The warmest profiles are observed by the end of drift four and three when the ship was furthest to the South and closest to the AW inflow in the Fram Strait.

Near surface temperature is defined as the uppermost good temperature measurement from the on-ice CTD after despiking, this is usually just below the ice bottom, where the CTD comes through the hole, i.e. approximately at 3 m depth. Figure 4.5

shows the departure from freezing point in the surface layer. When melting season starts, heat is mixed upwards and solar radiation is absorbed.

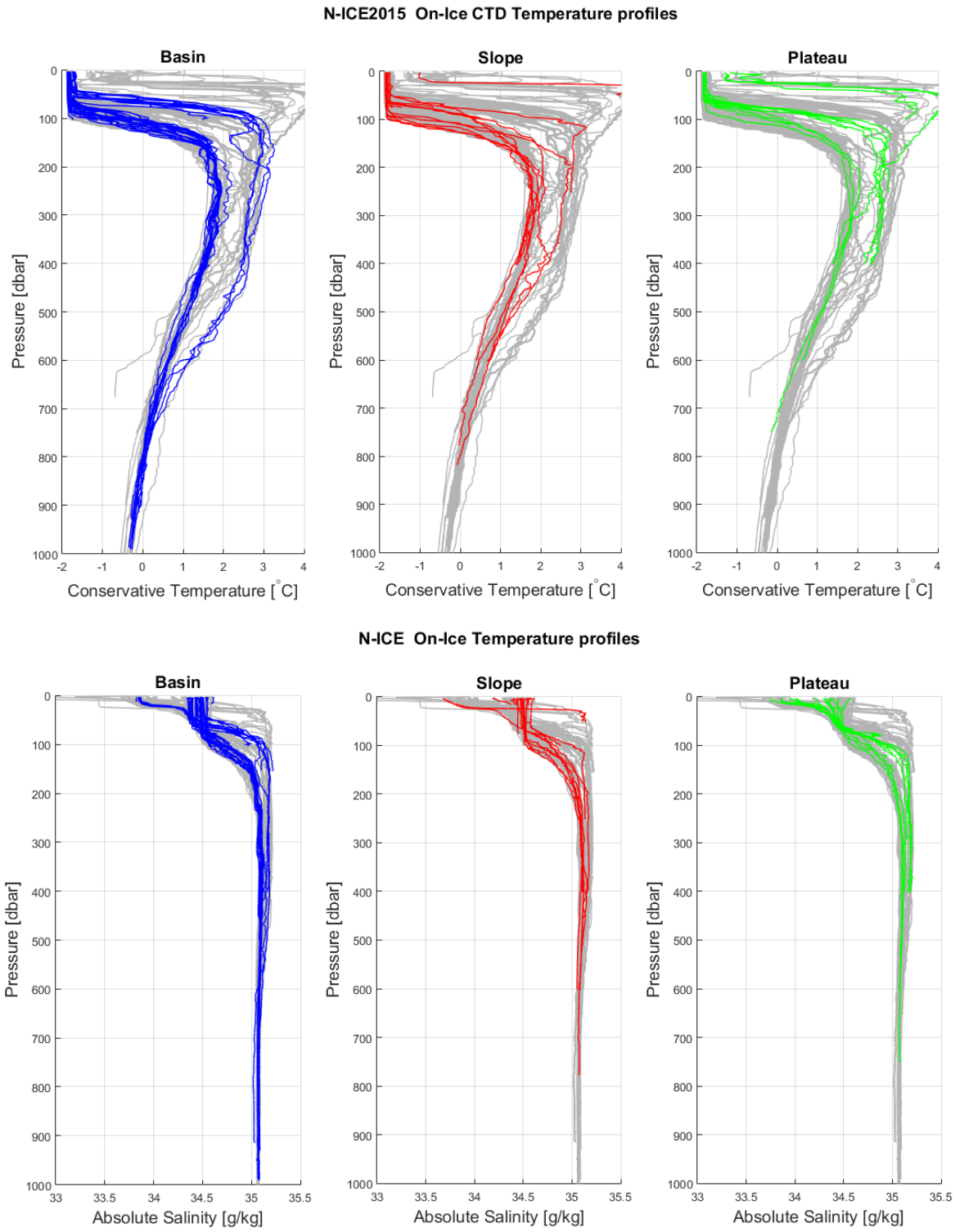

Figure 4.4: Regional temperature and salinity profiles from on-ice CTD. The colours indicate profiles in the Basin (blue), on the Slope (red), and on the Plateau (green). In light gray all profiles for all regions from both the ship and on-ice CTD together are shown for comparison.

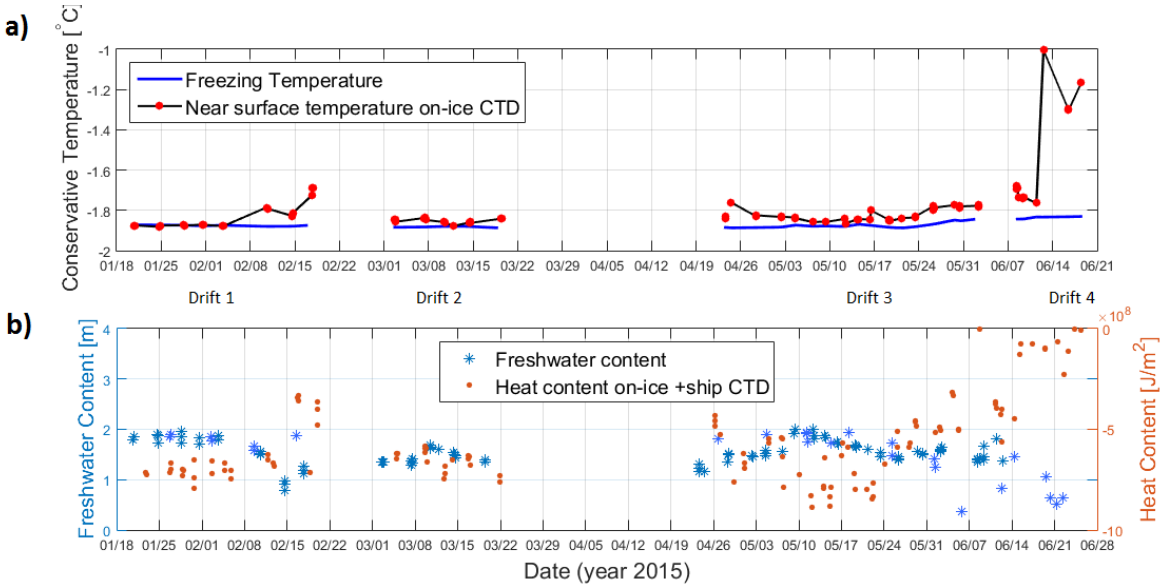

Figure 4.5: a) Near surface temperature development (red dots) and freezing temperature (blue) based on observed salinity. b) Heat content (orange) in the whole upper layer above the AW layer relative to reference temperature of 0°C *and total freshwater content (blue) in the whole upper layer lying above the reference salinity of 35 g/kg (not normalised).*

4.2 Atlantic Water and upper layer characteristics

Different characteristics of the AW and upper layer have been studied; the depth of the uppermost AW, the mixed layer depth and the AW core temperature.

4.2.1 Atlantic Water and mixed layer depth

The depth of the AW layer is shown as the depth of the uppermost zero-degree isotherm (Chapter 2). A time series of this is shown from the combined on-ice and ship CTD data set (Fig. 4.6 a). The mixed layer depth (MLD) is calculated according to the density criteria described in Chapter 3 and is shown in Figure 4.6 b). Both are relatively stable during drift 1 and 2 except from one event where both the AW layer and the surface mixed layer become 30-40 m shallower. This occurred when the ship drifted over the Slope and onto the Plateau. During mid-May, a higher MLD is found over the Plateau. However, no change is seen in the AW layer at that time. The AW layer is closer to the surface (20-30 m) and the MLD thins when melting starts on the 25th May (second half of drift 3). Mean observed AW depth and MLD are given in Table 4.1. The shallowest observed AW is at 5 m in mid-June. Spatial distribution of AW and MLD depths is shown in Figure 4.8, indicating that the shallowest AW and mixed layer are found on the southern part of the Plateau. However, these are also the latest measurements in spring. Taking this into account, deeper AW and mixed layer are generally found in the Basin compared to the Slope and Plateau. The AW depth was compared to changes in topography (not shown), and a correlation of -0.43 was found (18 % of the variance may be explained by topography change). The AW depth has also been compared with

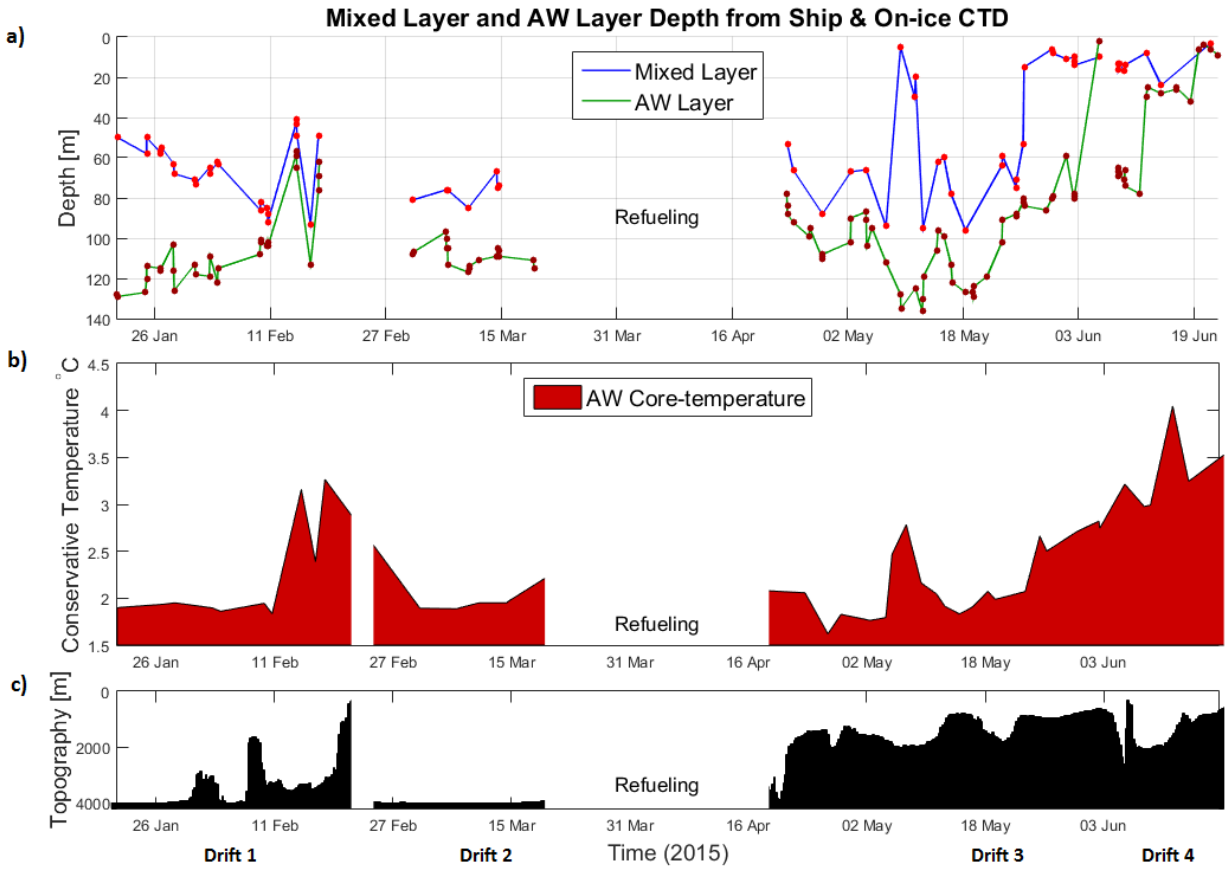

Figure 4.6: a) Timeseries of mixed layer dept and AW layer depth from combined ship and on-ice CTD data. b) Timeseries of AW-core temperature from combined ship and on-ice CTD data. c) Bottom topography from maps.

distance from AW inflow in the Fram Strait (Fig. 4.9). Generally the AW sinks along the inflow path and the correlation found is 0.55 (30 % of the variance explained).

4.2.2 Atlantic Water temperature

The AW core temperature is defined as the highest temperature measured in the AW layer (Chapter 3), which is found at intermediate depths between 100 m and 300 m (Fig. 4.1), and is used as an indicator for the temperature in the whole layer. Measured AW core temperature from the on-ice and ship CTD combined is shown in Figure 4.6 b). Maximum core temperature is observed in spring (4.05 °C) and the minimum in winter (1.62 °C). The mean temperature is 2.36 °C. The core temperature was analysed against topography (not shown) and correlated with 0.43 (18 % of the variance). The AW core temperature was also compared with distance from AW inflow in the Fram Strait (Fig. 4.9), resulting in a correlation of 0.63 (40 % of the variance explained). The AW core temperature has been measured at the southern tip of Svalbard as it flows towards the N-ICE2015 region through the Fram Strait. A time series from 1978 to 2014 of repeated August measurements at this location is shown in Figure 4.7. This figure shows evidence of 5-10 year long cycles, as mentioned in Chapter 2, but also an

increasing trend of 0.03 °C / year.

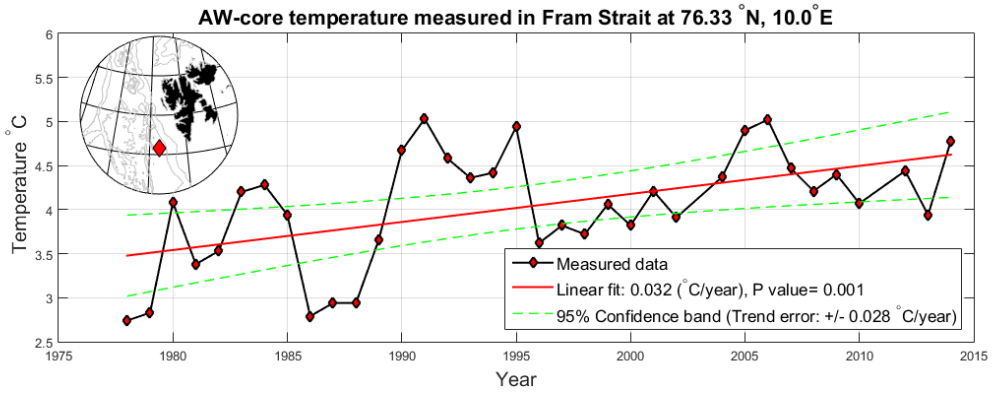

Figure 4.7: Timeseries of AW-core temperature (black) measured in the Fram Strait. Data from the Norwegian Institute of Marine Research. A linear fit shows an increasing trend of 0.032 °C/year (red line). Green lines show the 95 % confidence band for the linear fit. The trend error is calculated relative to the 95 % confidence band.

4.2.3 Freshwater and heat content

Freshwater and heat content are calculated for different layers as described in Chapter 3. Heat content for the upper layer is integrated down to a depth of 200 m, stopping when the temperature increases above 0 °C. The physical interpretation is that this heat has been removed from the water after it seized being AW. Figure 4.5 shows that the heat content in this upper layer is nearly constant around $-7 \cdot 10^8$ J/m^2 but that it rises slightly in mid-February and increases with half an order of magnitude in June. Freshwater content is also integrated down to a depth of 200 m, stopping when the reference salinity of 35.4 g/kg is reached. This gives the total amount of freshwater above the reference salinity. The freshwater content in the whole upper layer varies between 1 and 2 m without dominant changes. Freshwater content is also calculated for a thin fixed near surface layer of 20 m (not shown), and this reveals a strong freshening of the near surface layer for late May and June.

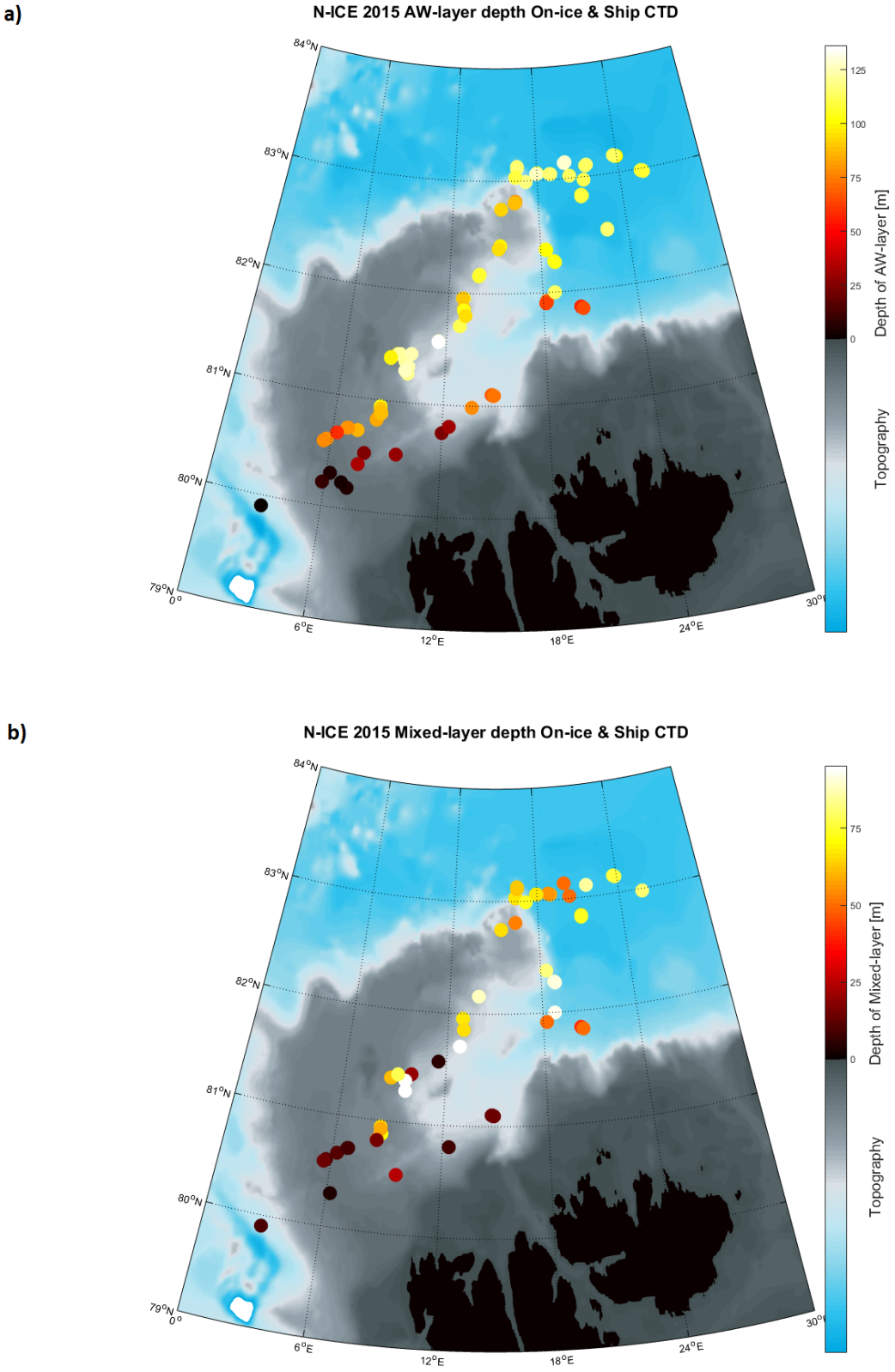

Figure 4.8: Water depths from N-ICE2015 observations. Spatial variation of a) AW layer and b) mixed layer depth from combined ship and on-ice CTD. Colour shading shows the water depth ranging from 0 m (grey) to 5000 m (blue).

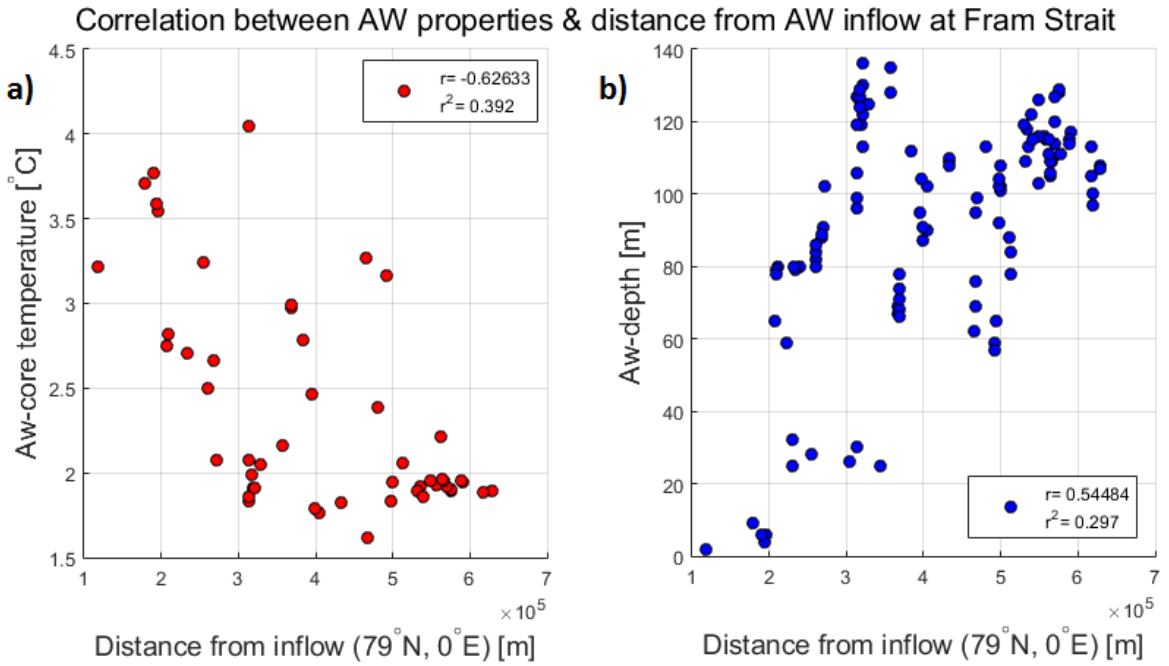

Figure 4.9: AW core temperature (a), and depth (b) compared with the distance from the AW inflow in the Fram Strait (which is set to an approximate location at 79 °N and 0 °E) at location of the measurements.

4.3 Historical data

4.3.1 Long term trends

Temperature and salinity properties from two gridded climatologies, the Polar science center Hydrographic Climatology (PHC3.0) and the World Ocean Atlas 2013 (WOA), have been compared with N-ICE2015 observational data. Comparison is also performed towards observed profiles in our area from the World Ocean Atlas, hereafter referred to as "REALWOA". Seasonal definitions vary for the different climatologies (Fig. 3.6). Most data collected in the region is from summer, however the N-ICE2015 cruise can be classified as mostly winter, and partly as spring (from 25th May). Climatological data for comparison during spring is sparse and therefore chosen to only present winter and summer data in this study. Comparisons are made in Figure 4.10 and 4.11. One particularity is that no mixed layer can be identified for neither of the climatologies nor from REALWOA, while it is evident for the N-ICE2015 winter observations. The same water masses can be seen in all climatologies and observations. The depth information from the REALWOA is very rough and with larger differences than the others. This gives a strange looking and stuttering profile with especially strange values near the surface.

At depth climatologies agree, confirming that the data is comparable. At intermediate depths in the AW layer they differ greatly, especially during winter (Fig. 4.10). Summer observations from the PHC3.0 and WOA of both temperature and salinity are comparable, but from winter there is a large difference, especially in temperature.

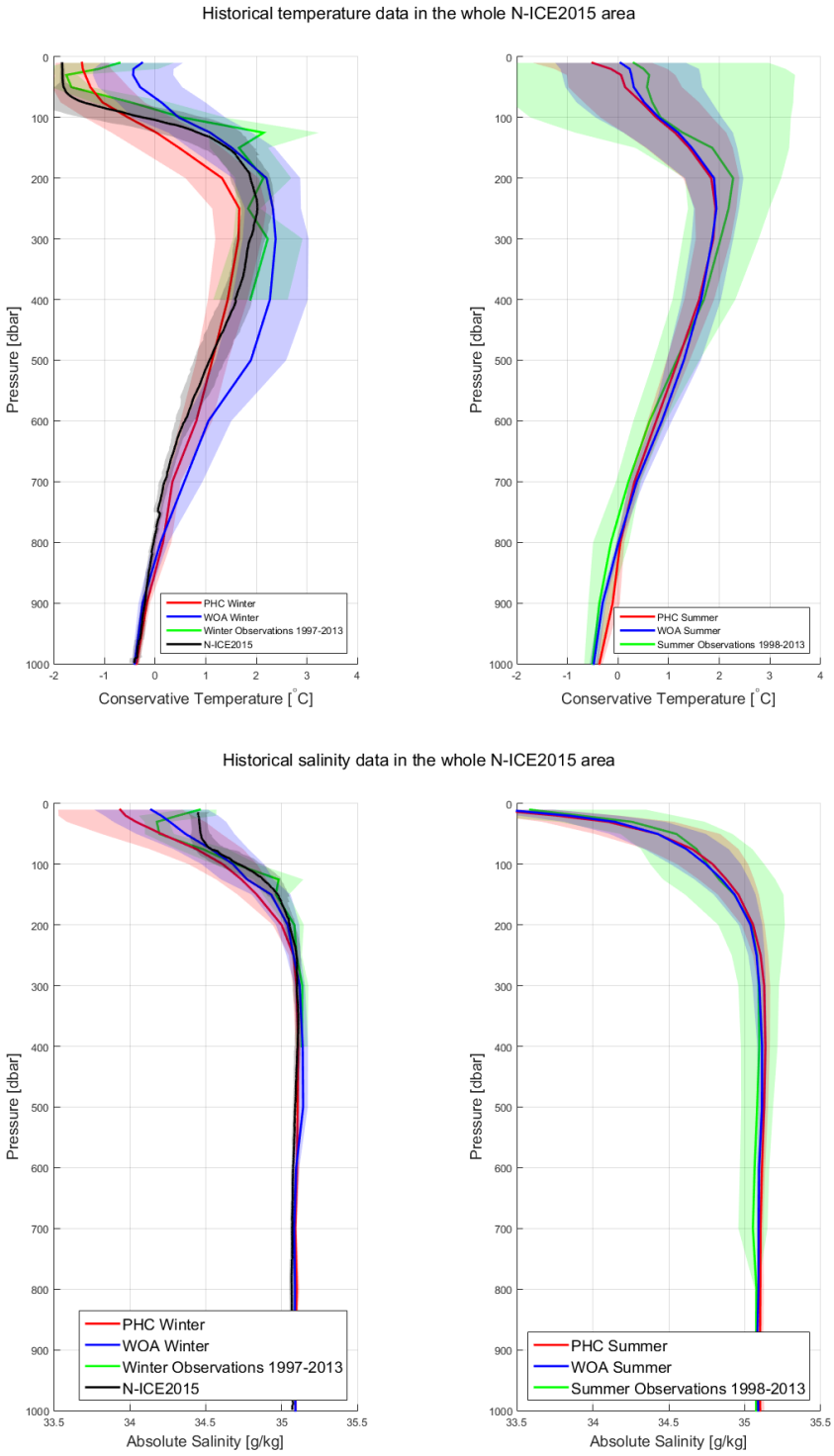

Figure 4.10: Historical mean temperature and salinity profiles from the two climatologies (PHC3.0 and WOA) compared with N-ICE2015 observations and observations from the World Ocean Atlas (REALWOA) in the period 1998-2013. Profiles are regional means from one degree cells for the whole region defined as the "N-ICE2015 area". Standard deviation is shaded in colours. Details about data and seasonal definitions are given in Chapter 3.

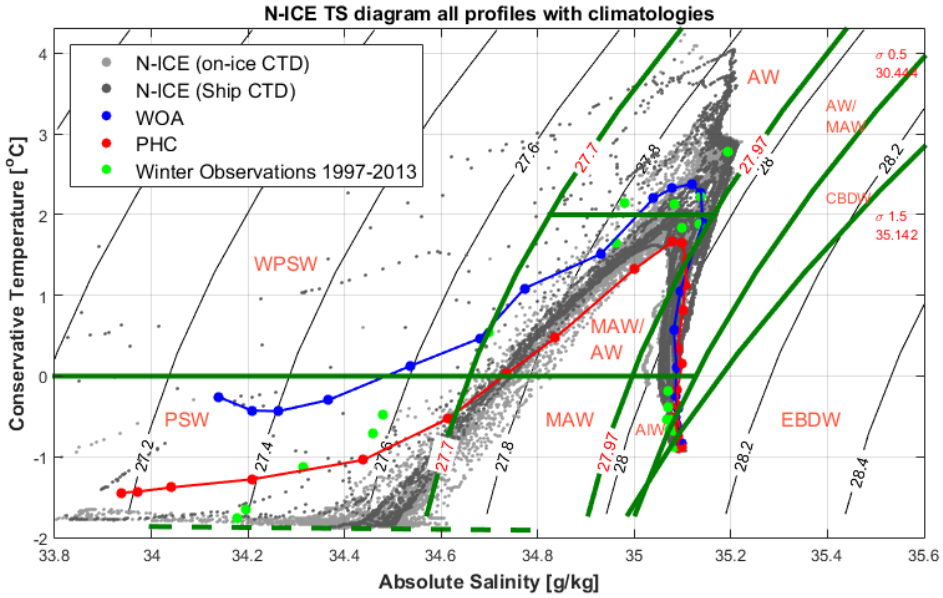

Figure 4.11: Historical mean T-S diagrams from the two climatologies (PHC3.0 and WOA) compared with N-ICE2015 observations and observations from the World Ocean Atlas (REALWOA) in the period 1998-2013. Details about data and seasonal definitions are given in Chapter 3. N-ICE2015 observations are divided for ship and on-ice CTD. Water masses are boxed according to the definitions from Rudels et al. (2000) and AW defined as $> 0°C, \theta = 27.7 < AW < \theta_{0.5} = 30.444$. *The dashed line represents the freezing temperature.*

PHC3.0 is coldest with almost 1 °C difference in AW core temperature compared to WOA, which is warmest. N-ICE2015 observations fall approximately in between. REALWOA observations are warmest during summer but slightly colder than WOA during winter, although it has large standard deviations. From PHC3.0 to N-ICE2015, a warming is observed. But from WOA to N-ICE2015, no warming is observed. In temperature there is no large difference between REALWOA and N-ICE2015.

The AW layer is deep in the PHC3.0, shallower in the WOA and again slightly deeper in REALWOA and during N-ICE2015.

Surface salinities vary a lot. PHC3.0 shows freshest surface values, WOA slightly saltier, while REALWOA and N-ICE2015 have the salties surface values. At depth, on the other hand, PHC3.0 and WOA are slightly saltier than REALWOA and N-ICE2015.

Measurements from the Fram expedition in 1893-95 show colder AW with almost 2 °C difference compared to the N-ICE2015 measurements (4.12). The AW layer also appears to be deeper. From approximately 200 m depth and down, all measurements from the Fram expedition are saltier than those from the N-ICE2015 campaign, with approximately 0.4 g/kg difference. These measurements where mostly taken in the Laptev Sea, the Kara Sea, the Barents Sea, and the eastern Eurasian Basin These observations only overlap with the N-ICE2015 area for a small part, but are still interesting for comparison. The spatial change in AW-core temperature must be taken into account here, and will be discussed related to Figure 4.26.

Temperature and salinity profiles taken during the Nautilus expedition north of the

Fram Strait in 1931 are comparable and similar to those from N-ICE2015, and are also taken in the same region.

4.3.2 Seasonal variability

Seasonal variations of T-S properties in the N-ICE2015 area are large (Fig. 4.10). Temperatures at the surface and at shallow depth for the climatologies are around 0 °C in summer and around 1 °C in winter (Fig. 4.10). AW core temperatures in summer from both PHC3.0 and WOA are approximately 2 °C which is similar to the N-ICE2015 winter observations. Temperature profiles from WOA show surprisingly that the AW core temperature is 0.4 °C higher in winter than in summer (Fig. 4.10). PHC3.0 shows warmer AW temperatures during summer than during winter and so does REALWOA.

From the salinity profiles of WOA, PHC3.0 and REALWOA we observe a freshening of the surface layers during summer, but also increased stratification and higher salinities at intermediate depths between 40 m and 100 m. At AW depth, the difference between PHC3.0 and WOA temperature profiles is smaller in summer than in winter. The winter AW temperature from N-ICE2015 is similar to the winter AW temperature from the climatologies.

4.3.3 Spatial variability

Spatial differences in the climatologies and observations have been analysed in reference to the three regions the N-ICE2015 area is divided into; Basin, Slope and Plateau (Fig. 4.13). In general the differences between the three different regions are small, and deep values are consistent for all regions. The main relative difference in temperature between climatologies remains similar to the whole region: from the PHC3.0 climatology there is a general warming onwards to WOA13. The difference between climatology and observations is largest for the Slope where PHC3.0 shows AW core temperatures of 2.4°C, WOA shows 3.0°C and N-ICE2015 observations show a maximum of 2.0°C. Here the N-ICE2015 observations are colder than all historical observations. On the Plateau, the difference is smaller and PHC3.0 is coldest, WOA the warmest. Here N-ICE2015 observations lie in between the climatologies. Below 450 m on the Plateau, our observations are colder than both PHC3.0 and WOA. In the Basin, mean N-ICE2015 observations are warmer than both PHC3.0 and WOA with a mean core-temperature of approximately 2 °C. Warmest AW is found on the Slope for the climatologies, followed by the Plateau and then the Basin. For N-ICE2015 observations, warmest AW spatially is found on the Plateau followed by the Basin and then the Slope.

Regional differences in salinity are minimal, except for surface salinities as can be seen from Figure 4.13. Also here, no mixed layer can be identified in the climatological mean profiles. A small mixed layer can be seen from temperature values in the Basin PHC3.0 profile, but salinity is stratified. Spatial comparison for summer mean profiles has also been done (not shown). The same development as discussed for the whole region is seen, and the relative differences between the different regions are the same as for winter.

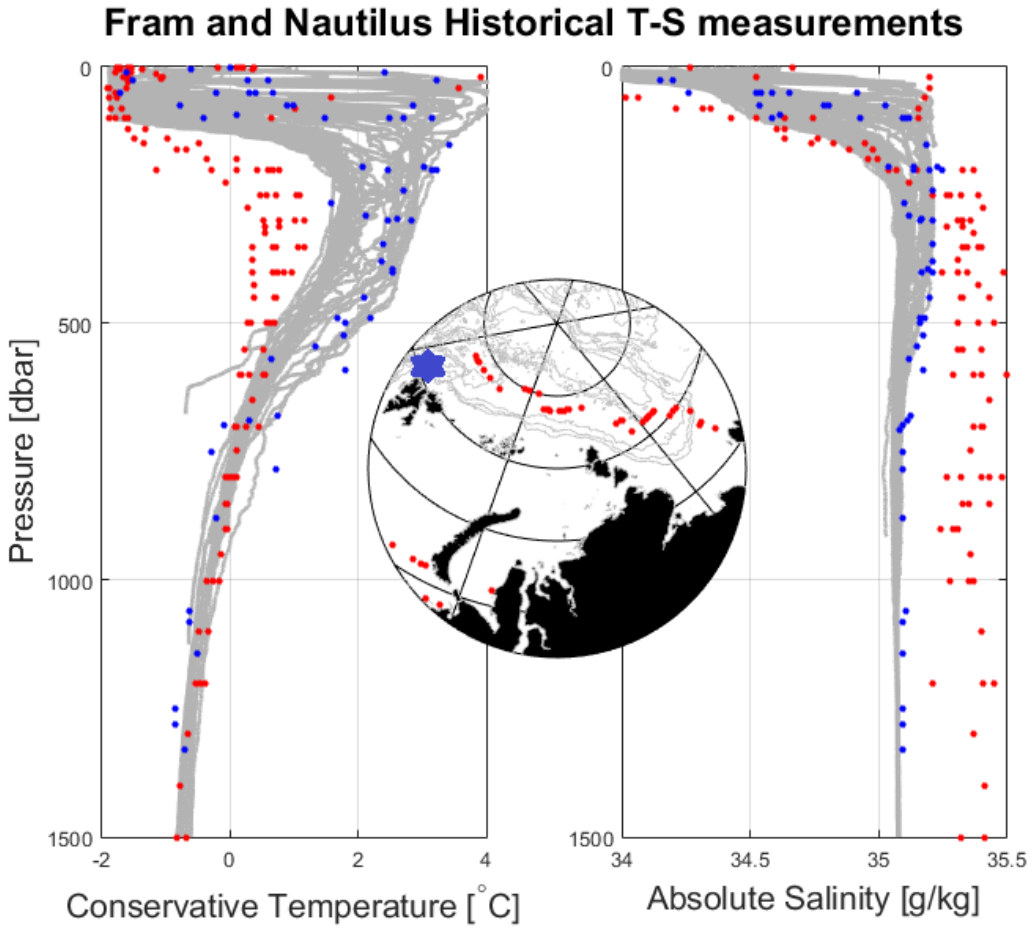

Figure 4.12: Historical observations from the Fram 1893-95 expedition (red dots) and Sverdrup's measurements from the Nautilus 1931 expedition (blue dots) in the Eastern Arctic Ocean. All ship and on-ice CTD data from N-ICE2015 is shaded in the background. Temperature and salinity values from the historical data sets are converted to conservative temperature and absolute salinity. Locations of the Fram CTD stations are marked on the map while locations of the Nautilus stations are not reported in the dataset. Most Nautilus stations come from the Nansen Basin north of Svalbard (blue star). Salinity measurements from the Fram expedition have high salinities (higher than would be expected in the ocean in general). We do not know the quality of these data, and do not know whether there is an error in the data.

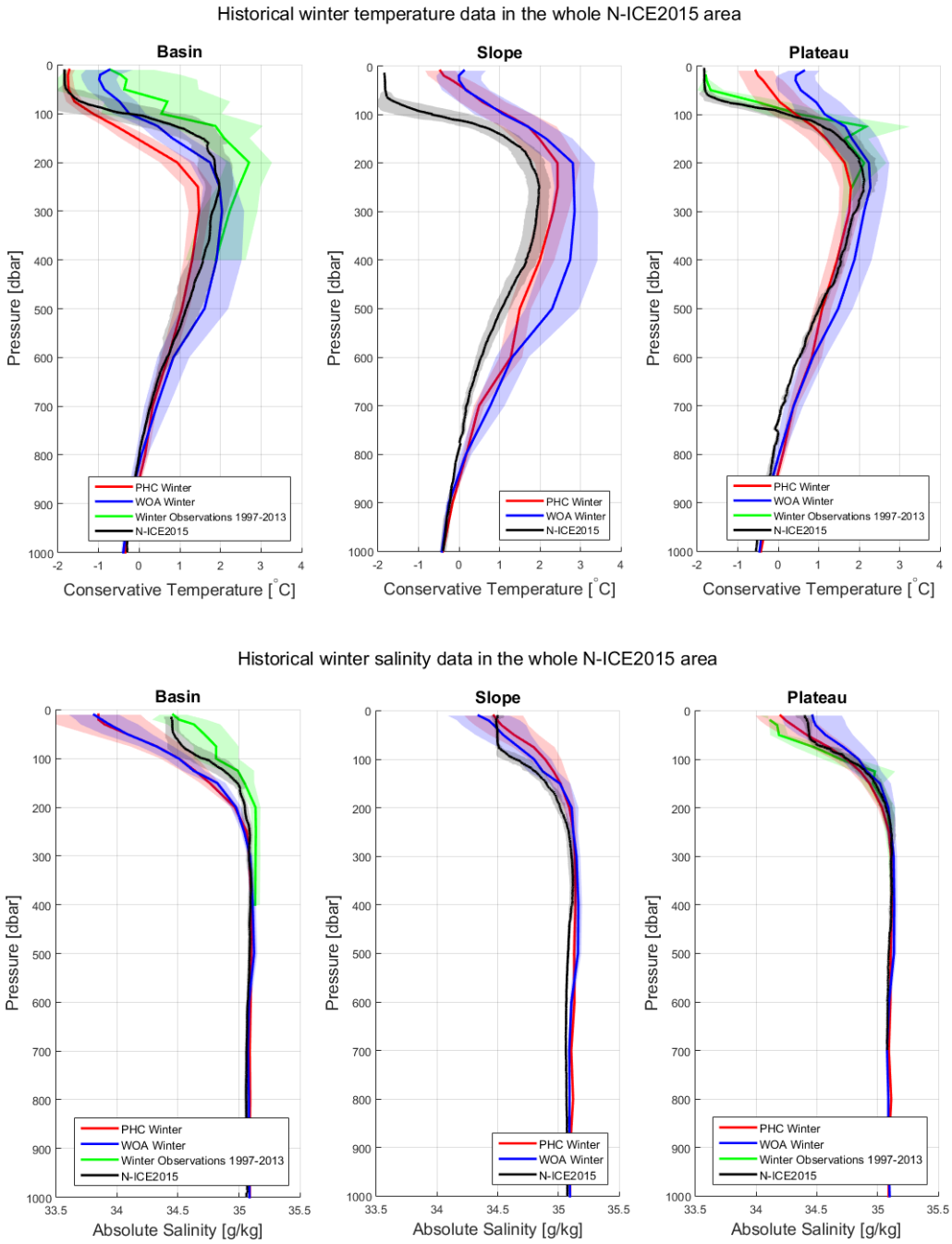

Figure 4.13: Historical mean temperature and salinity profiles from the two climatologies (PHC3.0 and WOA) compared with N-ICE2015 observations and observations from the World Ocean Atlas (REALWOA) in the period 1998-2013. Profiles are regional means from one degree cells for the three different regions defined as Basin, Slope and Plateau. Standard deviation is shaded in colours. Details about data and seasonal definitions are given in Chapter 3. No winter observations from REALWOA exist for the Slope region.

4.4 Currents

Current velocity measurements have been performed down to a depth of approximately 500 m by the Long Ranger ADCP. Observations from the Long Ranger ADCP have been compared to simulations of the barotropic current velocity field from the NorESM climate model. Measurements from the Long Ranger ADCP were available in 8 m bins and were sorted in layers (mixed layer and AW). The velocity profiles are nearly barotropic, i.e. the current velocity and direction vary little with depth. The mean current velocity is small (mean ~ 0.1 m/s). In general the AW and the surface mixed layer follow each other.

Simulations of the barotropic vertically averaged current from NorESM (Fig. 4.14) show inflowing AW west of Svalbard that divides into two branches. North of Svalbard one branch flows eastward directly across the Yermak Plateau (Svalbard branch). The other branch bends westward, where some of the AW recirculates back into the East Greenland Current and southwards to the Atlantic Ocean. An outer branch of AW is believed to follow the Yermak Plateau on the western side and around the Plateau (Yermak Branch, purple arrow in Figure 4.14, (Ivanov et al., 2009)), but this is not simulated by NorESM. Some of the water from the Svalbard branch is simulated to circumnavigate the Plateau anticlockwise and recirculate back with the southward flowing waters from the North. We believe that the southward flow around 0 °E is part of the southward flowing East Greenland Current, although it was simulated far to the East. It is important to remember that the simulation shows a vertical barotropic average, and that it may not capture an AW core, or a mixed layer with different direction and strength.

Figure 4.15 shows a map with a vector plot of the 24-hour vertical mean observed velocity during drift 3. The motion direction varies widely as the Long Ranger drifts over the Yermak Plateau, however a south-westerly mean direction is observed. Observations from the Long Ranger ADCP are similar to what is simulated by NorESM. Both show a mean south-westerly flow on the Yermak Plateau. In the upper 500 m, the current direction appears little affected by topography (Fig. 4.16). The mean flow, however, still appears to slightly follow topography (Fig. 4.16).

Figures 4.17 and 4.18 show Long Ranger velocity observations during drift 3 and 4 over the Yermak Plateau combined with wind observations, tidal analyses and calculations from the Turbulent Instrument Cluster (TIC). Both current direction and absolute velocity throughout the whole depth fluctuate with a diurnal frequency that is closely synchronised with the predicted tidal frequency. The current has a mean south-westerly flow, but changes 180° direction four times a day. The current direction follows the predicted tidal direction, although the observed vertical mean absolute velocity is nearly double that of the simulated tidal velocity. A tidal spring-neap signal is present in both model and observations, but the diurnal signal in the observations is much stronger than what the tidal model predicted. In a diurnal cycle, the mean observed velocity fluctuates over a range of 0.1 m/s, while the tidal model only predicts a fluctuation over a range of approximately 0.02 m/s relative to the ground (Fig. 4.18).

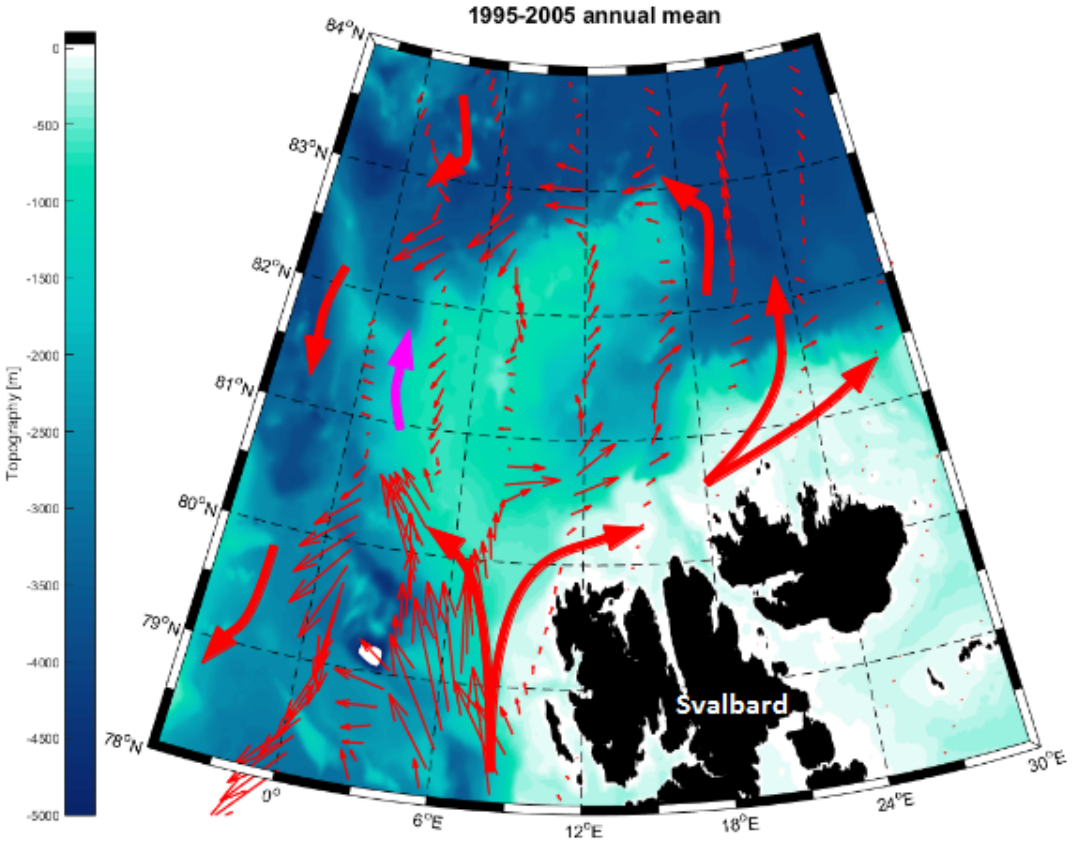

Figure 4.14: Map of the N-ICE2015 area showing a vertical mean of the barotropic current velocity for each grid cell simulated by the NorESM climate model, and averaged over the years 1995 to 2005. A volume weighted vertical average is performed over the different isopycnal levels of the model. Arrows denote current direction and relative strength. Thick red arrows show the main circulation pattern that is observed from visual inspection around the Yermak Plateau from the simulations. The thick purple arrow shows the location and direction of a suggested AW outer branch (Yermak branch, Ivanov et al. (2009)). Overlying topography in colors scale ranges to 5000 m.

Absolute current velocity appears little affected when the ship drifts over regions with different (shallower, deeper or steeper) topography, but in our observations these topography changes are also quite small, as most measurements are taken over the Plateau (Fig. 4.18 b). In particular, three large wind events, or minor storms, occur in our time series during the end of May and mid June. These events are clearly observed in the Long Ranger observations. The drift speed of the ship/ice varies between 0.1 m/s and 0.4 m/s and correlates highly with the wind speed (r=0.71 and r^2=0.50). As a direct result of this, the horizontal ice-ocean shear (defined as the difference between the velocity of the ice and the ocean velocity from the upper-most Long Ranger bin (center at 17 m)) is also largely dependent on the wind speed (r=0.64 and r^2=0.41). Due to the high drift speed and low current velocities, the horizontal ice-ocean shear is large with a mean of approximately 0.15 m/s and maximum values reaching up to

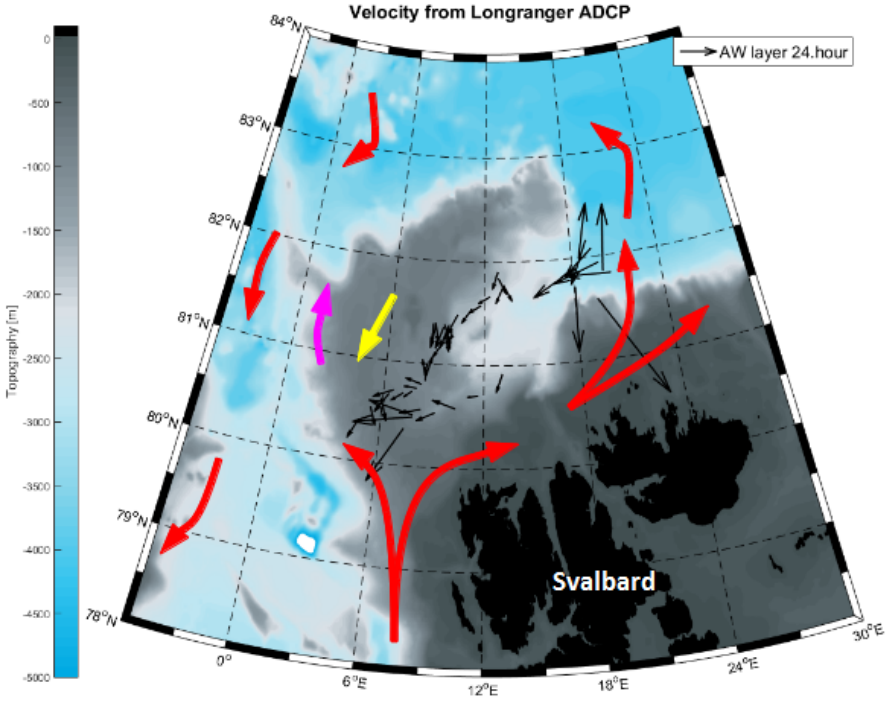

Figure 4.15: Map showing a vertical mean (∼ 17 m - ∼500 m) of the horizontal current velocity during drift 3 from the Long Ranger ADCP (black arrows). Thick red arrows denote the mean barotropic current pattern as simulated by NorESM in Figure 4.14. The thick yellow arrow denotes the mean direction of flow on the Yermak Plateau as simulated by NorESM. The thick purple arrow shows the location and direction of a suggested AW outer branch (Yermak branch, Ivanov et al. (2009)). Overlying topography in colors scale ranges to 5000 m.

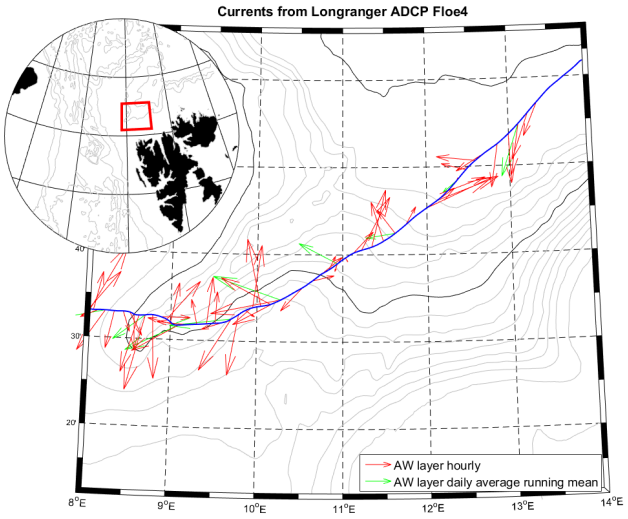

Figure 4.16: Zoom in of a across Slope section during drift 4 with red arrows showing hourly vertical mean AW absolute current velocity and direction from Long Ranger data. Green arrows show a running mean with a 24 hour window of the same AW absolute current velocity and direction.

0.4 m/s. The calculated shear and the shear measured directly from the Long Ranger agree well, although the fluctuations in the calculated values are stronger (Fig. 4.18 a). Measurements close to the center of the ice, to provide a good approximation of the vertical shear, do not exist.

Calculated friction velocity from the TIC measurements directly under the ice is generally below 0.005 m/s, but increases following increased shear and wind (Fig. 4.18 c). Vertical heat fluxes measured under the ice usually remain around 2-3 W/m^2, although they also seem affected by the wind forcing (not shown in graph due to scale) (Fig. 4.18 c). After the small storm on the 22nd of May, the heat fluxes rise to 12 W/m^2 and decrease again to 2-3 W/m^2 around the 24th of May. They rise again to the same level between the 25th and the 29th of May. The heat fluxes increase with several orders of magnitude during drift 4 in June when AW comes closer to the surface. At this point, heat fluxes reach a maximum of 400 W/m^2.

To study the effect of topography, three particular regions of interest have been chosen for investigation; two sections where the drift track is across Slope, from deeper to shallower waters, with large topography change, and one section along Slope with little change in water depth, but along the eastern Slope of the Yermak Plateau (Fig. 4.19, 4.20, 4.21). For all three sections, the flow is nearly barotropic, i.e. almost constant in direction and strength with depth. For both sections across Slope the current direction appears little affected by topography, but it is mostly in across Slope direction. In the longer section along Slope the flow is mostly following the Slope direction, but also changes direction on diurnal basis. The south-western flow is strongest in all three sections. The clearest diurnal tidal signal can be seen in the observations of the first across section and the along Slope section. Here the tidal model (AOTIM5) also predicts a signal of similar frequency, but it is slightly shifted and about 20 % of the amplitude of the observations. The second across section has relatively high current velocities as single events, not following the tidal diurnal frequencies, but higher wind speed. For all sections, the amplitude of the predicted tidal velocity is low, around 0.02 m/s. For the whole Long Ranger time series, the predicted velocities, u and v, correlate moderately with the observed vertical mean u and v velocities (u: r=0.57 and r^2=0.33, v: r=0.56 and r^2=0.31). The absolute vertical mean velocity does not correlate much with the predicted absolute tidal velocity (r=0.34 and r^2=0.12).

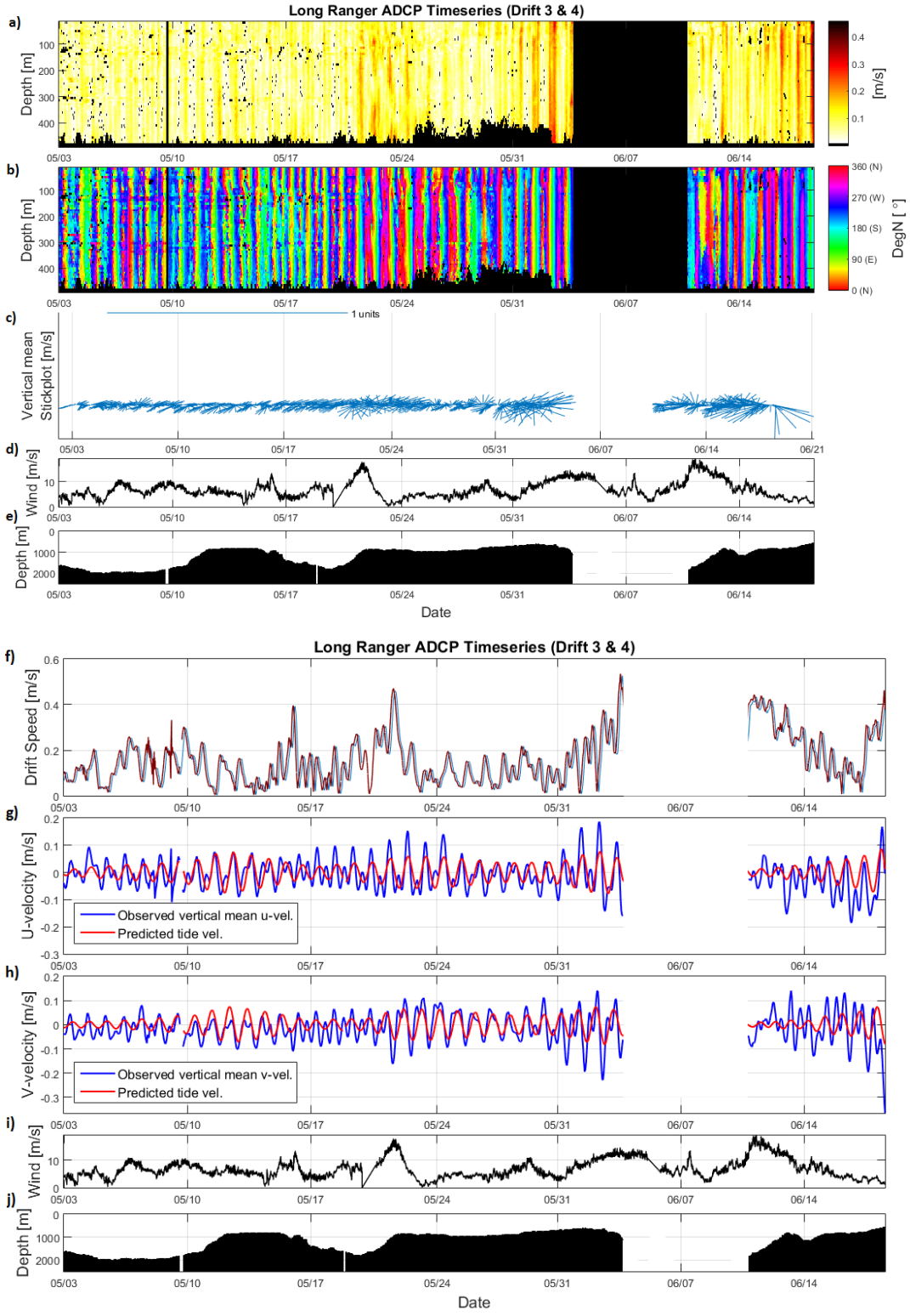

Figure 4.17: Timeseries of Long Ranger ADCP drift 3 and 4. Panel a) showing absolute current strength, b) absolute current direction c) stickplot of vertical mean current, d and i) absolute wind speed, e and j) bottom topography from maps, f) driftspeed, g and h) u and v vertical mean velocity with predicted tides from AOTIM5.

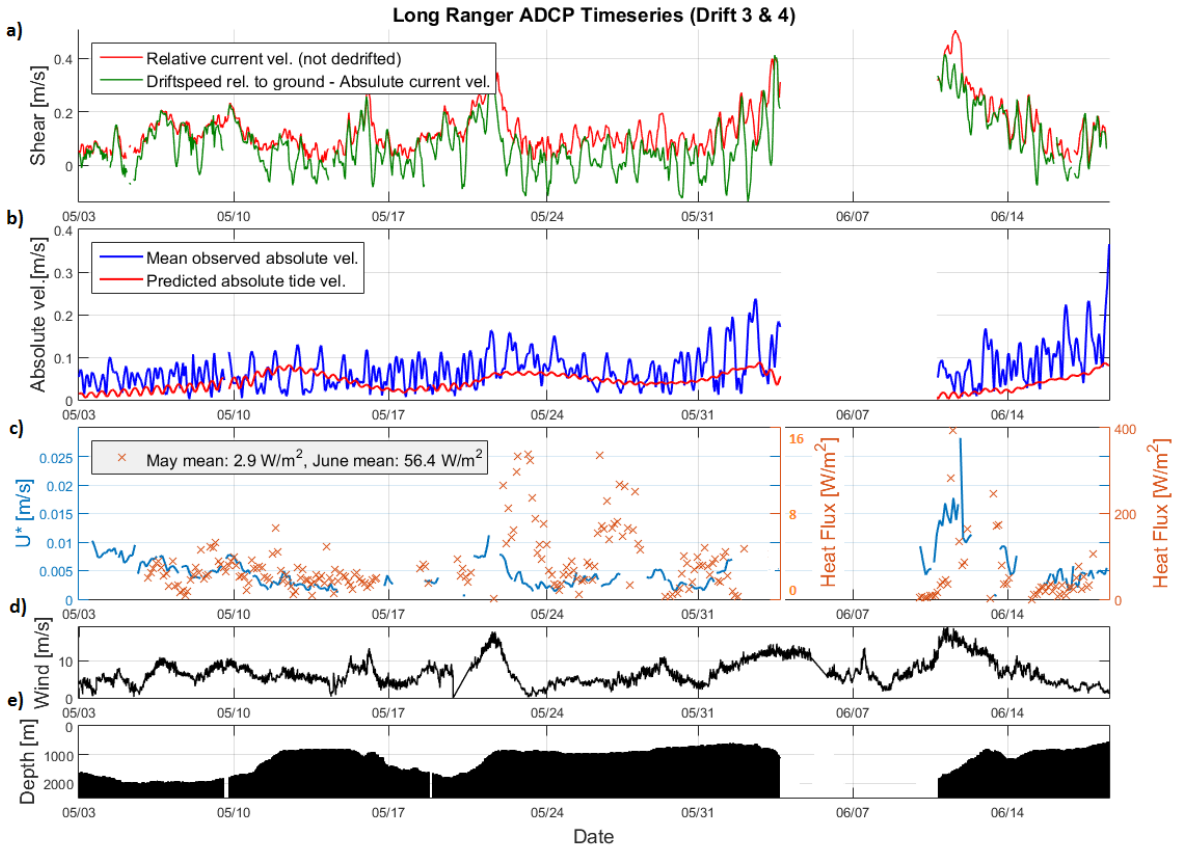

Figure 4.18: Timeseries of Long Ranger ADCP drift 3 and 4. Panel a) the horizontal ice-ocean shear (defined as the difference between the ice velocity and the ocean velocity in the uppermost bin of the Long Ranger (17m)), b) vertical mean absolute current strength with predicted tides from AOTIM5 c) friction velocity, u, and heat flux (Note the different scales on drift three and four) from TIC, d) absolute wind speed, e) bottom topography from maps.*

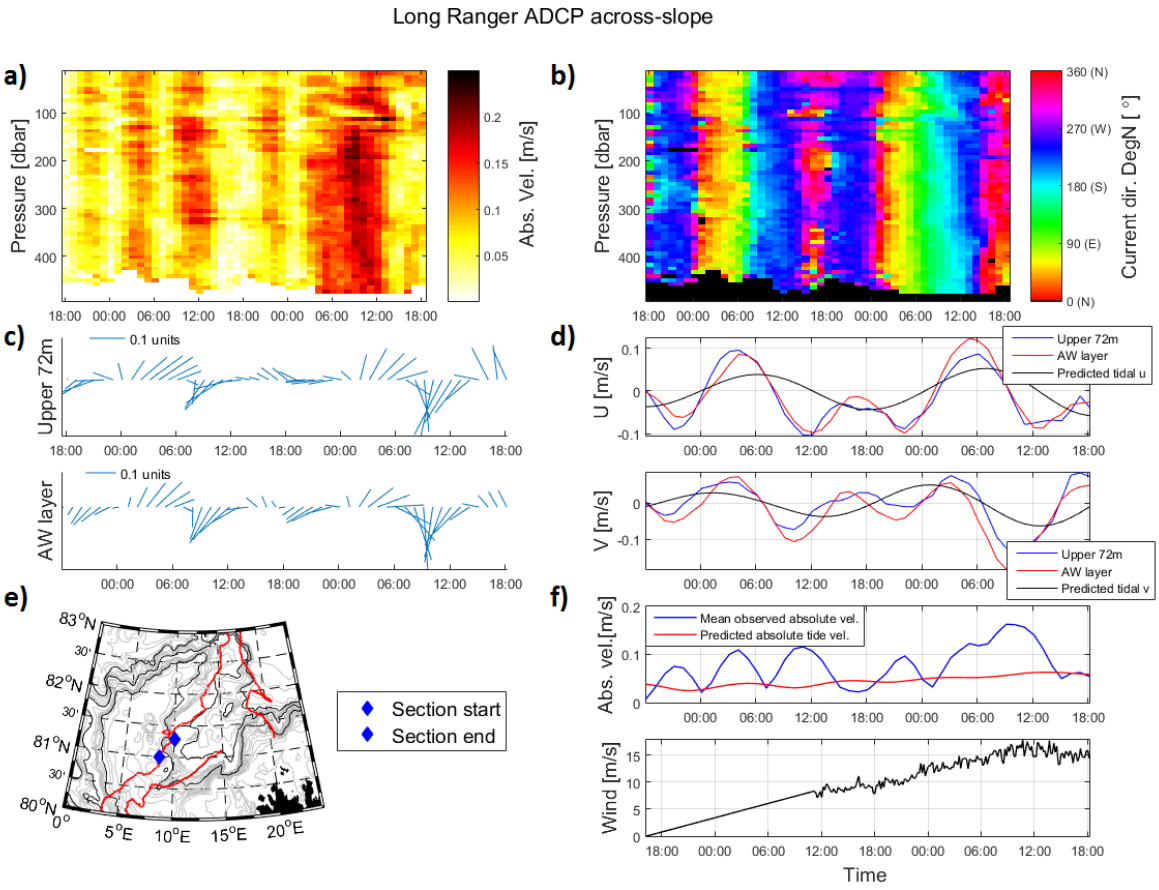

Figure 4.19: Zoom in on across Slope section showing Long Ranger current velocity data during drift 3. a) absolute current strength, b) current direction, c) stickplot showing strength and direction of the current in the mixed layer (above 72 m) and AW layer (below 112 m), d) u and v in the mixed layer and AW layer, e) map showing the location of the section, and f) vertically averaged absolute current strength compared with predicted tidal velocity from AOTIM5 and wind speed. Wind speed data is missing from 18:00 to 12:00.

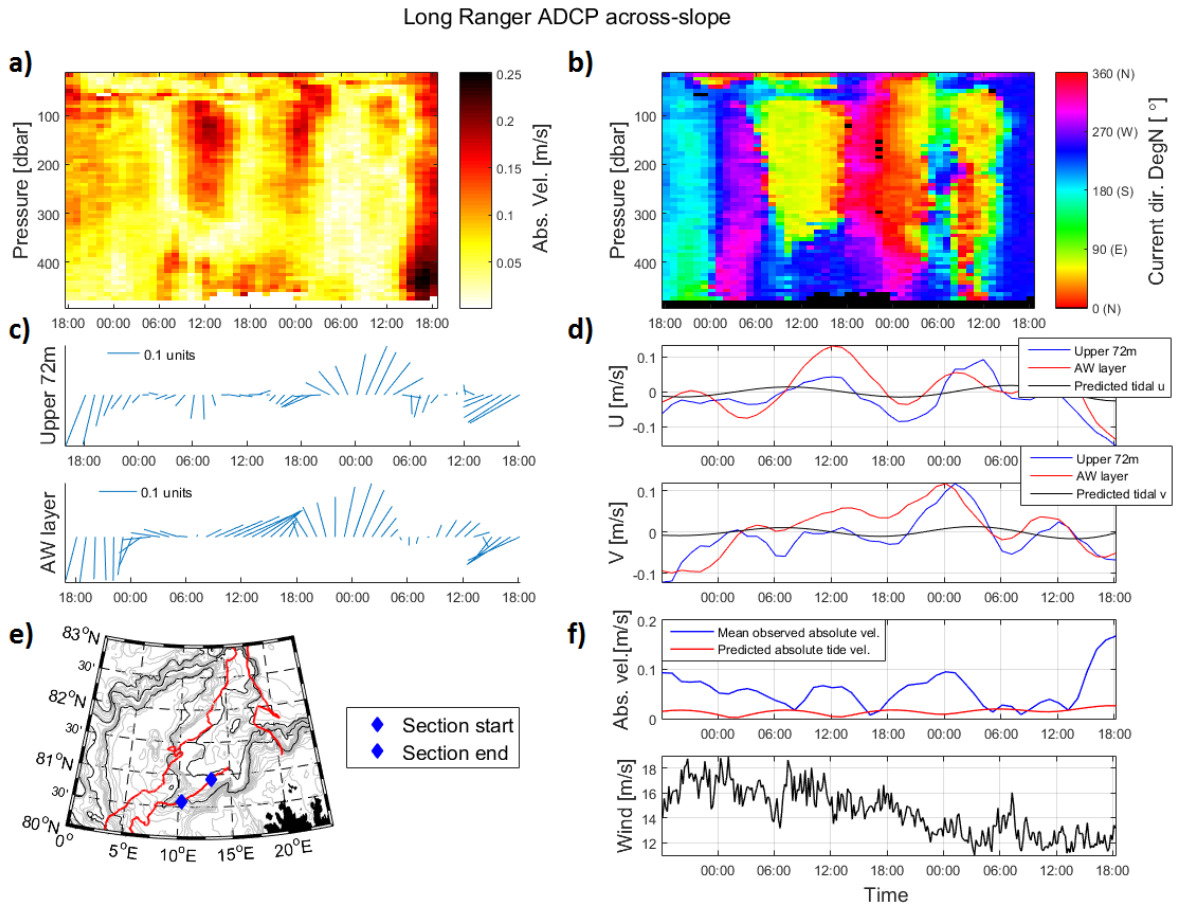

Figure 4.20: Zoom in on one across Slope section showing Long Ranger current velocity data during drift 3 and 4. a) absolute current strength, b) current direction, c) stickplot showing strength and direction of the current in the mixed layer (above 72 m) and AW layer (below 112 m), d) u and v in the mixed layer and AW layer, e) map showing the location of the section, and f) vertically averaged absolute current strength compared with predicted tidal velocity from AOTIM5 and wind speed.

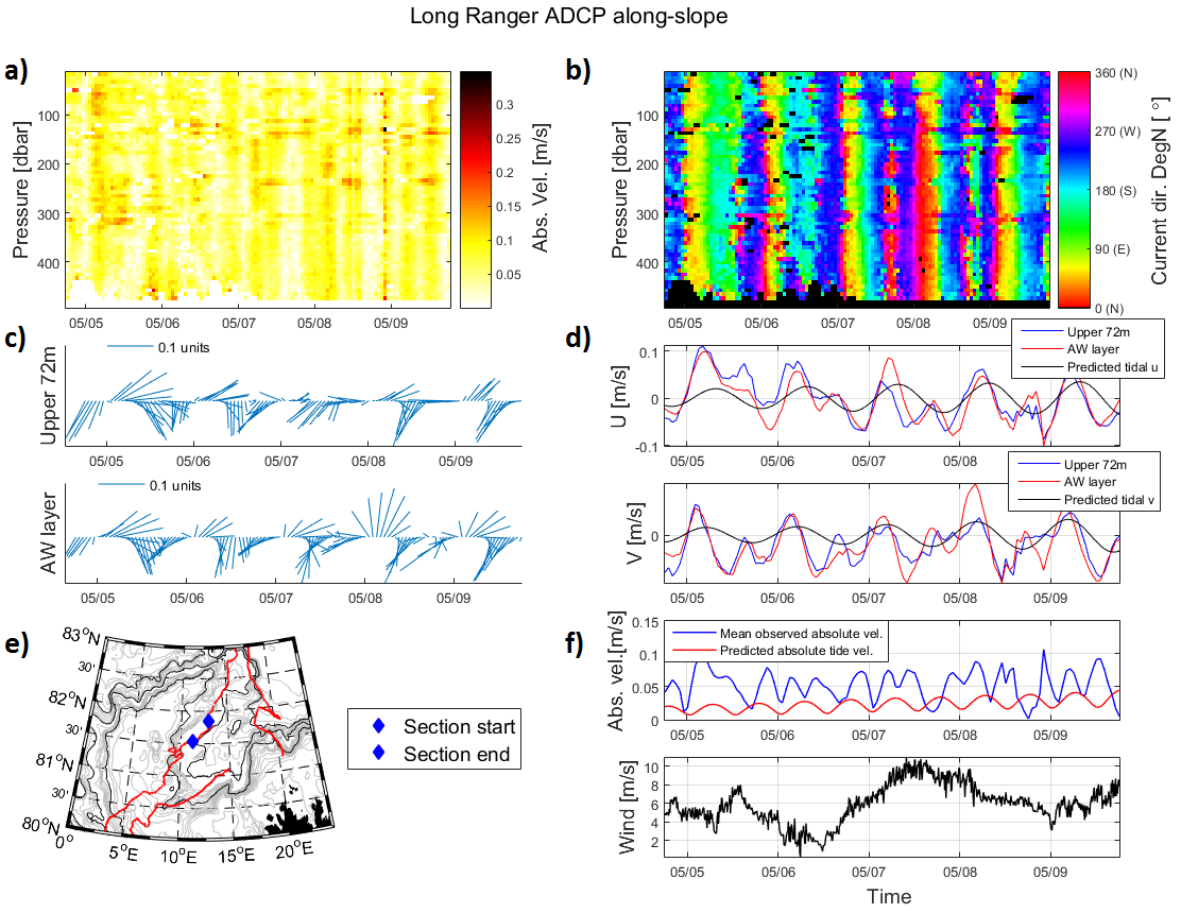

Figure 4.21: Zoom in on one along Slope section showing Long Ranger current velocity data during drift 3 and 4. a) absolute current strength, b) current direction, c) stickplot showing strength and direction of the current in the mixed layer (above 72 m) and AW layer (below 112 m), d) u and v in the mixed layer and AW layer, e) map showing the location of the section, and f) vertically averaged absolute current strength compared with predicted tidal velocity from AOTIM5 and wind speed.

4.5 Evaluation of a simple 1-D sea ice growth model

A 1-D convection model was applied to investigate the winter evolution of a sea ice cover and its sensitivity to oceanic heat. Benchmark experiments were initialised with mean temperature and salinity profiles from the PHC3.0 climatology (Fig. 4.22 a). Due to haline convection only, the convection reaches 160 m depth for an ice growth of approximately 0.8 m (Fig. 4.22 a). The growth season was set to end by the end of April, when solar heating should start to have an effect and we can expect summer melting to start. This is also comparable to the N-ICE2015 observations where melting starts on 25th May. Similar experiments were done for mean profiles from N-ICE2015 observations (Fig. 4.22 b,c,d,e). The major difference between the benchmark experiment and the experiment based on N-ICE2015 data is a reduction to almost one third of the ice growth. From the initial ocean profiles we see that the whole PHC3.0 profile is about 0.5 °C to 1 °C colder than the observed N-ICE2015 profiles. The higher oceanic temperature appears to lead to a reduction in ice growth for the N-ICE2015 profiles. With only approximately 0.25 m of ice growth for the N-ICE2015 run, the convection depth still reaches deeper than 300 m. The ice growth is slower than in the PHC3.0 run and levels out already in December, after which almost no ice growth occurs. The convection however, reaches deeper very quickly and reaches the PHC3.0 maximum depth already in December. It continues to deepen while there is little ice growth. After December/January the convection depth in the N-ICE2015 run undergoes several large jumps that are seen as big steps in Figure 4.22 b), d) and e). This will be explained in Chapter 5.3. Regional differences from the N-ICE2015 three sub areas (Basin, Slope, Plateau) are small, but ice growth is smallest on the Yermak Plateau and largest in the Nansen Basin. There is almost 20 cm difference in growth between the two. Convection reaches deeper on the Plateau than in the Basin and in the Basin no large jumps are observed.

The results described above have shown a large impact from the thermohaline structures on the sea ice evolution. Our main interest is to see the effect of changing AW properties on the sea ice cover. Therefore, the model was applied to profiles that are based on the PHC3.0 profiles but with a modified AW layer. Figures 4.23 and 4.24 show the evolution of ice cover for some profiles with gradually warmed AW and for some profiles where the AW has been moved upward (shoaled). The final ice thickness at the end of the growth season is affected very little if the whole AW layer is warmed gradually up to 2°C (Fig. 4.24). The maximum difference in final ice thickness is only 9 cm. If the AW layer is moved upward in the water column, no change in ice evolution can be seen until the initial AW layer reaches a depth of 80 m. When the AW layer shoals further, the final ice thickness decreases rapidly, i.e. the ice growth process is affected very little if the AW is only warmed, but very much if the initial AW layer shoals above a given depth. When we warmed the AW, we also added salt to keep the column vertically stable. If no salt is added, the warming AW would rise due to decreasing density (Fig. 4.24). The maximum rise due to warming of AW calculated from the density difference only is 10 m. This is not enough to have a large impact

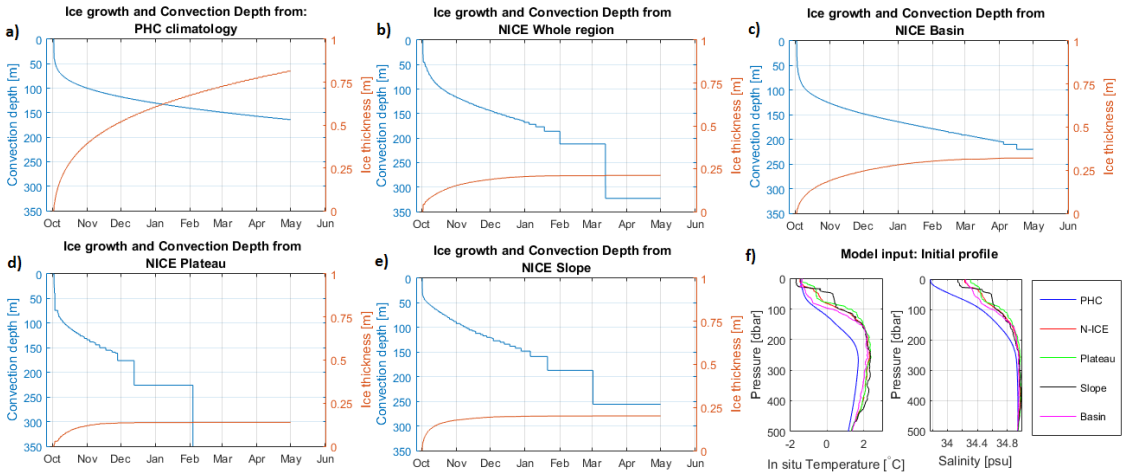

Figure 4.22: 1-D sea ice growth model results; sea ice thickness (orange) and haline convection depth (blue) for a) Benchmark experiment: PHC3.0 climatology input b) N-ICE2015 whole area mean input, c) N-ICE2015 Basin mean input, d) N-ICE2015 Plateau mean input and e) N-ICE2015 Slope mean input. Panel f) shows the input temperature and salinity profiles for the different runs.

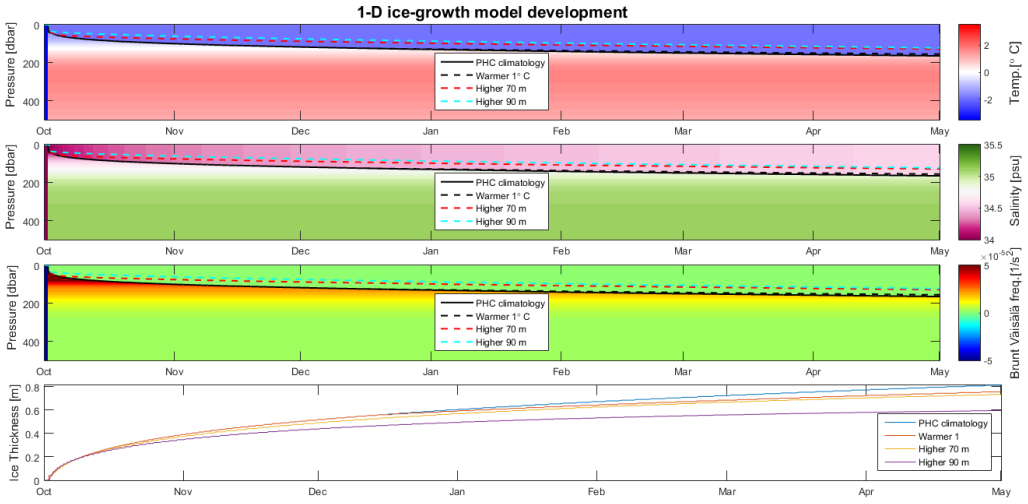

Figure 4.23: 1-D sea ice growth model results showing a time series of sea ice thickness, convection depth, salinity, temperature and stratification (buoyancy frequency) development throughout the growth season. Coloured in the background is the development for the benchmark experiment (PHC3.0 input), whereas lines are added showing sea ice thickness and convection depth for runs with warmed and lifted AW.

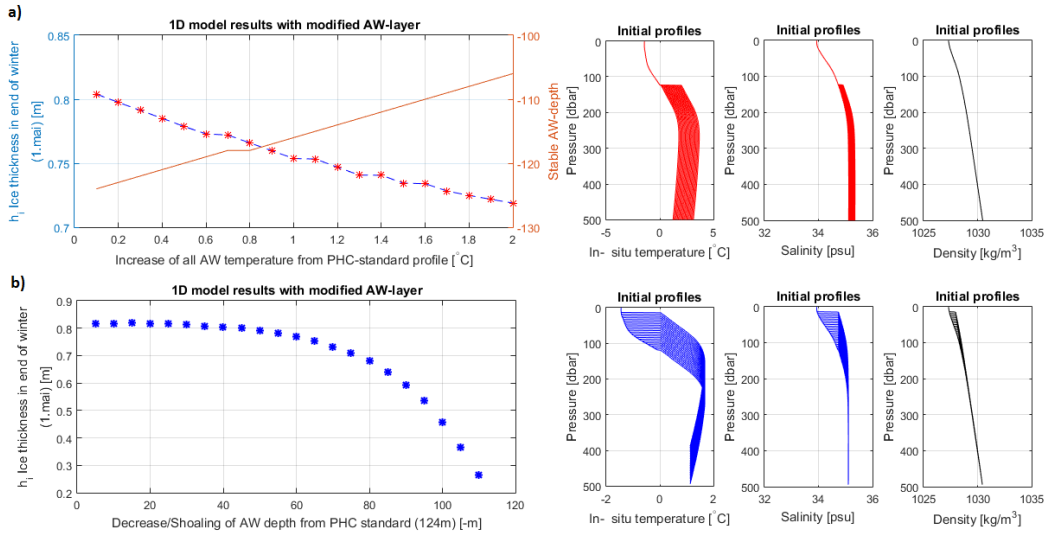

Figure 4.24: 1-D sea ice growth model run with modified AW. Panel a) shows the final ice thickness at the end of growth season (April) for the benchmark profiles (PHC3.0 input) with gradually warmed AW in the model initialisation. Salinity is added to keep the profile stable. The red line shows the stable depth of the AW if it is warmed but no salt is added. Panel b) shows the final ice thickness for the benchmark profiles with gradually lifted AW in the model input. The initial density profiles, based on initial temperature and salinity are given on the right.

on the ice growth. Initial ice thickness plays an important role for the evolution of the winter ice cover. Thicker initial ice leads in general to thicker ice by the end of the growth season (Fig. 4.25). Thin initial ice is affected more throughout the growth period by shoaled and warmed AW than thicker initial ice cover. If the initial ice cover is thicker than 1.2 m there is no visible impact on the ice due to warming or shoaling of the AW.

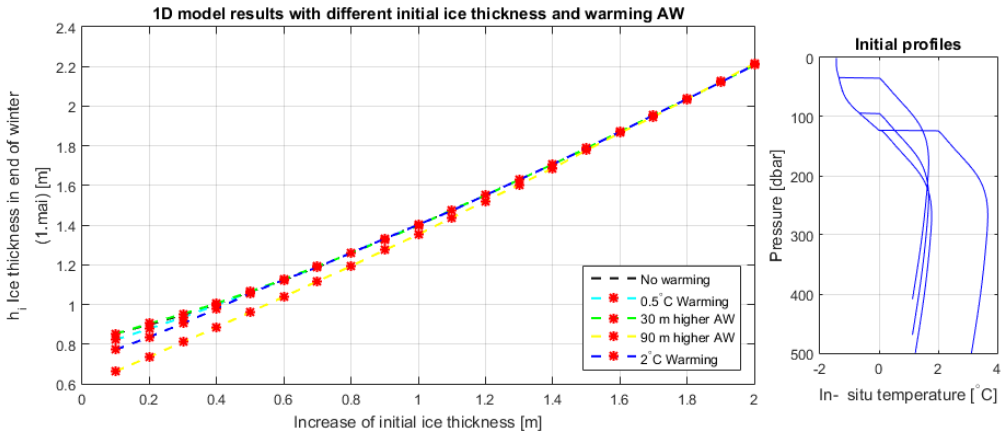

Figure 4.25: 1-D sea ice growth model results showing final ice thickness at the end of the growth season (April) for the benchmark profiles (PHC3.0 initialization) with changing initial ice thickness, lifted AW and warmed AW. Initial input temperature profiles are given on the right.

4.6 Evaluation of a fully coupled Earth System Model

Simulations from a global circulation model (NorESM) are analysed for the Arctic region to investigate the possible role of oceanic heat on the ice cover north of Svalbard. AW properties and values of sea ice bottom melting are presented here. Detailed information about the model and calculations are given in Chapter 3.3.2. Figure 4.26 shows the yearly mean AW core temperature from NorESM for a random year (2000). The AW inflow in the West Spitsbergen Current can clearly be seen, and we can follow the signal of warmer temperatures along its pathway through the Fram Strait, over the Yermak Plateau and then anticlockwise around the Arctic basin as an eastern boundary current. An inflow into the Barents Sea is also seen. The pattern of the AW core temperature spatial distribution is roughly the same for every year, but cycles of warm and cold pulses as discussed in Chapter 2.6.3 are observed (not shown). A zoom in on the N-ICE2015 area for 6 chosen years from 1960 to 2000 is shown in Figure 4.27. The pattern of warm AW follows the suggested current pattern (Fig. 4.14). Yearly images have been studied (not shown) and here we can observe a 5 year cycle of warmer pulses in the inflow of AW for parts of the time series. No large warm pulses are found between 1970 and 1985. In general, a positive warming trend can be seen in the core temperature. From the chosen years (Fig. 4.27) it can be seen that 1950 and 2000 had warmer AW core temperatures than the other years. The spatial resolution of NorESM, as can be seen from Figures 4.26 and 4.27, is around 50 km to 100 km in this area.

Figure 4.28 shows nearly constant simulated yearly mean AW depth in the West Spitsbergen Current (WSC) (south-western Fram Strait), while Figure 4.29 shows the same for the N-ICE2015 area. A warming trend of 0.008 °C per year is found in the AW core temperature in the WSC from 1950 to 2005 (Fig. 4.28). The shorter trend from 1978 to 2005, is 0.026 °C per year. This is similar to the trend of 0.032 °C per year observed in the WSC from 1975 to 2015. Calculating the trend from the values

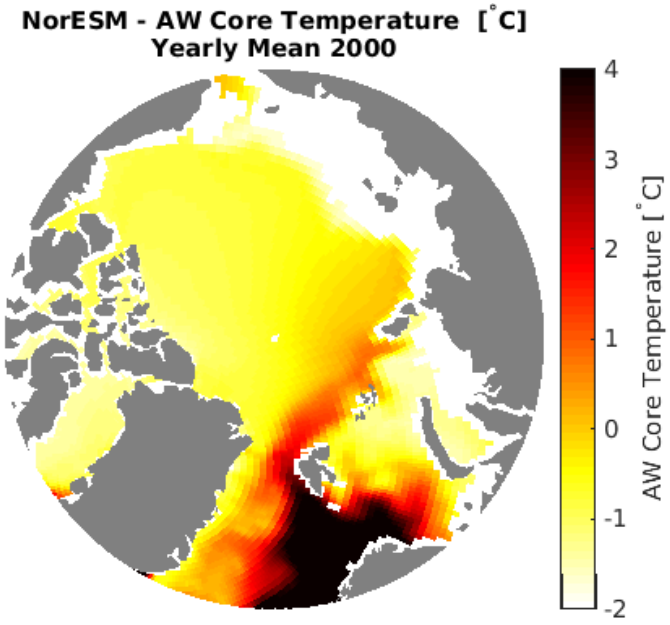

Figure 4.26: Spatial distribution of AW core temperature for a chosen year (2000) from the NorESM model.

only until 2005, for direct comparison with the modelled values, gives a trend of 0.040 °C per year (not shown). This is even higher than the trend for the longer series, and approximately 0.014 °C per year higher than the simulated trend.

Values for the N-ICE2015 area are divided in Plateau and Basin, because the resolution of NorESM does not allow the Slope to be captured accurately. The simulations show that the Basin warming trend is the same as in the WSC (0.008 °C/year). On the Plateau, the trend is slightly smaller (0.006 °C/year). The simulated AW is close to the surface when it enters the Fram Strait (Fig. 4.28), as suggested by earlier observations (Chapter 2.5). Consistent with historical observations, the AW core temperature in the WSC varies in the model, and it increases by approximately 0.5 °C from 1950 to 2000. Observations date back to 1978 and show two warm pulses just before 1990 and 1995 and one in 2005 (Fig. 4.7). Similar warm pulses are found in the simulations (Fig. 4.28). Observed temperatures are higher than simulations by NorESM.

In the N-ICE2015 area, AW core temperature is relatively stable in NorESM with only a small increasing trend (Fig. 4.29). AW core temperature is generally lower in the Basin than on the Plateau. This is consistent with the climatologies, but N-ICE2015 observations do not show such differences. N-ICE2015 observations show a mean AW depth of approximately 100 m with a maximum depth of 136 m. The difference between Basin and Plateau is minimal. The AW depth in NorESM has a mean just above 200 m in the Basin and just below 100 m on the Plateau.

NorESM simulates large values of bottom melting in the area north of Svalbard and especially over the Yermak Plateau as well on other shelf regions and in the Barents Sea (Fig. 4.30). During summer, bottom melting occurs over the entire Arctic Ocean, but during the winter months it is limited to the inflowing AW region. Yearly and spatial means are shown in Figure 4.31. In the N-ICE2015 Basin area, bottom

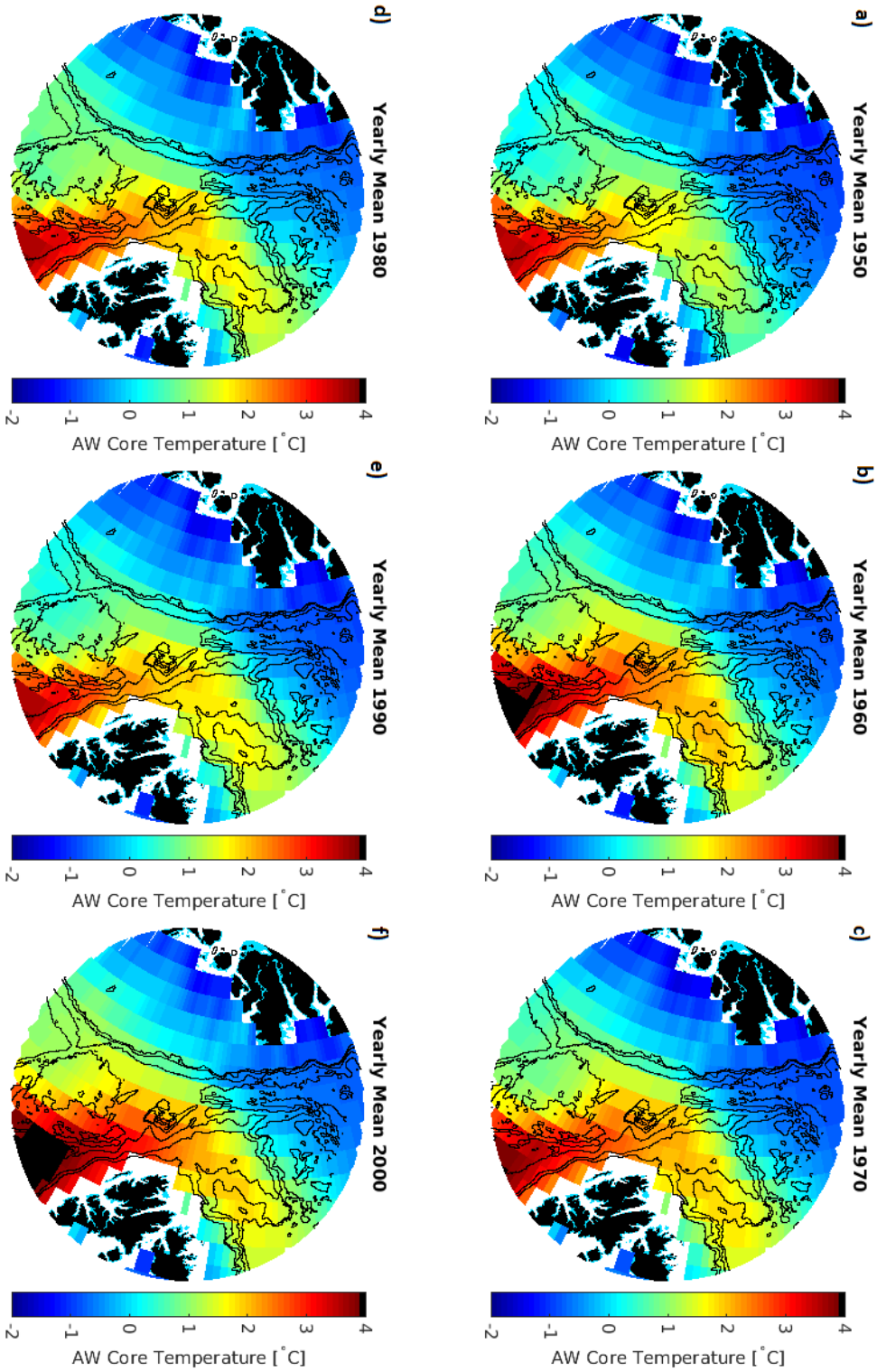

Figure 4.27: Spatial distribution of AW core-temperature for six chosen years in the N-ICE2015 area from the NorESM model for a) 1950, b) 1960, c) 1970, d) 1980, e) 1990, and f) 2000.

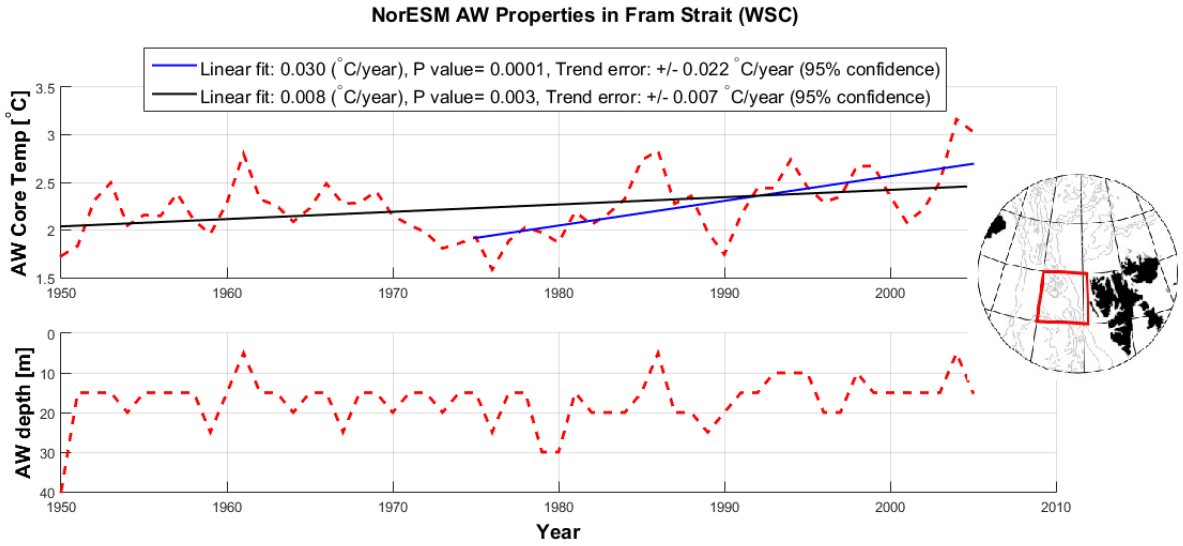

Figure 4.28: Simulated AW core temperature and depth from the NorESM model in the West Spitsbergen Current (southern Fram Strait, spatial mean from $78°N-80°N$ *and* $0°E-10°E$*). The trend error is calculated relative to the 95 % confidence band.*

melting is low throughout the winter period and it reaches a peak only during summer together with the rest of the Arctic Ocean. On the Plateau however, melting occurs steadily throughout the whole year peaking in summer. Figure 4.32 shows the correlation between simulated AW temperature in the Fram Strait and sea ice bottom melting. Positive correlations, indicated by red and yellow areas, reflect that positive temperature anomalies in the Fram Strait co-vary with more melting in these areas. Warmer water results in more melting and colder water results in less melting. The figure shows a similar correlation with AW depth. The two lower panels show how AW properties at the inflow in the WSC correlate with the AW properties in the N-ICE2015 area. There is a high correlation between AW core temperature in the WSC and on the Plateau (r=0.89, r^2=0.79) and smaller between WSC core temperature and that in the the Basin (r=0.44, r^2=0.19)(Fig. 4.32). The correlation between AW depth in the inflow and the N-ICE2015 area is smaller (r=0.48 and r^2=0.23 for the Plateau and r=0.31 and r^2=0.10 for the Basin).

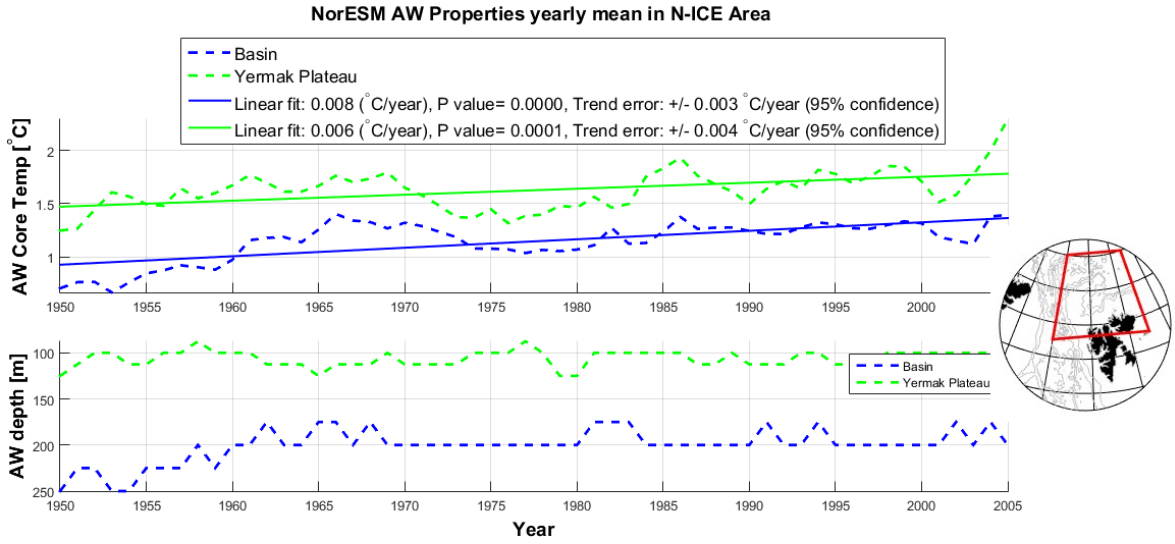

Figure 4.29: Timeseries of AW characteristics in the N-ICE2015 area from the NorESM model. The trend error is calculated relative to the 95 % confidence band.

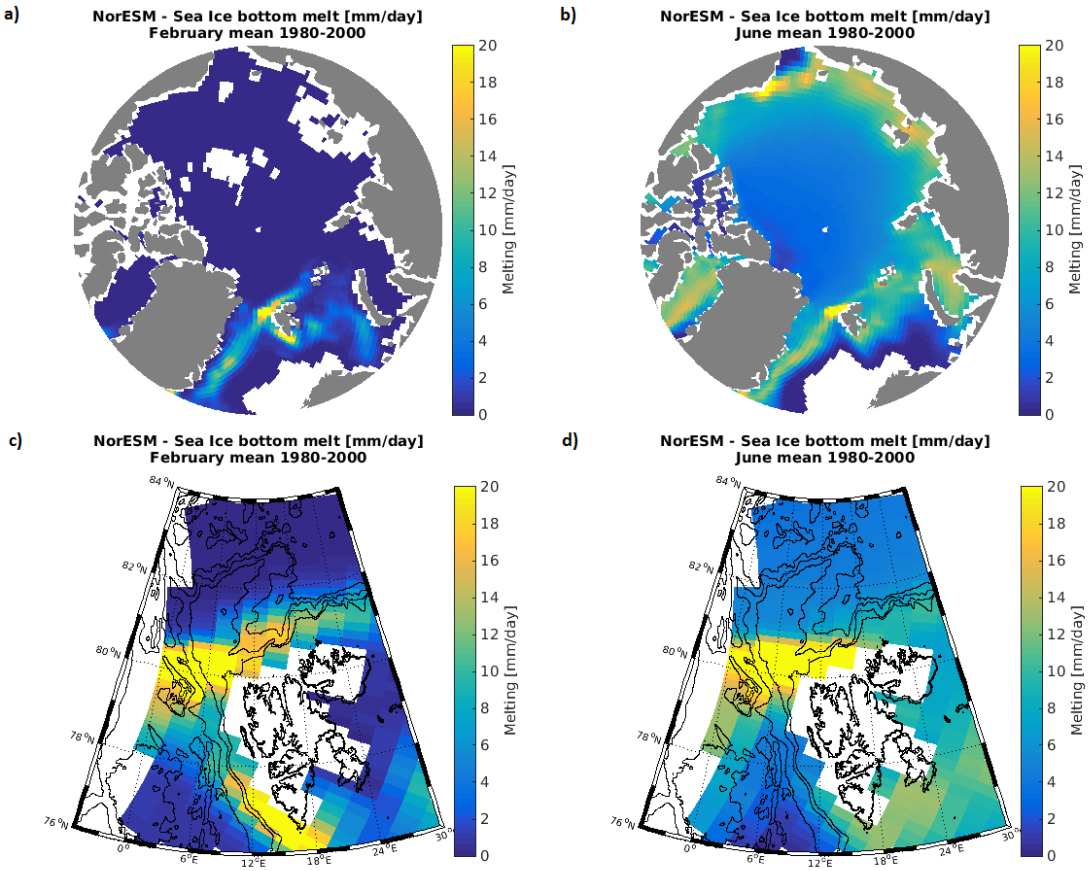

Figure 4.30: Values of Arctic sea ice bottom melting in the whole Arctic and in the N-ICE2015 area for a) February mean 1980-2000 (freezing season) and b) June mean 1980-2000 (melting season).

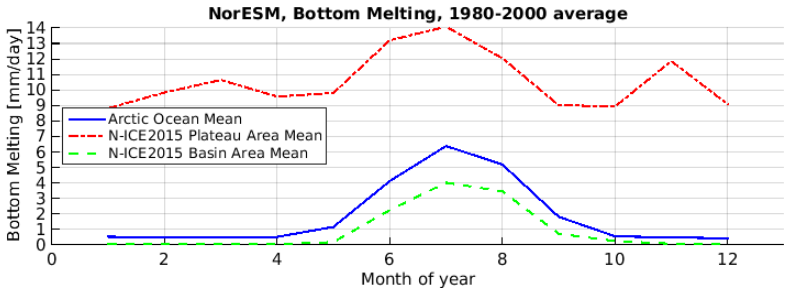

Figure 4.31: Yearly evolution of Arctic sea ice bottom melting values from the NorESM model for the whole Arctic Ocean and the N-ICE2015 area.

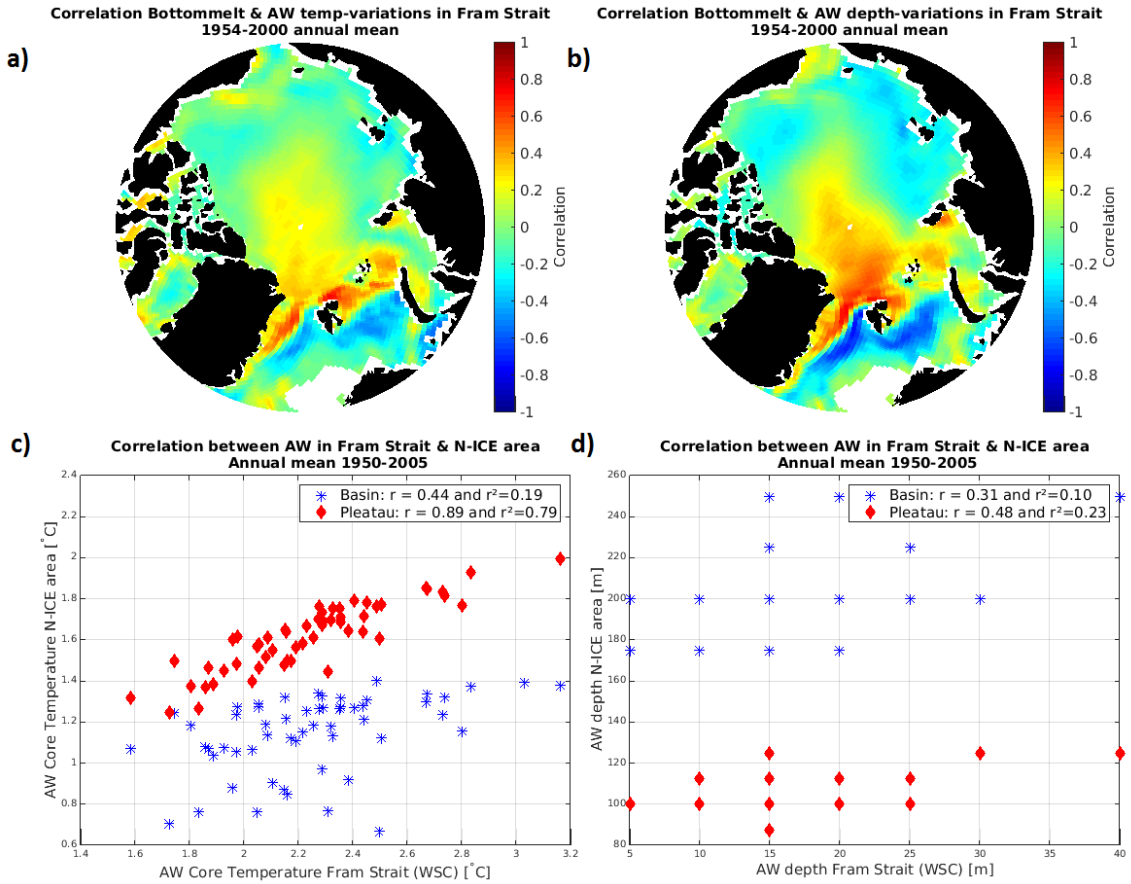

Figure 4.32: Top panels show spatial correlation between Arctic sea ice bottom melting and variations from the NorESM model of a) AW core temperature and b) AW depth. Lower panels c) and d) present correlations between AW properties in the Fram Strait and the AW properties in the N-ICE2015 area. Panel c) shows core temperature and panel d) shows AW depth.

Chapter 5

Discussion

The hydrography and currents in the N-ICE2015 campaign region north of Svalbard were presented and contrasted with historical data in Chapter 4. Based on these observations, we will here discuss differences and changes with a particular focus on the Atlantic Water (AW). We will also describe local processes that affect the AW which can be identified in the observations. Finally, we will discuss how changes in the AW characteristics may affect the sea ice cover.

Historical measurements of inflowing AW core temperature in the southern Fram Strait show a warming trend over the past decades (Fig. 4.7). Compared with some climatologies, our N-ICE2015 observations also reflect such warming. However, compared with other observations, no warming can be identified. The AW characteristics may be partly controlled by topography, partly by the distance from the inflow, partly by the inflow characteristics, and partly by heat and salt fluxes to the atmosphere and/or sea ice. AW characteristics and stratification may control sea ice growth and melt, where higher and warmer AW could limit the growth and also melt sea ice from below, even during winter. Vertical mixing due to internal waves generated by tides, storm activity and a mobile as well as loose ice cover could play important roles in this process. This will all be discussed in detail here.

5.1 Hydrographic changes of Atlantic Water

The timeseries of inflowing AW core temperature (Fig. 4.7) shows a steady long term warming over the past few decades. These measurements, however, do not present the full picture, as they are only annual snapshots from August. Although regularly spaced in time, they are not annual means and do not give us information about the yearly fluctuations or shifts in seasonality. Taking into account other observations that reveal warming of AW (Chapter 2.6.3) we do however, assume that the warming trend observed in these observations would hold even if the temporal sampling resolution was higher.

5.1.1 Challenges with historical comparisons

All the climatologies used in this study and observations from N-ICE2015 are similar for the deeper values (below 800 m, Fig. 4.10, 4.13). This consistency, i.e. that the same water masses are observed (Fig. 4.11) strengthens our comparison, because we expect the deep waters to change little over time. Hence, the data appears to be of good quality and make a comparison possible.

In the N-ICE2015 area we have to base our conclusions regarding temporal change in hydrographic conditions on a comparison with sparse measurements, irregular in both time and space, and interpolated climatologies. This is often the case in remote polar oceans and seas, but it does imply some limitations and challenges in the comparison. In the PHC3.0 (until 1998, Steele et al. (2001)), for example, we do not know from exactly where or when the observations are (Chapter 3.2.5). For the interpolated WOA13 (until 2013, where PHC3.0 data are not included in WOA13, Locarnini et al. (2013)) we do not know how many data points have been used in the different regions to create the interpolated gridded climatology. For some areas there may be several observations over a large time period, while for other regions there may only exist a few observations with large temporal spacing, or none at all. We see that regional differences are large (Fig. 4.3, 4.4, and 4.8) and that local topography plays an important role in determining the hydrographic conditions in the N-ICE2015 area. The rough resolution of the climatologies and the sparse geographical spreading of historical data therefore make comparison difficult. The regional separation into basin, slope and plateau areas improves this slightly, although we believe that differences are still large within these regions, for example between the western and eastern part of the basin, the northern or southern part of the plateau, or the northern or eastern part of the slope. This is illustrated well by the REALWOA data (observations until 2013, Fig. 4.13) which consists of real profiles that are not interpolated, has large regional differences and has large standard deviation within the three distinct regions. This is likely due to the fact that the calculated mean are from a few cruises in different parts of the region at different times. We have to keep in mind these limitations of the historical data comparison when we discuss the results.

The surface layer in the different climatologies (Fig. 4.13) should be treated with some care. In the Arctic Ocean both during winter and summer we expect a mixed surface layer, with varying depth. In our profiles of the PHC3.0 and WOA13, we cannot see evidence of a mixed layer except in the winter basin profiles. This is probably caused by the method we used (Chapter 3.2.5) to spatially average the one degree grid cells to a larger region. Some grid cells have AW close to the surface, and this together with the rough vertical resolution of the climatologies will make the mixed layer disappear in the spatial average. If the mixed layer depth varied a lot spatially in the region it would not show up as a mixed layer in the mean profile. It would be interesting to investigate further the spatial distribution of the mixed layer depth in the climatologies.

5.1.2 Atlantic Water change in the N-ICE2015 region

Compared to the PHC3.0, the N-ICE2015 observations of AW are both warmer and closer to the surface for all regions (Fig. 4.13), in agreement with previous conclusions (Chapter 2.6.3), and this backs up our hypothesis that the AW is warming. Compared to the WOA13, N-ICE2015 observations show a colder mean AW temperature and deeper AW depth in all regions except the basin. However, our observations are still within the standard deviation of both climatologies. The WOA13 shows the warmest and shallowest AW. The difference between the climatologies is large, and the reason for this is partly explained in Chapter 3.2.5. WOA13 contains more recent data than the PHC3.0. The more recent temperature data are expected to be warmer than the older temperature data due to the warming trend. On the other hand the WOA13 lacks many of the older (and colder) observations from for example Russian submarines in the northern part of the region that are included in the PHC3.0. We therefore conclude that it is likely that the most realistic climatological mean for the region lies between the PHC3.0 and the WOA13 (Fig. 5.1). This is more similar to what is measured during the N-ICE2015 campaign, and we could therefore argue that the observations from N-ICE2015 are similar to the climatological mean and colder than other recent observations (REALWOA from 1997-2013). From this we can conclude that we did not observe any warm pulse in the 2015 measurements and that the REALWOA is warmer probably because it includes the warm pulse from 2003 to 2007 (Chapter 2.6.3 and Fig. 4.10). Due to the lack of historical data in the N-ICE2015 region and our observations being close to what we believe is the climatological mean, we cannot confirm or invalidate AW warming over a longer timescale than what is shown in Figure 4.7. Looking at a long timescale we know that low frequency oscillations (50-80 year time scale) have been documented (Smedsrud et al., 2013; Polyakov et al., 2004; Polyakov, 2005; Jones, 2001). We know from comparison with the Fram expedition's measurements (Fig. 4.12) that the region was colder 115 years ago. We also know that is has been as warm as it was in 2015 before, during the Nautilus 1931 expedition (Fig. 4.12). It is possible that this was a warm pulse, as described in Chapter 2.6.3, but it is also possible that this period was a warmer period in the long term, low frequency oscillation as described by Polyakov et al. (2004) and Polyakov (2005) (Fig. 5.1). To investigate this further we would need longer timeseries at fixed points. N-ICE2015 provides us with a winter to spring season, but it is still only one season.

Based on snapshots from literature and from what we have observed, we believe that the last 35 years ($\sim$ 1975 until $\sim$ 2010) have been a warm period in AW temperatures flowing into the Arctic, with an increasing trend throughout this period. This fits our theory that AW is warming over time. However, such a warm period may have occurred before, for example around the 1930's (Fig. 5.1, Polyakov et al. (2004); Polyakov (2005)), suggesting that the warming trend observed, may be part of a long term oscillation.

The AW core temperature simulated by NorESM in the Fram Strait (Fig. 4.28) is comparable with the observed timeseries from the same location (Fig. 4.7). A warming

trend is observed in both, but the modelled trend is smaller than the observed trend (Fig. 4.28). From 1978 the trends are very similar, and as discussed earlier this may be partly due to anthropogenic forcing and partly due to a long term oscillation. In Figure 4.28 it appears that a full cycle of a long term oscillation is captured as well. This cycle has a top between 1950 and 1960, a bottom between 1970 and 1980 and a new top after 1985. If we assume that this is natural long term variability that is captured by the model, then the trend observed in the full timeseries of simulated AW core temperature in the Fram Strait (0.008 °C/year) may be attributed to anthropogenic forcing. This would be 0.4 °C warming from 1950 to 2000, which is consistent with the global temperature increase of 0.5 °C over the past 50 years. If we assume that 0.008 °C is due to global warming and anthropogenic activity, then $\sim$ 30 % of the observed trend in Figure 4.28 may be due to global warming and anthropogenic activity and 70 % may be due to natural, long term variability. The trends in AW temperature are also observed further north in the N-ICE2015 are, and here it is interesting to note that the trend in the Basin is the same as in the WSC, but that the trend on the Plateau is slightly smaller (Fig. 4.29).

During the last 35 years, several shorter term oscillations have been observed as warm (or cold) pulses on top of the general warming trend (Fig. 4.7)(Polyakov, 2005; Polyakov et al., 2010; Dmitrenko et al., 2006, 2008). These inter annual oscillations in AW core temperature can also be seen the simulated timeseries of AW core temperature (Fig. 4.29). The frequency and amplitudes of these oscillations are not completely the same as what is observed over the last few decades, but we expect that the model does not simulate the "real" world perfectly, it gives its own representation of the physical system and processes at hand. The oscillation of AW core temperature is also seen in the yearly maps of the simulated spatial distribution of AW core temperature, where some years clearly stand out as warm pulses (Fig. 4.27).

We observe that the N-ICE2015 observations are slightly colder than what has been observed as the mean for the last 10-15 years. It is possible that this change is either because we are in a cold higher frequency pulse (in between warm pulses), but still on a long term (50-80 year) warming trend (option 1 in Fig. 5.1), or that we have reached the top of the long term trend and started a cooler long term period (option 3 in Fig. 5.1). A third option is that due to global warming and anthropogenic influence, the possible long term oscillation as has been described here (Chapter 2.6.3), is disturbed and the global warming wil work against long ter cooling trend, resulting in an oscillation around a relative warm mean temperature (option 2 in Fig. 5.1). Which one of these scenarios is right is difficult to tell at this point, but continuous measurements for the years to come and model simulations will reveal more about the long term change of AW.

5.1.3 Other noticeable difference in historical comparison

Below 300 m, the N-ICE2015 observations are slightly fresher than the climatologies and the Nautilus observations (Fig. 4.10), and much fresher than the observations

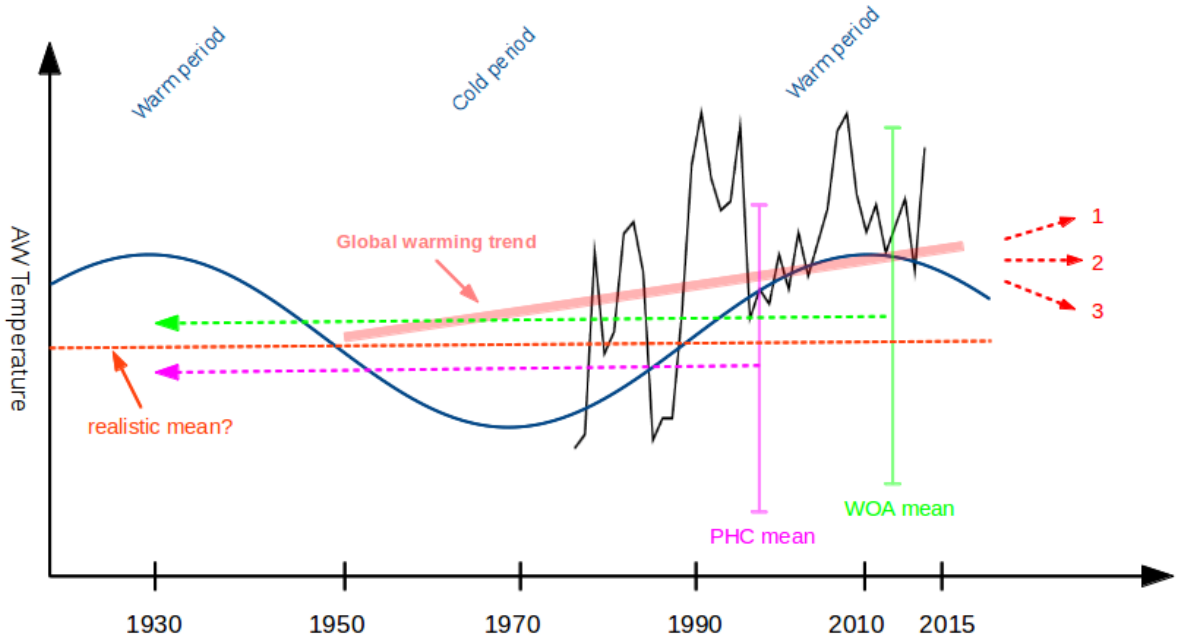

Figure 5.1: Sketch illustrating the long term AW temperature variability. The blue curve represents the suggested natural long term variability with two warm periods and one cold period. The black curve is the observed AW temperature in the Fram Strait from Figure 4.7, and the red curve represents the suggested global warming trend which may explain 30 % of the trend in the observations. The green and the magenta lines illustrate the difference in time scale and mean temperate between the PHC3.0 and WOA climatologies, and the orange represents a suggested realistic mean AW temperature. Three possible future scenarios are suggested. 1) A continued warming trend possibly due to global warming, 2) oscillation around a warm mean due to a combination of a increasing trend from global warming and negative long term variability, and 3) a cooling trend due to log term variability.

from Fram (Fig. 4.12). It is possible that the deeper Arctic Ocean layer experiences a small freshening. This would be coherent with the increased freshwater circulation described in Chapter 2.6.3, but we do not have enough historical observations to confirm or invalidate this theory. We do not now know the quality of the salinity measurements from Fram, which is a limitation for this comparison. Instrumental technology at that time was not as good as today. The fact that the salinities observed by Fram are much higher than those observed during N-ICE2015, and higher than one would expect in the Arctic in general, gives reason to treat these measurements with some scepticism.

The seasonal differences in the climatologies are comparable with the N-ICE2015 observations, as expected. The upper layer characteristics are hugely affected by sea ice growth, melt, and solar heat uptake at the surface. The AW core temperature also varies seasonally, similar to what is described in Chapter 2.6.2. An interesting point is that from the WOA13 data on the slope, the winter profiles are warmer than the summer profiles, which is not likely to be true. This difference could be explained by having single measurements in a region with very few measurements, and it may be more of a spatial difference than temporal difference.

The climatologies agree most on the Plateau and the difference is largest on the Slope. The fact that the N-ICE2015 temperature observations are closer to WOA13 in the Basin than other places, could suggest that, if there has been warming over the last few decades; it has warmed more in the Basin than on the Slope or the Plateau. We expect that that AW temperatures are coldest in the Basin, warmer on the northern part of the Slope, again warmer on the Plateau and warmest on the souther part of the Slope, closest to the AW inflow. This is almost correct for the climatologies but not for the N-ICE2015 observations that are coldest on the slope. At this point, we realize that the choice of our three "boxes", the Plateau, Slope and Basin, is not ideal, due to the large spatial difference within these boxes. For example it is a limitation that we have not divided the Slope in a northern and southern part (closer to the inflow) where we see large spatial differences. The fact that the N-ICE2015 observations are coldest on the Slope is also likely due to the fact that most of these profiles are from the northern parts of the Slope (Fig. 4.8). If we would have a good spatial average of slope profiles from the N-ICE2015 for the whole region, we would likely have a warmer average than the basin average. That the climatologies are warmer on the Slope than on the Plateau may be because the percentage of Slope profiles close to the inflow is larger than the percentage of Plateau profiles close to the inflow (Fig. 3.7). Again, this is evidence showing that regional dependence is very important in the N-ICE2015 region and this is a clear limitation of the spatially averaged climatologies. We observe that such regional differences likely are more important than the depth criteria we have used alone. For further studies, we would not divide the region to depth criteria alone but also to the location relative to the AW inflow area.

5.2 Atlantic Water characteristics and local processes

5.2.1 Temporal or spatial differences

Both temporal and spatial changes can be identified in the N-ICE2015 hydrography data (Figures 4.3, 4.4, 4.6, and 4.8). During drift 4, it is difficult to say if observed changes in AW depth, mixed layer depth and AW core temperature occur because it is the beginning of spring and melt season or because this part of the drift is close to the marginal ice zone and the AW inflow on the southernmost part of the Yermak Plateau (Fig. 4.3). We can compare the end of drift 3 and 4 as they are very close to each other (Fig. 3.2), but on the other hand are these drifts very different. Drift 4 was faster and in thinner ice than drift 3, and drift 4 was closer to the ice edge.

Drift 4 is over a region where AW is warm and close to the surface (Fig. 4.3), and we argue that this is due the location of the ship. Melting and solar heat uptake will create a shallower mixed layer, likely creating a new mixed layer on top of the older mixed layer. This is caused by an increased freshwater amount at the surface from both sea ice melt and solar radiation (Maykut and McPhee, 1995; Jackson et al., 2010). The observed differences are very large after just a short period of spring. This, together

with the fact that the AW core temperature increased more than it would have just because of seasonality, indicates that the changes we observe are largely due to spatial differences. Still, the seasonality is clearly visible in the N-ICE2015 observations, where we have two dominating regimes (Fig. 4.4): winter observations with deep and cold upper AW and a deep saltier mixed layer, and spring observations with warmer AW and a shallower and fresher surface mixed layer. When the melt season starts, we observe a freshening close to the surface (Fig. 4.3 and 4.6), which likely comes from the melting, a departure from the freezing point (Fig. 4.5), and creating stratification with steeper thermocline. The last is also likely due to melting (Fig. 4.3, Jackson et al. (2010)). In the spring season, the shallow AW and occasionally deeper mixed layer because of storms (Fig. 4.6 and 4.17) lead to enhanced heat fluxes and bottom melting (discussed in detail in Chapter 5.3.2). These changes can probably not be attributed to regional differences. In winter we do not observe the mixed layer tap into the AW layer. However, winter bottom melting is observed during the N-ICE2015 campaign (personal communication with Polona Itkin, Norwegian Polar Institute).

5.2.2 Atlantic Water characteristics partly controlled by topography

We have established that regional differences are clear in the N-ICE2015 observations. More precisely, the AW characteristics are partly controlled by the distance from the AW inflow. The warmest and shallowest AW is found on the plateau, and the coldest and deepest AW is found over the basin (Fig. 4.8). Although the warmest and shallowest AW is found when the water depth is also shallowest, we believe that this is controlled by the actual location of the station and not by changing water depth. Change in water depth alone would likely not change the AW characteristics. AW would probably flow around steep topography. If it flows over a shallow area, the depth of the top of the AW layer is probably not affected, since this is governed by other processes. Temperature should not be affected changing water depth either. This is supported by correlations between AW characteristics and water depth that are low over the N-ICE2015 area.

The distance from the inflow is almost proportional with the time the AW has had to cool and how long local processes have had to affect it. The further away from the inflow it is, the longer it has had to cool. A small part of the slope is closest to the inflow, however during N-ICE2015 no measurements were taken on the outer slope. Then follows the Yermak Plateau which is also the shallowest region. After this we get the slope on the eastern side of the Plateau, followed by the Basin. Of the observations taken on the plateau (shallow water), those showing the shallowest and warmest AW are all found on the middle of the Southern part of the plateau (closest to the inflow and below 81 ° N). This, and the fact that the calculated correlations between changing AW characteristics and distance to the AW inflow are high (Fig. 4.9), backs up our theory. We can conclude that the AW characteristics are partly controlled by location relative to the AW inflow, not by changing water depth alone, and as we will see onwards also partly by other processes.

5.2.3 Events and notable characteristics of the hydrographic observations

Only a seasonal halocline was observed in spring and no cold halocline was observed during winter (Fig. 4.2). At the end of drift 1 both the mixed layer and AW layer rise (Fig. 4.6). This occurs when the vessel drifts over the continental slope and is therefore likely connected to topography changes. Around the 10th of May, the surface mixed layer shoals and the AW layer deepens (Fig. 4.6). This event is connected to a minor storm (Fig. 4.17). It is also the only time during the timeseries when the AW depth and mixed layer depth change in the opposite direction (Fig. 4.6). We are unsure about the processes at hand in this event, why the mixed layers shoals, and not deepens due to the increased winds, or why the AW layer becomes deeper. It is possible that the sudden shoaling of the mixed layer is an early sign of spring and that it is a stratification due to melting of sea ice.

5.2.4 Local processes affecting Atlantic Water characteristics

Besides the local topography, other local processes can also affect the AW characteristics. Throughout the winter period, a thick surface mixed layer, possibly caused by haline convection, is observed (Fig. 4.6). Local sea ice growth determines the depth of the AW through haline convection. As we will see in the following section, the AW influences bottom melting, but the melting process in turn will influence the AW depth due to an increase in stratification from the melting. Another process that affects the AW is tidal mixing. This study does not have the suitable data to look at internal tidal waves or turbulent mixing with regard to tidal currents over steep topography, but literature (Chapter 2.7.3) suggests that this important around the Yermak Plateau. Increased tidal mixing can increase the mixing in and below the surface mixed layer, and hence add energy which could potentially lift AW. How this would affect the AW characteristics would be possible to look at in a future study. Also the amount and type of imported ice into the area could affect the AW characteristics (Alexeev et al., 2013).

Thicker, imported ice into the area will lead to less growth during winter, and hence less haline convection. A thicker sea ice pack breaks less, and therefore there is less turbulent mixing in the ocean due to wind. With thinner ice imported into the area there will be more turbulent mixing. On the other end, thicker ice usually has a rougher underside than thin ice which leads to more drag and hence more mixing. Which of these two effects is strongest we have not studied. There was actually more and relatively thick sea ice in the N-ICE2015 area than in the few foregoing years, making 2015 a “normal state” winter with good sea ice conditions and more comparable to 2011 conditions than 2012-2014 (Ivanov et al., 2016). We have not studied the sea ice characteristics in the area in particular, but because it has not changed drastically compared to earlier years before 2012, we assume that changing ice conditions have not had a large effect on the AW characteristics during our study period. This made comparison with climatologies possible. This assumption and the effect of different

types of sea ice flowing into the N-ICE2015 area on the AW characteristics would be possible to investigate in further depth in a future study.

5.2.5 Atlantic Water characteristics compared to mixed layer characteristics

Figure 5.2 shows regional temperature and salinity measurements in a T-S diagram. The mean near surface salinity during spring (after 25th May) and during winter are marked. There is a clear mixing line from the AW core (T $\sim$ 2.06 °C and S $\sim$ 35.1 g/kg) towards the point of mean winter near surface salinity (T $\sim$ -1.8 °C and S $\sim$ 34.4 g/kg). We ask ourselves why this "breaking point" is around S $\sim$ 34.4 g/kg, and not saltier or fresher. This "breaking point" is consistent through most of the drift and similar to what is observed by Rudels et al. (2015). To investigate this we have calculated a "Gade-line" (Gade, 1979, 1993). Here it is assumed that a volume of AW is used to melt sea ice, the cooling and freshening of the mixed result, is solely dependent on temperature and salinity. As more meltwater is added to the well mixed volume, its properties evolve along a straight line in temperature and salinity space (Gade, 1979; Jenkins and Holland, 2007). We thus assume that a volume of AW is cooled to the freezing point, and that all the heat that is become available in this process is used to melt a volume of sea ice, conservation of heat and salt gives an estimate of the salinity in the layer below the ice at the end of this process (Chapter 3.4.10). The "Gade-line" (Fig. 5.2) calculated from the mean winter AW properties (T $\sim$ 2.06 °C and S $\sim$ 35.1 g/kg) predicts a near surface salinity of 33.7 g/kg, which is exactly the same as the spring mean, but fresher than the winter mean at the "breaking-point". A mean sea ice salinity of 7 g/kg is used.

Here we have chosen to ignore the fact that atmospheric heat will also melt sea ice during spring and summer, and that the near surface freshwater may have other sources as well, such as river input or precipitation. Studies of oxygen isotopes, however, have indicated that only a very small percentage of the freshwater in the N-ICE2015 region originates from river input (personal communication with Paul Dodd, Norwegian Polar Institute, May 2016). This supports the theory that most of the freshwater in this region originates from melting of sea ice (personal communication with Bert Rudels, May 2016).

The reason why our winter "breaking point" is saltier than the "Gade-line" estimates is likely that not all of the AW heat is used to melt ice. A part is likely lost to the atmosphere (Rudels et al., 2015). If we assume that 70 % of the heat loss goes to the atmosphere and not to sea ice melt (Rudels et al., 2015), the "Gade-line" predicts a near surface salinity of 34.7 g/kg (purple star Fig. 5.2). This is closer to the observed winter near surface salinity of 34.4 g/kg than the first "Gade-line" calculated, but slightly more saline. This difference might be due to other freshwater input from rivers and precipitation. Another limitation of this calculation is the varying AW temperature. In our calculation, we have used the mean winter core temperature of 2.06 °C. If we use the maximum core temperature observed during winter (3.27 °C) the resulting winter

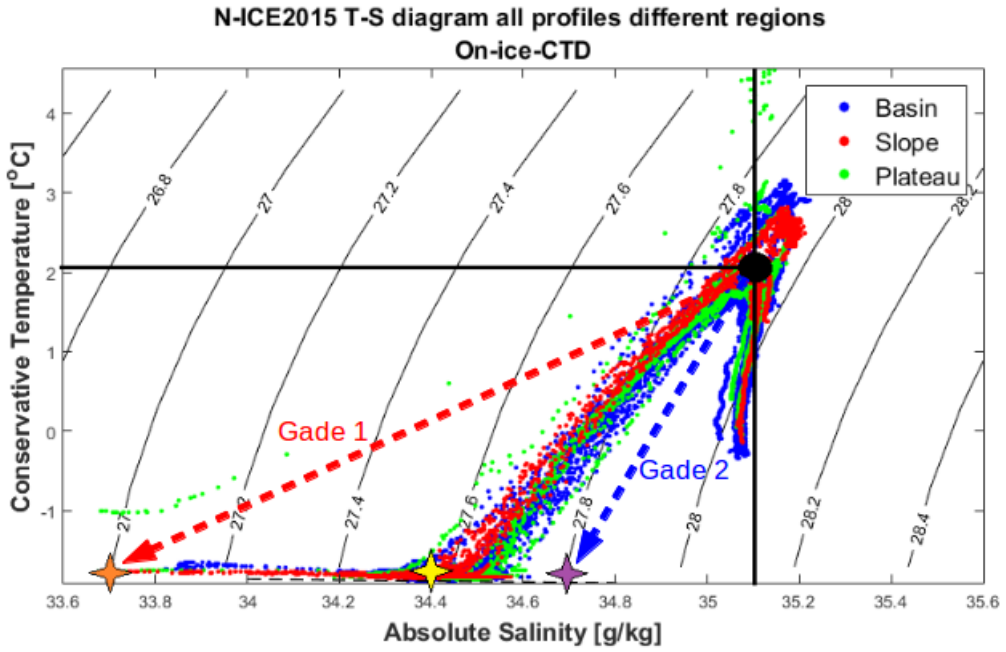

Figure 5.2: T-S diagram with scatter of on-ice CTD observations from N-ICE2015 divided in 3 distinct regions. The black dot represents the mean AW core charactersitics during winter ($T \sim 2.06$ °C and $S \sim 35.1$ g/kg). The yellow star denotes the mean near surface salinity during winter (34.4 g/kg) while the orange star denotes the mean near surface salinity during spring (33.7 g/kg). The red dashed line represents the "Gade-line" calculated if all available AW heat is used to melt sea ice. The resulting predicted near surface salinity coincides with the mean spring salinity. The blue dashed line represents the calculated "Gade-line" if 70 % of the AW heat is lost to the atmosphere and only 30 % is available for melting sea ice. The purple star denotes the resulting predicted near surface salinity (34.7 g/kg).

near surface salinity would become 34.6 g/kg which is close to the observed mean of 34.4 g/kg. It is very likely that the 70 % of heat lost to the atmosphere as estimated by Rudels et al. (2015) is not accurate now or for this region. It has also been shown that if the AW gets warmer, a smaller percentage of heat will be lost to the atmosphere (Rudels et al., 2015). If we assume that other influences on the near surface salinity are negligible , and we calculate a "Gade-line" to 34.4 g/kg, then 44 % of the heat must be lost to the atmosphere (not shown in figure). Regional differences in the tilt of the mixing line as observed in Figure 5.2, could possibly mean that there is a difference between the regions in how large fraction of AW heat that is lost to the atmosphere.

Our spring observations are from a period with sea ice melting from above due to solar radiation and warm air temperatures, and melting from below due to warm AW near the surface (close to the inflow). This combination makes it difficult to say how much of the melting is caused by oceanic heat or atmospheric heat. Again, this influences the calculation of the "Gade-line". We therefore believe that the first Gade-line coinciding with the mean spring near surface salinity is a coincidence. It is also believed that the additional melting occurring in spring and summer does not affect the near surface salinity in winter (Rudels et al., 2015).

This study has its main focus on the AW characteristics and its influence on sea ice. However, a more detailed investigation of mixed layer characteristics, and how these are influenced by the AW characteristics, and local processes such as melting of sea ice, would be interesting to include in a future study.

5.3 Influence of Atlantic Water on the sea ice cover

It has previously been thought that AW does not have a large impact on the Arctic sea ice cover, and that ocean heat fluxes in the Arctic Ocean are negligible (Untersteiner, 1964). More recently, AW has been suggested to have a direct impact on the sea ice, especially where it enters the Arctic and in the area north of Svalbard (Onarheim et al., 2014; Ivanov et al., 2016; Alexeev et al., 2013). Confirming the ocean's role in the evolution of the Arctic sea ice pack is difficult given how short field programs usually are. Using the N-ICE2015 data and two types of models, we have made an attempt at describing the ocean's role in the evolution of the sea ice cover. The available simulations suggest that AW has a direct impact on the sea ice throughout the season in the Nansen Basin, on the slope and on the Yermak Plateau.

5.3.1 The flow of the Atlantic Water and turbulent mixing

The current data investigated in this study are obtained during drift 3, which mainly took place on the Yermak Plateau and the slope. Data from the vessel-mounted ADCP shows that for almost all current observations during the N-ICE2015 campaign, the observed flow is nearly barotropic with a rather high ice-ocean horizontal shear (as defined in Chapter 4.4). From the Long Ranger ADCP current data we observe that below 17 m depth, the flow follows the AW, and not the ice. This is in accordance with Rudels et al. (1996), who argued that the depiction of AW "diving" beneath the outflowing Polar Surface Water, as it enters the Arctic Ocean, is misleading (Carmack et al., 2015). Rudels et al. (1996) stated that shear may be present in the top few meters, but the thickness of the outflowing layer is not known. Thus, while a thin part of the mixed layer may follow the ice towards the Fram Strait, most of the mixed layer follows the AW flowing northward and towardsthe east (Carmack et al., 2015).

The mean flow observed on the Yermak Plateau in the upper 500 m is in south-western direction, which may be either recirculating AW from the inner Svalbard branch, a return flow from the outer Yermak branch, or AW water from the Basin flowing in southwesterly direction towards Fram Strait (Fig. 4.15). Given the high temperatures observed, it is not likely water from the Basin. No outer Yermak branch was identified in neither the observations nor simulations from NorESM (Fig. 4.14). Simulations therefore suggest that the southwesterly flow observed on the Yermak Plateau is due to the Svalbard branch that bends and recirculates. Again, the simulations may not have captured the AW core, and the Yermak branch may still exist although it is not visible in the vertical mean flow. In observations, the outer Yermak branch is likely not observed since the drift was not far enough to the west.

We observe a current with oscillations at tidal and wind frequencies, and want to find out what causes the observed signal. Tidal flow gives the largest signal in our observations (Fig. 4.17 and 4.18), which could indicate turbulent mixing near topography. The predicted tidal current frequencies from the AOTIM5 model (Padman and Erofeeva, 2004) are similar to observations. There is however, a large difference in observed and predicted tidal amplitude. Modelled diurnal tides are underestimated by almost a factor 2. In general, if the topography changes, the tides are influenced a lot (Fer et al., 2015, 2010; Padman and Dillon, 1991), and these topography changes may not be captured in the model. To evaluate the tidal model, we studied the topography the model uses and the actual water depth at our location (Fig. 5.3). The topography from the model is very similar to the ship echo-depth. This means that it is likely not the reason for the large difference in observed current amplitudes and modelled diurnal tidal amplitudes. There is only a small section where the AOTIM5 model uses a depth deeper that the actual depth, and this would give slightly smaller tidal predictions.

There must be other reasons for the differences between the observed currents and the predicted tidal currents. We know that the diurnal signal we observe is not only due to tidal forcing. For example, the observed signals can come from shelf waves. Wind forcing during storms generates internal waves at the near inertial frequencies that are close to 12 hours in the N-ICE2015 region (Gimbert et al., 2012; Fer et al., 2010). Such waves would be included in the observed current. The wind signal only propagates down to a certain depth, and our current observations are quite barotropic, but with a more advanced analysis of the different signals and frequencies and different depths, this could be investigated. Another issue that is not discussed in detail here is the roughness of the topography. The model does not appear to capture the effect of changing roughness on different scales very well. The roughness is defined as the variance in sea floor height in m^2 (Wu et al., 2011). If the topographic rougness is not well represented in the tidal model, tidal amplitudes will not be accurate. The model predicts the tidal velocities well when compared to current in the VMADCP data in the deep Nansen Basin, where the topography is very smooth, during drift 2 (personal communication with Amelie Meyer, May 2016). We also see that during drift 3, the predicted tidal components, u and v, are more similar to what is observed when the drift is on the top of the (relatively smooth) Yermak Plateau (12th-15th May and 24th-31st May). When Lance drifted over sloping topography (rougher topography). We believe the roughness is important for the tides, and it would be interesting to study this in further detail.

Three larger storm events are observed during drift 3 and 4 (Fig. 4.17 a), 20th-21st May, 1-4th June, and 12th June). During these events, the drift speed and the horizontal ice-ocean shear increase. After these events, the absolute current velocity appears to increase all the way down to 450 m. It is surprising if these events would have an impact on the currents so far down in the water column. The first two events mentioned coincide with the top of the spring-neap tidal cycle (Fig. 4.18 b) which likely increased the current velocity at all depths. It is possible that this is the dominant reason for the increased current velocities, and not the wind, but we are not completely

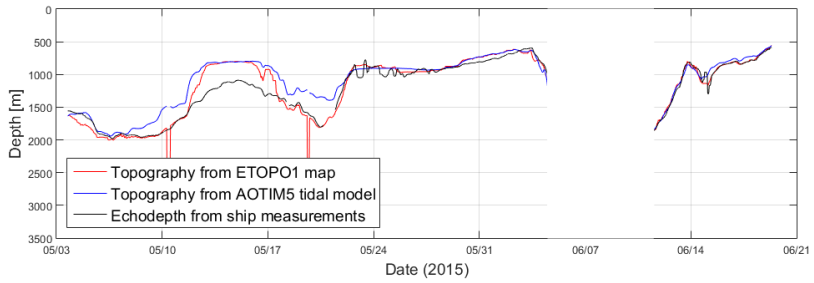

Figure 5.3: Bottom depth from the ETOPO1 map, AOTIM5 tidal model and observed depth from the ship echo-sounder during drift three and four while the Long Ranger ADCP was deployed. The ship echo-sounder gives spikes and disturbances around the seventh of June, maybe due to ice under the hull of the ship or other disturbances.

certain about this. It is also surprising that we do not see such a signal during the first top around 12th May, but here, again, regionality or roughness may explain the difference.

Previously, the Arctic Ocean has been described as an ocean with a thick and strong ice cover, which is not very mobile. The general movement of this ice cover would transfer momentum to the upper ocean layer, but the wind forcing would not induce much turbulent mixing (Padman and Dillon, 1991). During N-ICE2015 we observed the opposite, a rather mobile, breaking and "loose" ice cover. During periods with strong winds, the ice broke up and leads were frequently created. This again would lead to more turbulent mixing. The observations clearly show that the under-ice friction velocity increases with increasing wind (Fig. 4.18). The wind also leads to increased heat fluxes under the ice (Fig. 4.18). This will be further discussed in the next section.

Surprisingly, we observe little effect of topography on current strength and direction (Figures 4.19, 4.20, and 4.21). Although we only measure down to 500 m, depth we would because of the Taylor-Proudman theorem expect that the mean barotropic flow would follow the slope and topography changes (Marshall and Plumb, 2008). We would also expect a slight increase in current strength along the continental slope in shallow water (Cushman-Roisin and Beckers, 2011). For the slope sections, we generally observe a south-westerly flow, mostly across-slope. It is possible that we did not observe what we would expect because we did not drift right across the slope at any point.

5.3.2 The role of stratification and turbulent mixing

A lot of heat is available in the AW (Fig. 4.6 and 4.3), yet it is difficult for this heat to be mixed up to the surface because of the strong stratification (Fig. 4.3). We expect that the closer the AW layer and the mixed layer are, the higher the heat flux into the mixed layer is, and hence the higher the bottom melting is (Carmack et al., 2015). During N-ICE2015 shallowest AW depth occurs during the end of drift 1 and during drift 4 (Fig. 4.6). The heat content in the layer above the AW rises in spring, partly as a result of increased solar heat uptake (Fig. 4.5). However, it also increases in mid February (Fig. 4.5) during the polar night. This increase in heat content in the layer

above the AW in winter is connected to a major storm (not shown,) and presumably comes from warmer waters below. These findings agree with observations of under-ice heat fluxes from the TIC (Fig. 4.18). Heat flux observations from the TIC also show a very large increase in heat fluxes under the ice in spring. Here it is difficult to say whether the heat comes from solar heating or from the warm AW that is close to the surface at that time. We suggest that it is likely a combination of both atmospheric and oceanic heat fluxes. To quantify this, one would need to investigate the heat fluxes from the AW to the mixed layer. These measurements exist from micro structure profiles (MSS), but have not been analysed in this study. Under-ice heat fluxes double earlier in the time series (Fig. 4.18), coinciding with minor storms. This also happens during the polar night in drift 1 and 2 when there is no solar heat uptake (Personal communication with Algot Peterson, and Peterson et al. ,(in progress)). We therefore conclude that AW heat is brought to the surface mixed layer, through the stratification, and these fluxes increase with turbulent mixing due to increased atmospheric forcing (Fig. 4.18).

The observed stratification is strengthened in spring when the temperature difference between the mixed layer and the AW layer is larger (Fig. 4.3). This is also when the two layers are closest to each other. It does not seem logical that the ocean heat fluxes are largest when the stratification is largest, and some therefore believe that the large heat reaching the ice due to solar heating (Maykut and McPhee, 1995). All in all, there are several processes happening at the same time during the end of drift 4, and it is difficult to state what happens first and what is a cause or result of various processes. We observe AW closer to the surface, which is likely caused by the closeness to the AW inflow. We also observe high under-ice heat fluxes which may be due to the shallow AW or increased solar heat uptake. The solar radiation can also possibly go below the mixed layer. We observe melting due to the increased heat fluxes (oceanic but an/or atmospheric), which leads to a freshening of the surface ocean layer and strengthened stratification. This strengthened stratification makes it theoretically more difficult for oceanic heat to move upwards (Chapter 2.7.3).

Although the uppermost layer freshens, the total freshwater content in the layer above the AW stays nearly constant throughout the whole period, and actually goes down slightly during drift 4 (Fig. 4.5). We believe that most of the freshwater in the surface mixed layer north of Svalbard originates from ice melt (either the current or previous years) and that little originates from river inflow (based on personal communication with Paul Dodd, May 2016, isotropic composition $\sim$ 2 % river water). Then we could expect to observe a smaller freshwater content when we reach further south and closer to the AW inflow, because there has been less sea ice in general in this area the last few years (Ivanov et al., 2016), and hence also less ice melt. This matches our observations, and the idea is worth investigating further.

The turbulent mixing is also largely dependent on local topography, and hence varies a lot spatially. Since the bottom melting likely depends on both the AW characteristics and the magnitude of turbulent mixing, regionality will play a major role in the evolution of the ice cover. We know from literature that steep topography and ridge systems are sites of large-scale fronts and intensified circulation and mixing (Shimada, 2005;

Bluhm et al., 2015). Although it is found that the highest entrainment of heat from the AW to the mixed layer occur along the AW pathway, where the AW and mixed layer are in direct contact (Carmack et al., 2015; McPhee, 2003; Untersteiner, 1988; Sirevaag, 2009), bathymetry plays an important role in the distribution of vertical heat input to the surface mixed layer (Padman and Dillon, 1991; Lenn et al., 2009; Shaw et al., 2009; Sirevaag, 2009; Rippeth et al., 2015). For instance, high heat fluxes have previously been found (> 20 Wm^{-2}) over the Yermak Plateau, away from the main pathway of the AW (Carmack et al., 2015). It has also been found from analysis of records from the deeper central Eurasian Basin that delivery of heat from the AW to the mixed layer occurs away from steep or shallow topography (Polyakov et al., 2013). This has also been observed during N-ICE2015 (Peterson et al., in progress). This can probably be attributed to a large vertical velocity shear, double diffusive mixing, and haline convection. The fact that AW heat can be transported through the stratification, away from steep or shallow topography and also in winter, strengthens the theory that AW has a direct impact on the sea ice cover throughout the whole year and in the whole region. This statement will be emphasised in the discussion of the NorESM model results in the next sections.

5.3.3 Atlantic Water limiting sea ice growth

To study the effect of AW heat on the sea ice growth process we used a 1-D model as described in Chapter 3.3.1 and Chapter 4.5. It is important to note that this is a simple model which is useful to investigate some of the processes taking place, but there are some important processes not simulated by the model. The model simulates sea ice growth and related convection in a realistic way with high vertical resolution. However, firstly, the model does not include melting; i.e. at times when melting could be expected, the available heat is conducted through the ice until further freezing takes place. Secondly, no heat is advected to the column, so in reality, more heat would be added to the column when the haline convection "digs" down in to the AW layer. Finally no turbulent mixing is present and therefore no heat is diffused or mixed through the stratification. All these three processes, if included, would have made the effect of AW on the ice growth processes larger, i.e. the model underestimates the effect of AW heat. Melting would have affected the freshening of the surface layer, the increased stratification and the vertical diffusion. This would have a positive effect on the sea ice cover, where positive means a strengthening of the sea ice cover. A lot of time was spent in this study to analyse model results and to try out different methods. We stopped the model before spring starts, so solar heat uptake is not important, and during winter the contribution of short wave radiation is negligible.

We believe that warmer and shallower AW will limit sea ice growth, and that the heat which is delivered from the AW to the ocean surface as a result of winter convective mixing is the main reason for this effect, together with the turbulent mixing. Compared with the PHC3.0, the N-ICE2015 observations show a shoaling (~ 50 m) and warming (~ 1 °C) of the AW core (Chapter 4.3). Following this, the model run with

N-ICE2015 initialization leads to 2/3 less ice growth than with PHC3.0 initialization. With PHC3.0 initialization the model reaches into the AW layer in December, while with the N-ICE2015 initializations the haline convection reaches the AW layer already in mid October, just a few weeks after the growth season starts (Fig. 4.22). The main difference is that the N-ICE2015 initialization reaches the AW heat quicker, and once it does, there is also more heat available due to the warming. This leads to a slower ice growth and a continued dampening of the growth process with the N-ICE2015 initializations. The regional differences in the N-ICE2015 initializations lead to similar results. Most heat is available higher up on the Plateau, and this leads to a slower ice growth in the beginning. Where a lot of heat is close to the surface, such as on the Plateau and the Slope, the growth process slows down and stops already in December, while in the Basin the AW is deeper, resulting in relatively strong growth until January and minor growth onwards to May (Fig. 4.22).

In the results from the N-ICE2015 initializations we observe a big "jump" in the convection depth after a certain time and a staircase development following. This happens because the column suddenly gets unstable in salinity at depth. Since it is already unstable in temperature and the mixed layer depth was only kept because of the gradient in salinity, it suddenly turns unstable and mixes all the way down to where it is stable again. This process is strongest on the Plateau where there is most heat. The column is therefore more unstable in temperature on the Plateau than on the Slope and in the Basin. At a certain point (depth range 160-220 m) the column also gets unstable in salinity in the Basin but it is not so unstable in temperature that it gives a large staircase jump. During the N-ICE2015 campaign we did not observe mixed layer depth so deep that it would become unstable in salinity after haline convection, but theoretically this is possible. Recall that the model is likely overestimating the ice growth because it underestimates advection of AW heat, therefore the haline convection is likely overestimated as well. This study illustrates that in general, in the cold Arctic Ocean, temperature has little effect on density, which depends almost entirely on the salinity field here. A measure of density compensating variations in temperature and salinity (i.e. spiciness) is not appropriate (Timmermans and Jayne, 2016). However, it is stated in literature that as the Arctic Ocean warms up, temperature will take a new role in setting the dynamical balances. Under continued warming, there exists the possibility for a regime shift in the mechanisms by which heat is moved in the Arctic Ocean. This may result in a lid on the ocean heat, having implications for future predictions of Arctic sea ice (Timmermans and Jayne, 2016).

Our simulations with the convection model with a modified AW layer on the PHC3.0 benchmark initialization showed that warming of AW alone will not give a remarkable impact on the evolution of the sea ice cover ($\approx$ 10 cm decrease in final ice thickness due to 2 °C AW warming, Fig. 4.24). This is mainly because the convection does not reach into the AW layer until the end of the season, and no heat is transported through the strong stratification. Also, if the layer is heated and no salt is added to keep it vertically stable, the rise due to the density decrease is not enough to give an impact on the ice growth process (Fig. 4.24). This of course neglects many of the

processes discussed earlier. Nonetheless, the model shows that if the AW is shallower than 80 m, it starts to have a large influence on the ice growth process (Fig. 4.24). We have previously discussed shoaling of AW in three different contexts: seasonal shoaling, geographic shoaling and long term shoaling.

A seasonal shoaling is observed, and is explained by the fact that there is less sea ice growth during spring and non during summer, thus less convection, with a following thinner mixed layer. In summer there are also less storms that deepen the mixed layer and hence "push down" the upper AW interface. Geographic shoaling relative to the distance from the inflow of AW in Fram Strait has also been observed (Fig. 4.8). This is explained by the local processes such as cooling, sea ice growth, and sea ice melt that happen after the AW meets sea ice along its path northward. Shoaling of AW over time compared to climatologies has not been shown.

The model runs were repeated with different initial ice thicknesses (Fig. 4.25), which also shows that warming alone had little effect and shoaling of AW had a larger effect. With thick initial ice (> 1.2 m) there was no effect on the final ice thickness because of AW warming or shoaling. With a thinning sea ice cover in the Arctic, AW thus has become, and may become even more important in the future.

We conclude that the AW heat is able to substantially retard local ice formation, due to the heat brought up to the mixed layer by haline convection. This heat limits growth and can potentially also melt sea ice.

5.3.4 Bottom melting due to Atlantic Water influence

We have established that AW characteristics are partially controlled by topography, sea ice growth, sea ice melting, turbulent mixing, and the volume and characteristics of sea ice imported into the area. A global earth system model (NorESM) was used to investigate how changes in inflow AW characteristics influence the AW north of Svalbard. The model was used to investigate the existence of winter sea ice melting, indicated by the 1-D model. In the middle of the polar night in January-February, the atmospheric forcing does not support ice melt. The heat balance at the surface lacks a short wave component, air temperatures are negative, and the ocean loses heat. On the other hand, at this time, the inflowing AW reaches its highest temperatures of the seasonal cycle, and the warm pool sits closest to the ocean surface (Ivanov et al., 2009, 2012). Hence, if bottom melting is observed during this period it is likely because of AW heat.

First of all we investigated how well the NorESM model performs in our N-ICE2015 area by comparing several characteristics, such as the AW flow and spatial distribution of AW core temperature and depth, with N-ICE2015 and earlier observations. Of course the spatial resolution of the model is coarse, and limits comparison with observed profiles. However, looking at the whole region, the model performs well and captures many of the features we expect to see. The spatial distribution of AW core temperature has highest temperatures at the inflow and on the central and southern parts of the Plateau (Fig. 4.26). This is in accordance with the barotropic current pattern shown in

Figure 4.14. As expected, the AW is close to the surface when it enters the Arctic and it is deeper further along the flow path on the Plateau and the Basin. Due to the large grid cells it has been difficult to distinguish between Slope and Plateau in the model and we therefore just use Plateau and Basin.

There are many reasons why the model results are different from what we observe. Even though NorESM and the other CMIP5 models are run with similar initializations, they will after some time develop their own fluctuations and changes over time. Some more similar to what is observed in the real world than others. They also use different parametrizations, simplifications and approximations. Although many of the oceanic features we expect are captured in the model, it is still different from other models and reality. A comparison of the NorESM model with 15 other global ocean-sea ice models has been done in the framework of the Coordinated Ocean-ice Reference Experiments, phase II (CORE-II, Ilıcak et al. (2016)). Most of these models are the ocean+sea-ice components of the coupled climate models used in the Coupled Model Intercomparison Project Phase five (CMIP5) experiments. This study found a large spread in temperature in the Arctic Ocean between the models, and generally large differences compared to the observed temperature at intermediate depths (Ilıcak et al., 2016). Figure 5.4 shows a comparison of a temperature section through the Fram Strait and the Eurasian Basin from the NorESM model with the PHC3.0 climatology (Steele et al., 2001).

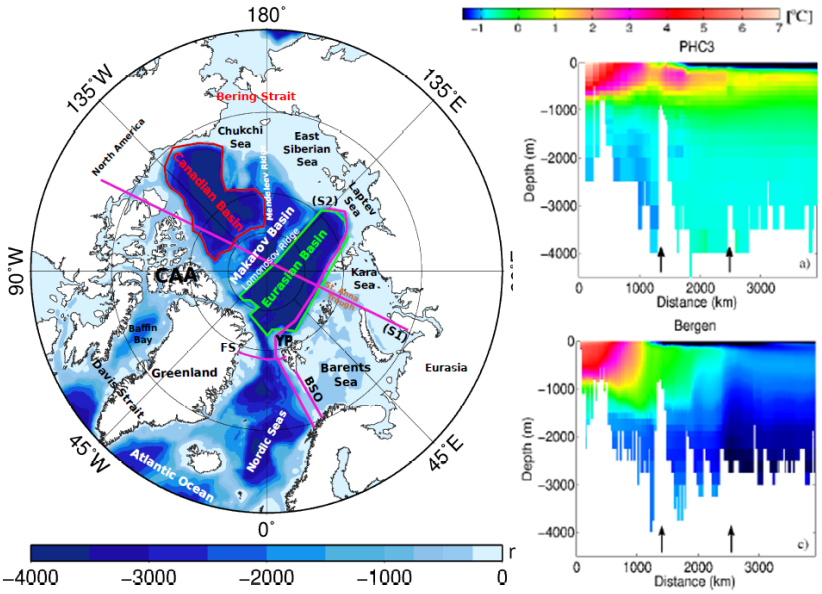

Figure 5.4: Map of the Arctic Ocean topography and a comparison of the NorESM model with a PHC3.0 climatology temperature section though S2 (pink line from the Fram Strait through the Eurasian Basin. The left arrow in the sections is the Yermak Plateau and the right arrow is the St. Anna Trough at the Barents Sea exit. Figures from Ilıcak et al. (2016).

There is a difference, and the difference is larger for some models than for others. The AW core appears to be warmer in the PHC3.0 further into the basin, and the mean modelled Eurasian basin is generally colder than the PHC3.0 climatology. The limitations of the PHC3.0 climatology (Chapter 3.2.5) have to be kept in mind as well. For this study, the main hydrography, AW characteristics and processes from NorESM are captured well enough for comparison with observations. The results are also good enough for a rough investigation on the existence of sea ice bottom melting during winter and how the AW characteristics north of Svalbard change with changes in inflowing AW characteristics.

Results from the NorESM analysis support our hypothesis that AW characteristics such as the core temperature in the N-ICE2015 area co-vary with the core temperature in the inflow area in the Fram Strait. The AW depth in the N-ICE2015 area appears not to be affected much by changes in inflowing AW characteristics, mostly because the AW is at the surface when it enters the Arctic Ocean, and the temperature differences do not have a large effect on the AW depth. Again the model's vertical resolution is not good enough for a direct comparison with observations.

The model does capture bottom melting during summer across the whole Arctic Ocean (Fig. 4.30 and 4.31). It also shows that during winter (February) there is extensive bottom melting in regions where the AW is close to the surface such as in the N-ICE2015 area (Fig. 4.30). This bottom melting correlates highly with changes in AW core temperature in the Fram Strait. In the Basin in the N-ICE2015 area, the observations show the at bottom melting only occurs during spring and summer and not during winter. The winter bottom melting appears to be confined to regions where the AW is high up in the water column, as it is on the Plateau, and it is also highly correlated with changes in AW inflow characteristics in the eastern Fram Strait (Fig. 4.32). Positive correlations, indicated by red and yellow areas in this figure, reflect that temperature anomalies in the Fram Strait co-vary with more melting in these areas.

Chapter 6

Summary and Outlook

The objective of this study was to investigate the hydrographic situation north of Svalbard during the N-ICE2015 campaign, and to study what governs Atlantic Water characteristics in the region and how they have changed over time. Further, the aim was to understand how Atlantic Water may influence the sea ice growth and melt.

The N-ICE2015 observations provide several opportunities for further investigation. Linking Atlantic Water to sea ice involves many different processes, and to get a better understanding of the "big picture" one would have to go more in depth in the different processes at hand, some of which, we only touched upon in this study. For example the effect of: internal tidal waves, double diffusive mixing, sea floor roughness, mixed layer evolution, increased freshwater circulation, increased stratification, ice-ocean shear, and wind on a thinner ice cover, are some examples of processes that would be interesting to investigate further to improve our understanding. A more detailed comparison and study of regional historical data would also provide a better understanding of the regional hydrographic changes over time.

We have presented the hydrography, analysed one dimensional model results, and studied the outcome from a fully coupled earth system model. This work has resulted in the following contributions:

- The most realistic long term climatological mean of the hydrography in the region north of Svalbard lies somewhere in between the PHC3.0 and the World Ocean Atlas (2013) climatologies. N-ICE2015 contributes significantly to the historical data sets because of the sparse previous winter observations in the region.
- Observations and model results show a warming trend of Atlantic Water core temperature over the last few decades. This is true both in the Atlantic Water inflow area and the N-ICE2015 area north of Svalbard. The warming trend of Atlantic Water in the Arctic Ocean may be part of long term multi-decadal variability where the warming observed is part of a warm phase. We can neither confirm nor invalidate this long term variability with the data that is currently

available, but temperatures have been almost as warm earlier in the 1930s. This warming trend over the past few decades have likely been enhanced or influenced by anthropogenic forcing. Simulations suggest that approximately 30 % of trend may be attributed to global warming.

- Both observations from N-ICE2015 and historical data show seasonality in Atlantic Water and Polar Surface Water north of Svalbard. The hydrography can clearly be divided into two regimes: winter observations with a deep salty mixed layer, and spring observations with a shallower and fresher surface mixed layer. During spring and summer the Atlantic Water is warmer than in winter. Due to the mixed layer depth deepening, the upper interface of the Atlantic Water is also deeper during winter.

- Atlantic Water characteristics north of Svalbard are mainly controlled by the distance along the inflow path rather than by topography itself, and by changes in inflowing Atlantic Water temperature in the Fram Strait. Atlantic Water characteristics north of Svalbard are also largely affected by local processes such as sea ice growth, melting and tidal induced mixing.

- The tidal signal north of Svalbard is generally low, but larger around the Yermak Plateau. Here the AOTIM5 inverse tidal model captures the correct frequencies, but underestimates the amplitude of the diurnal tidal signals when compared with observations. The observed oscillations in currents are possibly a combination of tidal and inertial oscillations, and these likely contribute to vertical mixing on the Yermak Plateau.

- The upper ocean flow is near barotropic, and shear is present in the uppermost layer, where a "more mobile" wind driven ice cover floats on a rather "steady" ocean. While a thin part of the mixed layer may follow the ice, most of the mixed layer follows the Atlantic Water flow pattern and oscillations.

- Atlantic Water has a direct impact on the sea ice cover north of Svalbard. Shallow and warm Atlantic Water efficiently reduces sea ice growth and can result in bottom melting throughout the whole year. Model studies confirm the existence of winter sea ice bottom melting north of Svalbard. This simulated bottom melting is confined to regions where Atlantic Water is close to the surface, such as on the Yermak Plateau. The bottom melting highly correlates with changes in Atlantic Water characteristics at the inflow.

- Stratification in the Arctic Ocean efficiently separates Atlantic Water heat from the layers above once the Atlantic Water is well inside the Basin. However, turbulent mixing due to wind forcing, tidal mixing and haline convection due to ice growth can still mix heat upwards through this stratification. Wind forcing also increases the ice-ocean shear, upper ocean current strength, turbulent mixing and the vertical heat fluxes.

- Observations show seasonal shoaling of the Atlantic Water upper interface in spring and summer, and shoaling of Atlantic Water upstream along the flow path. Observations and model results show that the upper interface of the Atlantic Water in the Nansen Basin has shoaled over time compared to the pre 1990 historical data. However, compared to more recent observations no further shoaling in the Nansen Basin is observed. On the Slope and the Yermak Plateau the upper interface of the Atlantic Water has not shoaled for neither climatologies.

- Thicker sea ice is less effected by Atlantic Water than thin sea ice. With a thinning Arctic sea ice cover in general there will likely be more sea ice growth during winter and therefore more haline convection. This leads to a deepening of the Mixed layer and upper interface of the Atlantic Water.

Our hypothesis stated:
"AW characteristics north of Svalbard are partly controlled by local topography of the Yermak Plateau, partly by local processes, and by the characteristics of the inflowing AW through Fram Strait. " This we have shown is correct, but more precisely we have shown that the characteristics are mainly controlled by the distance along the inflow path rather than by topography itself. Furthermore, our hypothesis stated:
"AW at the inflow on the Yermak Plateau is becoming warmer, and further along its path north of Svalbard it is shoaling. The warming and shoaling of AW melts and limits sea ice growth in the area. " We have successfully shown that the AW is warming, and that warming and shoaling of AW melts and limits sea ice growth. However, observations show no shoaling of the AW over time on the Slope and Plateau. Observations from after 1998 show no shoaling of AW in the Basin either. Based on our analysis we therefore falsify this part of our hypothesis.

These findings are important for our understanding of the evolution of the sea ice cover north of Svalbard and the influence of Atlantic Water. With warming Atlantic Water and a thinning sea ice cover in general we expect a closer link between Atlantic Water and the sea ice north of Svalbard in the future.

Bibliography

Aagaard, K. (1981). On the deep circulation in the Arctic Ocean. *Deep Sea Research Part A. Oceanographic Research*, 28(3):251–268.

Aagaard, K., Coachman, L. K., and Carmack, E. (1981). On the halocline of the Arctic Ocean. *Deep Sea Research Part A, Oceanographic Research Papers*, 28(6):529–545.

Aagaard, K. and Greisman, P. (1975). Toward new mass and heat budgets for the Arctic Ocean. *Journal of Geophysical Research*, 80(27):3821–3827.

Aagaard, K., Swift, J. H., and Carmack, E. C. (1985). Thermohaline circulation in the Arctic Mediterranean Seas. *Journal of Geophysical Research: Oceans*, 90(C3):4833–4846.

Aagard and E.C. Carmack, K., Aagard, K., and E.C.Carmack (1989). The role of sea ice and other fresh water in the Arctic circulation. *Journal of Geophysical Research*, 94(1):414–485.

Aasen, I. L. (2009). Hydrographic conditions in the upper Arctic Ocean from 1950 until 2009. *Master's Thesis: University of Bergen*, (June).

Alexeev, V. a., Ivanov, V. V., Kwok, R., and Smedsrud, L. H. (2013). North Atlantic warming and declining volume of arctic sea ice. *The Cryosphere Discussions*, 7(1):245–265.

Amstrup, S. C., Deweaver, E. T., Douglas, D. C., Marcot, B. G., Durner, G. M., Bitz, C. M., and Bailey, D. a. (2010). Greenhouse gas mitigation can reduce sea-ice loss and increase polar bear persistence. *Nature*, 468(7326):955–958.

Anderson, L. G., Bjrrk, G., Jones, E. P., Kattner, G., Koltermann, K. P., Liljeblad, B., Lindegren, R., Rudels, B., and Swift, J. (1994). Water masses and circulation in the Eurasian Basin: Results from the Oden 91 expedition. *Journal of Geophysical Research: Oceans*, 99(C2):3273–3283.

Antonov, J. I., Levitus, S., Boyer, T. P., Conkright, M. E., O'Brien, T. D., and Stephens, C. (1998). World Ocean Atlas 1998. Vol. 1: Temperature of the Atlantic Ocean.

Årthun, M., Ingvaldsen, R., Smedsrud, L., and Schrum, C. (2011). Dense water formation and circulation in the Barents Sea. *Deep Sea Research Part I: Oceanographic Research Papers*, 58(8):801–817.

Ball, F. K. (1960). Control of inversion height by surface heating. *Quarterly Journal of the Royal Meteorological Society*, 86(370):483–494.

Banks, H. T., Wood, R. A., Gregory, J. M., Johns, T. C., and Jones, G. S. (2000). Are observed decadal changes in intermediate water masses a signature of anthropogenic climate change? *Geophysical Research Letters*, 27(18):2961–2964.

Barnes, E. A. (2013). Revisiting the evidence linking Arctic amplification to extreme weather in midlatitudes. *Geophysical Research Letters*, 40(17):4734–4739.

Barnett, T. P., Pierce, D. W., AchutaRao, K. M., Gleckler, P. J., Santer, B. D., Gregory, J. M., and Washington, W. M. (2005). Penetration of Human-Induced Warming into the World's Oceans. *Science*, 309(5732):284–287.

Barnett, T. P., Pierce, D. W., and Schnur, R. (2001). Detection of Anthropogenic Climate Change in the World's Oceans. *Science*, 292(5515):270–274.

Bekryaev, R. V., Polyakov, I. V., and Alexeev, V. a. (2010). Role of Polar Amplification in Long-Term Surface Air Temperature Variations and Modern Arctic Warming. *Journal of Climate*, 23(14):3888–3906.

Bentsen, M., Bethke, I., Debernard, J. B., Iversen, T., Kirkevåg, a., Seland, Ø., Drange, H., Roelandt, C., Seierstad, I. a., Hoose, C., and Kristjánsson, J. E. (2013). The Norwegian Earth System Model, NorESM1-M – Part 1: Description and basic evaluation of the physical climate. *Geoscientific Model Development*, 6(3):687–720.

Beszczynska-Möller, A. and Stephen R. Dye (2006). ICES Report on Ocean Climate 2005. *Cooperative Research Report*, (280):53.

Bhatt, U. S., Walker, D. A., Walsh, J. E., Carmack, E. C., Frey, K. E., Meier, W. N., Moore, S. E., Parmentier, F.-J. W., Post, E., and Romanovsky, V. E. (2014). Implications of Arctic sea ice decline for the Earth system. *Annual Review of Environment and Resources*, 39:57–89.

Bluhm, B. A., Kosobokova, K. N., and Carmack, E. C. (2015). A tale of two basins: An integrated physical and biological perspective of the deep Arctic Ocean. *Progress in Oceanography*, 139:89–121.

Bourgain, P. and Gascard, J. C. (2012). The Atlantic and summer Pacific waters variability in the Arctic Ocean from 1997 to 2008. *Geophysical Research Letters*, 39(5).

Boyd, T. and Steele, M. (2002). Partial recovery of the Arctic Ocean halocline. *Geophysical Research Letters*, 29(14):94–97.

Bukreev, V. I. (2007). Double diffusion during ice thawing in salt water. *Izvestiya, Atmospheric and Oceanic Physics*, 43(6):762–765.

Carmack, E., Polyakov, I., Padman, L., Fer, I., Hunke, E., Hutchings, J., Jackson, J., Kelley, D., Kwok, R., Layton, C., Melling, H., Perovich, D., Persson, O., Ruddick, B., Timmermans, M.-L., Toole, J., Ross, T., Vavrus, S., and Winsor, P. (2015). Towards Quantifying the Increasing Role of Oceanic Heat in Sea Ice Loss in the New Arctic. *Bulletin of the American Meteorological Society*, 96(12):2079–2105.

Carmack, E. C., Macdonald, R. W., Perkin, R. G., McLaughlin, F. A., and Pearson, R. J. (1995). Evidence for warming of Atlantic water in the southern Canadian Basin of the Arctic Ocean, Results from the Larsen 93 expedition. *Geophysical Research Letters*, 22(9):1061–1064.

Collett, R. and Nansen, F. (1901). The Norwegian North Polar Expedition 1893-1896. *Volume II. Christiania.*

Comiso, J. C. (2012). Large Decadal Decline of the Arctic Multiyear Ice Cover. *Journal of Climate*, 25(4):1176–1193.

Curry, J. A., Schramm, J. L., and Ebert, E. E. (1995). Sea ice-albedo climate feedback mechanism. *Journal of Climate*, 8(2):240–247.

Cushman-Roisin, B. and Beckers, J.-M. (2011). *Introduction to geophysical fluid dynamics: physical and numerical aspects*, volume 101. Academic Press.

Darelius, E. and Nilsen, F. (2004). Ice formation and covection - a one dimensional model (Model Manual). Technical report, UNIS, University Center of Svalbard.

Dmitrenko, I. a., Polyakov, I. V., Kirillov, S. a., Timokhov, L. a., Frolov, I. E., Sokolov, V. T., Simmons, H. L., Ivanov, V. V., and Walsh, D. (2008). Toward a warmer Arctic Ocean: Spreading of the early 21st century Atlantic Water warm anomaly along the Eurasian Basin margins. *Journal of Geophysical Research*, 113(C5).

Dmitrenko, I. a., Polyakov, I. V., Kirillov, S. a., Timokhov, L. a., Simmons, H. L., Ivanov, V. V., and Walsh, D. (2006). Seasonal variability of Atlantic water on the continental slope of the Laptev Sea during 2002–2004. *Earth and Planetary Science Letters*, 244(3-4):735–743.

Dulvy, N. K., Rogers, S. I., Jennings, S., Stelzenmüller, V., Dye, S. R., and Skjoldal, H. R. (2008). Climate change and deepening of the North Sea fish assemblage: a biotic indicator of warming seas. *Journal of Applied Ecology*, 45(4):1029–1039.

Echert, D. C., Morison, J. H., White, G. B., and Geller, E. W. (1989). The autonomous ocean profiler: A current-driven oceanographic sensor platform. *Oceanic Engineering, IEEE Journal of*, 14(2):195–202.

Eicken, H. (2003). From the microscopic, to the macroscopic, to the regional scale: growth, microstructure and properties of sea ice. *Sea ice: an introduction to its physics, chemistry, biology and geology*, pages 22–81.

Fahrbach, E., Meincke, J., Østerhus, S., Rohardt, G., Schauer, U., Tverberg, V., and Verduin, J. (2001). Direct measurements of volume transports through Fram Strait. *Polar Research*, 20(2):217–224.

Fer, I., Müller, M., and Peterson, A. (2015). Tidal forcing, energetics, and mixing near the Yermak Plateau. *Ocean Science*, 11(2):287–304.

Fer, I., Skogseth, R., and Geyer, F. (2010). Internal Waves and Mixing in the Marginal Ice Zone near the Yermak Plateau. *Journal of Physical Oceanography*, 40(7):1613–1630.

Fofonoff, N. P. (1985). Physical properties of seawater: A new salinity scale and equation of state for seawater. *Journal of Geophysical Research: Oceans (1978–2012)*, 90(C2):3332–3342.

Francis, J. A. and Vavrus, S. J. (2012). Evidence linking Arctic amplification to extreme weather in mid latitudes. *Geophysical Research Letters*, 39(6).

Furevik, T., Bentsen, M., Drange, H., Kindem, I. K. T., Kvamstø, N. G., and Sorteberg, A. (2003). Description and evaluation of the Bergen climate model: ARPEGE coupled with MICOM. *Climate Dynamics*, 21(1):27–51.

Gade, H. (1994). Termodynamiske Prosesser i havet - Utvalgte temaer over processer och energiomsetning på makro og mesoskala, del 2. Technical report, University of Bergen, Geophysical Institute. (In Norwegian).

Gade, H. G. (1979). Melting of ice in sea water: A primitive model with application to the Antarctic ice shelf and icebergs. *Journal of Physical Oceanography*, 9(1):189–198.

Gade, H. G. (1993). When ice melts in sea water: A review. *Atmosphere Ocean*, 31(1):139–165.

Garrett, C. and Kunze, E. (2007). Internal tide generation in the deep ocean. *Annu. Rev. Fluid Mech.*, 39:57–87.

Gascard, J.-C., Festy, J., Le Gogg, H., Weber, M., Bruemmer, B., Offermann, M., Doble, M., Wadhams, P., Forsberg, R., and Hanson, S. (2008). Exploring Arctic transpolar drift during dramatic sea ice retreat. *Eos*, 89(3):21–28.

Gent, P. R., Danabasoglu, G., Donner, L. J., Holland, M. M., Hunke, E. C., Jayne, S. R., Lawrence, D. M., Neale, R. B., Rasch, P. J., Vertenstein, M., Worley, P. H., Yang, Z.-L., and Zhang, M. (2011). The Community Climate System Model Version 4. *Journal of Climate*, 24(19):4973–4991.

Gimbert, F., Marsan, D., Weiss, J., Jourdain, N. C., and Barnier, B. (2012). Sea ice inertial oscillations in the Arctic Basin. *The Cryosphere*, 6:1187–1201.

Granskog, M. A., Assmy, P., Gerland, S., Spreen, G., Steen, H., and Smedsrud, L. (2016). Arctic research on thin ice: Consequences of Arctic sea ice loss. *EOS*, 97.

Grassi, B., Redaelli, G., and Visconti, G. (2013). Arctic Sea Ice Reduction and Extreme Climate Events over the Mediterranean Region. *Journal of Climate*, 26(24).

Haas, C., Hendricks, S., Eicken, H., and Herber, A. (2010). Synoptic airborne thickness surveys reveal state of Arctic sea ice cover. *Geophysical Research Letters*, 37(9).

Halvorsen, M. H., Smedsrud, L. H., Zhang, R., and Kloster, K. (2015). Fram Strait spring ice export and September Arctic sea ice. *The Cryosphere Discussions*, 9(4):4205–4235.

Hinze, J. O. (1975). *Turbulence, Second Edition.* McGraw-Hill, New York, 2 edition.

Hogg, R. V., Tanis, E. A., and Zimmerman, D. L. (2010). *Probabiblity and Statistical Inference 8/e.* Pearson Prentice Hall, New Jersey, 8/e edition.

Holliday, N. P., Hughes, S. L., Bacon, S., Beszczynska-Möller, A., Hansen, B., Lavín, A., Loeng, H., Mork, K. a., Østerhus, S., Sherwin, T., and Walczowski, W. (2008). Reversal of the 1960s to 1990s freshening trend in the northeast North Atlantic and Nordic Seas. *Geophysical Research Letters*, 35(3).

Honda, M., Yamazaki, K., Tachibana, Y., and Takeuchi, K. (1996). Influence of Okhotsk se ice extent on atmospheric circulation. 23(24):3595–3598.

Hunkins, K. L. (1974). Subsurface eddies in the Arctic ocean. *Deep-Sea Research and Oceanographic Abstracts*, 21(12):1017–1033.

Ilıcak, M., Drange, H., Wang, Q., Gerdes, R., Aksenov, Y., Bailey, D., Bentsen, M., Biastoch, A., Bozec, A., and Böning, C. (2016). An assessment of the Arctic Ocean in a suite of interannual CORE-II simulations. Part III: Hydrography and fluxes. *Ocean Modelling*, 100:141–161.

Ivanov, V., Alexeev, V., Koldunov, N. V., Repina, I., Sando, A. B., Smedsrud, L. H., and Smirnov, A. (2016). Arctic Ocean heat impact on regional ice decay - a suggested positive feedback. *Journal of Physical Oceanography*, 46(5):1437–1456.

Ivanov, V. and Watanabe, E. (2013). Does Arctic sea ice reduction foster shelf-basin exchange? *Ecological Applications*, 23(8):1765–1777.

Ivanov, V. V., Alexeev, V. A., Repina, I., Koldunov, N. V., and Smirnov, A. (2012). Tracing Atlantic Water signature in the Arctic sea ice cover east of Svalbard. *Advances in*

Meteorology, 2012.

Ivanov, V. V., Polyakov, I. V., Dmitrenko, I. a., Hansen, E., Repina, I. a., Kirillov, S. a., Mauritzen, C., Simmons, H., and Timokhov, L. a. (2009). Seasonal variability in Atlantic Water off Spitsbergen. *Deep Sea Research Part I: Oceanographic Research Papers*, 56(1):1–14.

Ivanova, N., Johannessen, O. M., Pedersen, L. T., and Tonboe, R. T. (2014). Retrieval of Arctic sea ice parameters by satellite passive microwave sensors: A comparison of eleven sea ice concentration algorithms. *Geoscience and Remote Sensing, IEEE Transactions on*, 52(11):7233–7246.

Jackson, J. M., Carmack, E. C., McLaughlin, F. a., Allen, S. E., and Ingram, R. G. (2010). Identification, characterization, and change of the near-surface temperature maximum in the Canada Basin, 1993–2008. *Journal of Geophysical Research*, 115(C5).

Jakobsson, M. (2002). Hypsometry and volume of the Arctic Ocean and its constituent seas. *Geochemistry, Geophysics, Geosystems*, 3(5):1–18.

Jeffries, M. O., Overland, J. E., and Perovich, D. K. (2013). The Arctic shifts to a new normal. *Physics Today*, 66(10):35.

Jenkins, A. and Holland, D. (2007). Melting of floating ice and sea level rise. *Geophysical Research Letters*, 34(16):1–5.

Jones, E. P. (2001). Circulation in the Arctic Ocean. *Polar Research*, 20(2):139–146.

Karcher, M. J. (2003). Arctic warming: Evolution and spreading of the 1990s warm event in the Nordic seas and the Arctic Ocean. *Journal of Geophysical Research*, 108(C2):3034.

Kay, J. E., Holland, M. M., and Jahn, A. (2011). Inter-annual to multi-decadal Arctic sea ice extent trends in a warming world. *Geophysical Research Letters*, 38(15).

Kraus, E. B. and Turner, J. S. (1967). A one dimensional model of the seasonal thermocline nr 2. *Tellus*, 19(1):98–106.

Kwok, R., Cunningham, G. F., Wensnahan, M., Rigor, I., Zwally, H. J., and Yi, D. (2009). Thinning and volume loss of the Arctic Ocean sea ice cover: 2003–2008. *Journal of Geophysical Research: Oceans (1978–2012)*, 114(C7).

Kwok, R. and Morison, J. (2011). Dynamic topography of the ice-covered Arctic Ocean from ICESat. *Geophysical Research Letters*, 38(2).

Kwok, R. and Rothrock, D. a. (2009). Decline in Arctic sea ice thickness from submarine and ICESat records: 1958-2008. *Geophysical Research Letters*, 36(15).

Kwok, R., Schweiger, A., Rothrock, D. A., Pang, S., and Kottmeier, C. (1998). Sea ice motion from satellite passive microwave imagery assessed with ERS SAR and buoy motions. 103(97):8191–8214.

Kwok, R., Spreen, G., and Pang, S. (2013). Arctic sea ice circulation and drift speed: Decadal trends and ocean currents. *Journal of Geophysical Research: Oceans*, 118(5):2408–2425.

Langehaug, H. R., Geyer, F., Smedsrud, L. H., and Gao, Y. (2013). Arctic sea ice decline and ice export in the CMIP5 historical simulations. *Ocean Modelling*, 71:114–126.

Laxon, S. W., Giles, K. a., Ridout, A. L., Wingham, D. J., Willatt, R., Cullen, R., Kwok,

R., Schweiger, A., Zhang, J., Haas, C., Hendricks, S., Krishfield, R., Kurtz, N., Farrell, S., and Davidson, M. (2013). CryoSat-2 estimates of Arctic sea ice thickness and volume. *Geophysical Research Letters*, 40(4):732–737.

Lehner, F., Raible, C. C., Hofer, D., and Stocker, T. F. (2012). The freshwater balance of polar regions in transient simulations from 1500 to 2100 AD using a comprehensive coupled climate model. *Climate dynamics*, 39(1-2):347–363.

Lemke, P. and Manley, T. O. (1984). The seasonal variation of the mixed layer and the pycnocline under polar sea ice. *Journal of Geophysical Research*, 89(C4):6494.

Lenn, Y. D., Wiles, P. J., Torres-Valdes, S., Abrahamsen, E. P., Rippeth, T. P., Simpson, J. H., Bacon, S., Laxon, S. W., Polyakov, I., Ivanov, V., and Kirillov, S. (2009). Vertical mixing at intermediate depths in the Arctic boundary current. *Geophysical Research Letters*, 36(5).

Levitus, S., Antonov, J. I., Boyer, T. P., and Stephens, C. (2000). Warming of the world ocean. *Science*, 287(5461):2225–2229.

Lindsay, R. W. (2005). The Thinning of Arctic Sea Ice , 1988 – 2003 : Have We Passed a Tipping Point ? (1999):1988–2003.

Lindsay, R. W., Zhang, J., Schweiger, a., Steele, M., and Stern, H. (2009). Arctic Sea Ice Retreat in 2007 Follows Thinning Trend. *Journal of Climate*, 22(1):165–176.

Lique, C. and Steele, M. (2012). Where can we find a seasonal cycle of the Atlantic water temperature within the Arctic Basin? *Journal of Geophysical Research*, 117(C3).

Locarnini, R. A., Mishonov, A. V., Antonov, J. I., Boyer, T. P., Garcia, H. E., Baranova, O. K., Zweng, M. M., Paver, C. R., Reagan, J. R., and Johnson, D. R. (2013). World Ocean Atlas 2013. Vol. 1: Temperature. *A. Mishonov, Technical Ed. NOAA Atlas NESDIS*, 73:40.

Marshall, J. and Plumb, A. R. (2008). *Atmosphere, Ocean, and Climate Dynamics: An Introductory Text*. Elsevier Academic Press.

Maslanik, J. A., Fowler, C., Stroeve, J., Drobot, S., Zwally, J., Yi, D., and Emery, W. (2007). A younger, thinner Arctic ice cover: Increased potential for rapid, extensive sea ice loss. *Geophysical Research Letters*, 34(24).

Maykut, G. A. (1985). An Introduction to Ice in the Polar Oceans. Technical report, Washington University Seatle Applied Physics Lab.

Maykut, G. a. and McPhee, M. G. (1995). Solar heating of the Arctic mixed layer. *Journal of Geophysical Research*, 100(C12):24691.

Maykut, G. a. and Untersteiner, N. (1971). Some results from a time-dependent thermodynamic model of sea ice. *Journal of Geophysical Research*, 76(6):1550–1575.

McDougall, T., Feistel, R., Millero, F., Jackett, D., Wright, D., King, B. A., Marion, G. M., Chen, C. T. A., and Spitzer, P. (2010). The International Thermodynamic Equation Of Sea water 2010 (TEOS-10): Calculation and Use of Thermodynamic Properties, Global Ship-based Repeat Hydrography Manual. *IOCCP Report*.

McDougall, T. J. (2003). Potential Enthalpy: A Conservative Oceanic Variable for Evaluating Heat Content and Heat Fluxes. pages 945–963.

McDougall, T. J. and Barker, P. M. (2011). *Getting started with TEOS-10 and the Gibbs Seawater (GSW) Oceanographic Toolbox*. SCOR/IAPSO.

McLaughlin, F., Carmack, E., Macdonald, R., Melling, H., Swift, J., Wheeler, P., Sherr, B., and Sherr, E. (2004). The joint roles of Pacific and Atlantic-origin waters in the Canada Basin, 1997–1998. *Deep Sea Research Part I: Oceanographic Research Papers*, 51(1):107–128.

McLaughlin, F. a., Carmack, E. C., Williams, W. J., Zimmermann, S., Shimada, K., and Itoh, M. (2009). Joint effects of boundary currents and thermohaline intrusions on the warming of Atlantic water in the Canada Basin, 1993–2007. *Journal of Geophysical Research*, 114.

McPhee, M. G. (2002). Turbulent stress at the ice/ocean interface and bottom surface hydraulic roughness during the SHEBA drift. *Journal of Geophysical Research: Oceans (1978–2012)*, 107(C10).

McPhee, M. G. (2003). Ocean-to-ice heat flux at the North Pole environmental observatory. *Geophysical Research Letters*, 30(24):2274.

McPhee, M. G., Morison, J. H., and Nilsen, F. (2008). Revisiting heat and salt exchange at the ice ocean interface: Ocean flux and modeling considerations. *Journal of Geophysical Research: Oceans (1978–2012)*, 113(C6).

Melling, H. and Moore, R. M. (1995). Modification of halocline source waters during freezing on the Beaufort Sea shelf: evidence from oxygen isotopes and dissolved nutrients. *Continental Shelf Research*, 15(1):89–113.

Mori, M., Watanabe, M., Shiogama, H., Inoue, J., and Kimoto, M. (2014). Robust Arctic sea-ice influence on the frequent Eurasian cold winters in past decades. *Nature Geoscience*, 7(12):869–873.

Mosby, H. (1962). Water, salt and heat balance of the North Polar Sea and of the Norwegian Sea. *Geophys. Norv*, 24(11):289–313.

Nansen, F. (1898). *"Farthest north" : being the record of a voyage of exploration of the ship Fram 1893-96 and of a fifteen months' sleigh journey by Dr. Nansen and Lieut. Johansen.* George Newnes, London.

Nansen, F. (1902). *The oceanography of the north polar basin*, volume 3. Longmans, Green, and Company.

Nansen, F. (1906). *Northern waters: Captain Roald Amundsen's oceanographic observations in the Arctic Seas in 1901. With a discussion of the origin of the Bottom-Waters of the Northern Seas.* Number 3. In commission by Jacob Dybwad.

National Snow and Ice Data Centre (2015). Arctic Sea Ice News and Analysis: 2015 melt season in review. http://nsidc.org/arcticseaicenews/. Last accessed on May. 1st, 2016.

Nilsen, J. E. Ø. and Falck, E. (2006). Variations of mixed layer properties in the Norwegian Sea for the period 1948–1999. *Progress in Oceanography*, 70(1):58–90.

NSIDC (2013). Arctic Sea Ice News and Analysis, Arctic Sea Ice Age. http://nsidc.org/arcticseaicenews/tag/multiyear-ice/. Last accessed on May. 1st, 2016.

Nummelin, A., Li, C., and Smedsrud, L. H. (2015). Response of Arctic Ocean stratification to changing river runoff in a column model. *Journal of Geophysical Research: Oceans*, 120(4):2655–2675.

Nummelin, A., Licak, M., Li, C., and Smedsrud, L. H. (2016). Consequences of Future

Increased Arctic Runoff on Arctic Ocean Stratification, Circulation, and Sea Ice Cover. *Submitted to Journal of Geophysical Research*, 120:617–637.

Onarheim, I. H., Smedsrud, L. H., Ingvaldsen, R. B., and Nilsen, F. (2014). Loss of sea ice during winter north of Svalbard. *Tellus A*, 66(1):1–9.

Otteraa, O. H., Bentsen, M., Bethke, I., and Kvamstø, N. G. (2009). Simulated pre-industrial climate in Bergen Climate Model (version 2): model description and large-scale circulation features. *Geoscientific Model Development*, 2(2):197–212.

Padman, L. and Dillon, T. M. (1987). Vertical heat fluxes through the Beaufort Sea thermohaline staircase. *Journal of Geophysical Research*, 92(C10):10799.

Padman, L. and Dillon, T. M. (1991). Turbulent mixing near the Yermak Plateau during the coordinated Eastern Arctic Experiment. *Journal of Geophysical Research: Oceans*, 96(C3):4769–4782.

Padman, L. and Erofeeva, S. (2004). A barotropic inverse tidal model for the Arctic Ocean. *Geophysical Research Letters*, 31(2).

Parkinson, C. L. and Comiso, J. C. (2013). On the 2012 record low Arctic sea ice cover: Combined impact of preconditioning and an August storm. *Geophysical Research Letters*, 40(7):1356–1361.

Parry, M. L. (2007). *Climate change 2007-impacts, adaptation and vulnerability: Working group II contribution to the fourth assessment report of the IPCC*, volume 4. Cambridge University Press.

Perovich, D. K., Grenfell, T. C., Light, B., Richter-Menge, J. A., Sturm, M., Tucker III, W. B., Eicken, H., Maykut, G. A., and Elder, B. (1999). SHEBA: Snow and Ice Studies. *US Army Cold Reg. Res. and Eng. Lab.*

Perovich, D. K., Light, B., Eicken, H., Jones, K. F., Runciman, K., and Nghiem, S. V. (2007). Increasing solar heating of the Arctic Ocean and adjacent seas, 1979–2005: Attribution and role in the ice-albedo feedback. *Geophysical Research Letters*, 34(19).

Perovich, D. K., Richter-Menge, J. a., Jones, K. F., and Light, B. (2008). Sunlight, water, and ice: Extreme Arctic sea ice melt during the summer of 2007. *Geophysical Research Letters*, 35(11).

Persson, P. O. G. (2011). Onset and end of the summer melt season over sea ice: thermal structure and surface energy perspective from SHEBA. *Climate Dynamics*, 39(6):1349–1371.

Peterson, A. K. (2017). Observations of Under-Ice Heat and Moentum Fluxes from Drift Stations North of Svalbard. *In progress.*

Pickart, R. S. and Clarke, R. A. (2002). Hydrography of the Labrador Sea during Active Convection. *Journal of Physical Oceanography*, pages 428–457.

Piechura, J. and Walczowski, W. (2009). Warming of the West Spitsbergen Current and sea ice north of Svalbard. *Oceanologia*, 51(2):147–164.

Pnyushkov, A. V., Polyakov, I. V., Ivanov, V. V., Aksenov, Y., Coward, A. C., Janout, M., and Rabe, B. (2015). Structure and variability of the boundary current in the Eurasian Basin of the Arctic Ocean. *Deep Sea Research Part I: Oceanographic Research Papers*, 101:80–97.

Polyakov, I. V. (2005). One more step toward a warmer Arctic. *Geophysical Research Letters*, 32(17):L17605.

Polyakov, I. V., Alekseev, G. V., Timokhov, L. a., Bhatt, U. S., Colony, R. L., Simmons, H. L., Walsh, D., Walsh, J. E., and Zakharov, V. F. (2004). Variability of the Intermediate Atlantic Water of the Arctic Ocean over the Last 100 Years. *Journal of Climate*, 17(23):4485–4497.

Polyakov, I. V., Alexeev, V. a., Bhatt, U. S., Polyakova, E. I., and Zhang, X. (2009). North Atlantic warming: patterns of long-term trend and multidecadal variability. *Climate Dynamics*, 34(2-3):439–457.

Polyakov, I. V., Pnyushkov, A. V., Rember, R., Padman, L., Carmack, E. C., and Jackson, J. M. (2013). Winter Convection Transports Atlantic Water Heat to the Surface Layer in the Eastern Arctic Ocean. *Journal of Physical Oceanography*, 43(10):2142–2155.

Polyakov, I. V., Pnyushkov, A. V., and Timokhov, L. a. (2012). Warming of the Intermediate Atlantic Water of the Arctic Ocean in the 2000s. *Journal of Climate*, 25(23):8362–8370.

Polyakov, I. V., Timokhov, L. a., Alexeev, V. a., Bacon, S., Dmitrenko, I. a., Fortier, L., Frolov, I. E., Gascard, J.-C., Hansen, E., Ivanov, V. V., Laxon, S., Mauritzen, C., Perovich, D., Shimada, K., Simmons, H. L., Sokolov, V. T., Steele, M., and Toole, J. (2010). Arctic Ocean Warming Contributes to Reduced Polar Ice Cap. *Journal of Physical Oceanography*, 40(12):2743–2756.

Rainville, L. and Winsor, P. (2008). Mixing across the Arctic Ocean: Microstructure observations during the Beringia 2005 Expedition. *Geophysical Research Letters*, 35(8):L08606.

Rainville, L. and Woodgate, R. a. (2009). Observations of internal wave generation in the seasonally ice-free Arctic. *Geophysical Research Letters*, 36(23).

Rampal, P., Weiss, J., and Marsan, D. (2009). Positive trend in the mean speed and deformation rate of Arctic sea ice, 1979–2007. *Journal of Geophysical Research*, 114(C5):C05013.

Rigor, I. G., Colony, R. L., and Martin, S. (2000). Variations in Surface Air Temperature Observations in the Arctic, 1979–97. *Journal of Climate*, 13(5):896–914.

Rippeth, T. P., Lincoln, B. J., Lenn, Y.-D., Green, J. a. M., Sundfjord, A., and Bacon, S. (2015). Tide-mediated warming of Arctic halocline by Atlantic heat fluxes over rough topography. *Nature Geoscience*, 8(3):191–194.

Rothrock, D. a., Percival, D. B., and Wensnahan, M. (2008). The decline in arctic sea-ice thickness: Separating the spatial, annual, and interannual variability in a quarter century of submarine data. *Journal of Geophysical Research*, 113(C5).

Ruddick, B. and Gargett, A. E. (2003). Oceanic double-infusion: introduction. *Progress in Oceanography*, 56(3-4):381–393.

Ruddick, B. and Kerr, O. (2003). Oceanic thermohaline intrusions: theory. *Progress in Oceanography*, 56(3-4):483–497.

Rudels (1991). Convection and deep water formation in the Arctic Ocean-Greenland Sea System. *Journal of Marine Systems*, 2(1991):435–450.

Rudels, B. (2015). Arctic Ocean circulation, processes and water masses: A description of observations and ideas with focus on the period prior to the International Polar Year 2007–2009. *Progress in Oceanography*, 132:22–67.

Rudels, B., Anderson, L. G., and Jones, E. P. (1996). Formation and evolution of the surface mixed layer and halocline of the Arctic Ocean. *Journal of Geophysical Research: Oceans*, 101:8807–8821.

Rudels, B., Björk, G., Muench, R. D., and Schauer, U. (1999a). Double-diffusive layering in the Eurasian Basin of the Arctic Ocean. *Journal of Marine Systems*, 21(1-4):3–27.

Rudels, B., Friedrich, H. J., Hainbucher, D., and Lohmann, G. (1999b). On the parameterisation of oceanic sensible heat loss to the atmosphere and to ice in an ice-covered mixed layer in winter. *Deep Sea Research Part II: Topical Studies in Oceanography*, 46(6):1385–1425.

Rudels, B., Korhonen, M., Schauer, U., Pisarev, S., Rabe, B., and Wisotzki, A. (2015). Circulation and transformation of Atlantic water in the Eurasian Basin and the contribution of the Fram Strait inflow branch to the Arctic Ocean heat budget. *Progress in Oceanography*, 132:128–152.

Rudels, B., Meyer, R., Fahrbach, E., Ivanov, V. V., Østerhus, S., Quadfasel, D., Schauer, U., Tverberg, V., and Woodgate, R. A. (2000). Water mass distribution in Fram Strait and over the Yermak Plateau in summer 1997. *Annales Geophysicae*, 18(6):687–705.

Sandø, A., Gao, Y., and Langehaug, H. R. (2014). Poleward ocean heat transport, sea ice processes, and Arctic sea ice variability in NorESM1-M simulations. *Journal of Geophysical Research: Oceans*, pages 2095–2108.

Schauer, U. (2004). Arctic warming through the Fram Strait: Oceanic heat transport from 3 years of measurements. *Journal of Geophysical Research*, 109.

Schauer, U. and Beszczynska-Möller, A. (2009). Problems with estimation and interpretation of oceanic heat transport–conceptual remarks for the case of Fram Strait in the Arctic Ocean. *Ocean Science*, 5(4):487–494.

Schauer, U., Loeng, H., Rudels, B., Ozhigin, V. K., and Dieck, W. (2002). Atlantic Water flow through the Barents and Kara Seas. *Deep Sea Research Part I: Oceanographic Research Papers*, 49(12):2281–2298.

Schauer, U., Muench, R. D., Rudels, B., and Timokhov, L. (1997). Impact of eastern Arctic shelf waters on the Nansen Basin intermediate layers. *Journal of Geophysical Research*, 102:3371–3382.

Schmitt, R. (1994). Double diffusion in oceanography. *Annual Review of Fluid Mechanics*.

Schweiger, A., Lindsay, R., Zhang, J., Steele, M., Stern, H., and Kwok, R. (2011). Uncertainty in modeled Arctic sea ice volume. *Journal of Geophysical Research*, 116.

Screen, J. a., Simmonds, I., Deser, C., and Tomas, R. (2013). The Atmospheric Response to Three Decades of Observed Arctic Sea Ice Loss. *Journal of Climate*, 26(4):1230–1248.

Seland, O., Iversen, T., Kirkevaag, A., and Storelvmo, T. (2008). Aerosol climate interactions in the CAM Oslo atmospheric GCM and investigation of associated basic shortcomings. *Tellus A*, 60(3):459–491.

Serreze, M. C., Barrett, A. P., Slater, A. G., Woodgate, R. a., Aagaard, K., Lammers, R. B., Steele, M., Moritz, R., Meredith, M., and Lee, C. M. (2006). The large-scale freshwater cycle of the Arctic. *Journal of Geophysical Research*, 111(C11).

Shaw, W. J., Stanton, T. P., McPhee, M. G., Morison, J. H., and Martinson, D. G. (2009). Role of the upper ocean in the energy budget of Arctic sea ice during SHEBA. *Journal of*

Geophysical Research, 114(C6):C06012.

Shimada, K. (2004). Penetration of the 1990s warm temperature anomaly of Atlantic Water in the Canada Basin. *Geophysical Research Letters*, 31(20).

Shimada, K. (2005). Halocline structure in the Canada Basin of the Arctic Ocean. *Geophysical Research Letters*, 32(3).

Shimada, K., Kamoshida, T., Itoh, M., Nishino, S., Carmack, E., McLaughlin, F., Zimmermann, S., and Proshutinsky, A. (2006). Pacific Ocean inflow: Influence on catastrophic reduction of sea ice cover in the Arctic Ocean. *Geophysical Research Letters*, 33(8).

Sirevaag, A. (2009). Turbulent exchange coefficients for the ice/ocean interface in case of rapid melting. *Geophysical Research Letters*, 36(4).

Smedsrud, L. H., Esau, I., Ingvaldsen, R. B., Eldevik, T., Haugan, P. M., Li, C., Lien, V. S., Olsen, A., Omar, A. M., Otterå, O. H., Risebrobakken, B., Sandø, A. B., Semenov, V. A., and Sorokina, S. A. (2013). The role of the Barents Sea in the Arctic Climate System. *Reviews of Geophysics*, 5(2012).

Smedsrud, L. H., Halvorsen, M. H., Stroeve, J. C., Zhang, R., and Kloster, K. (2016). Fram Strait sea ice export variability and September Arctic sea ice extent over the last 80 years. *The Cryosphere Discuss.*, 2016:1–29.

Smedsrud, L. H., Ingvaldsen, R., Nilsen, J. E. Ø., and Skagseth, Ø. (2010). Heat in the Barents Sea: Transport, storage, and surface fluxes. *Ocean Science*, 6(1):219–234.

Smedsrud, L. H., Sirevaag, A., Kloster, K., Sorteberg, A., and Sandven, S. (2011). Recent wind driven high sea ice area export in the Fram Strait contributes to Arctic sea ice decline. *The Cryosphere*, 5(4):821–829.

Smedsrud, L. H., Sorteberg, A., and Kloster, K. (2008). Recent and future changes of the Arctic sea-ice cover. *Geophysical Research Letters*, 35(20).

Solomon, S. (2007). *Climate change 2007-the physical science basis: Working group I contribution to the fourth assessment report of the IPCC*, volume 4. Cambridge University Press.

Spielhagen, R. F., Werner, K., Sørensen, S. A., Zamelczyk, K., Kandiano, E., Budeus, G., Husum, K., Marchitto, T. M., and Hald, M. (2011). Enhanced modern heat transfer to the Arctic by warm Atlantic Water. *Science (New York, N.Y.)*, 331(6016):450–453.

Spreen, G., Kwok, R., and Menemenlis, D. (2011). Trends in Arctic sea ice drift and role of wind forcing: 1992-2009. *Geophysical Research Letters*, 38(19).

Stammerjohn, S., Massom, R., Rind, D., and Martinson, D. (2012). Regions of rapid sea ice change: An inter-hemispheric seasonal comparison. *Geophysical Research Letters*, 39(6).

Steele, M. (2003). PHC 2.1 Detailed Report. http://psc.apl.washington.edu/nonwp_projects/. Last accessed on May. 1st, 2016.

Steele, M. (2004). Circulation of summer Pacific halocline water in the Arctic Ocean. *Journal of Geophysical Research*, 109(C2).

Steele, M. and Boyd, T. (1998). Retreat of the cold halocline layer in the Arctic Ocean. *Journal of Geophysical Research: Oceans*, 103.

Steele, M., Ermold, W., and Zhang, J. (2011). Modeling the formation and fate of the near-surface temperature maximum in the Canadian Basin of the Arctic Ocean. *Journal of Geophysical Research*, 116(C11).

Steele, M. and Flato, G. M. (2000). Sea ice growth, melt, and modeling: A survey. In *The freshwater budget of the Arctic Ocean*, pages 549–587. Springer.

Steele, M., Mellor, G. L., and Mcphee, M. G. (1989). Role of the Molecular Sublayer in the Melting or Freezing of Sea Ice. *Journal of Physical Oceanography*, 19(1):139–147.

Steele, M., Morley, R., and Ermold, W. (2001). PHC3 Updated from: A global ocean hydrography with a high quality Arctic Ocean. *Journal of Climate*, 14(9):2079–2087.

Stefan, J. (1889). {Ü}ber einige probleme der theorie der w{ä}rmeleitung. *Sitzungber., Wien, Akad. Mat. Natur*, 98:473–484.

Stouffer, J. (1980). Sensitivity of a Global Climate Model to an Increase of CO2 Concentration in the Atmosphere. *Journal of Geophysical Research: Oceans*, 85(80):5529–5554.

Stroeve, J. C., Serreze, M. C., Holland, M. M., Kay, J. E., Malanik, J., and Barrett, A. P. (2011). The Arctic's rapidly shrinking sea ice cover: a research synthesis. *Climatic Change*, 110(3-4):1005–1027.

Sverdrup, H. (1931). *Hvorledes og Hvorfor med "Nautilus"*. Gyldendal Forlag, Oslo.

Swift, J. H., Jones, E. P., Aagaard, K., Carmack, E. C., Hingston, M., Macdonald, R. W., McLaughlin, F. A., and Perkin, R. G. (1997). Waters of the Makarov and Canada basins. *Deep Sea Research Part II: Topical Studies in Oceanography*, 44(8):1503–1529.

Talley, L., Pickard, G. L., Emery, W. J., and Swift, J. H. (2012). *Descriptive Physical Oceanography*. Elsevier, sixt edition.

Taylor, K. E., Stouffer, R. J., and Meehl, G. A. (2012). An overview of CMIP5 and the experiment design. *Bulletin of the American Meteorological Society*, 93(4):485–498.

Thomson, R. E. and Emery, W. J. (2004). *Data analysis methods in physical oceanography*. Newnes, second and edition.

Thorpe, S. A. (2007). *An introduction to ocean turbulence*. Cambridge University Press.

Tilling, R. L., Ridout, A., Shepherd, A., and Wingham, D. J. (2015). Increased Arctic sea ice volume after anomalously low melting in 2013. *Nature Geoscience*, 8(8):643–646.

Timmermans, M.-L. and Jayne, S. R. (2016). The Arctic Ocean Spices Up. *Journal of Physical Oceanography*, 46(4):1277–1284.

Timofeyev, V. T. (1964). Interaction of waters from the Arctic Ocean with those from the Atlantic and Pacific. In *Deep Sea Research and Oceanographic Abstracts*, volume 11, pages 265–274. Elsevier.

Timokhov, L. and Tanis, F. (1997). Environmental Working Group Joint U.S.-Russian Atlas of the Arctic Ocean, Version 1.

Untersteiner, N. (1964). Calculations of temperature regime and heat budget of sea ice in the central Arctic. *Journal of Geophysical Research*, 69(22):4755–4766.

Untersteiner, N. (1988). On the ice and heat balance in Fram Strait. *Journal of Geophysical Research: Oceans*, 93(C1):527–531.

van Linschoten, J. H. (1601). Map of Barentsz Voyages. *Journal of Jan Huygens van Linschoten*.

Weingartner, T., Aagaard, K., Woodgate, R., Danielson, S., Sasaki, Y., and Cavalieri, D. (2005). Circulation on the north central Chukchi Sea shelf. *Deep Sea Research Part II: Topical Studies in Oceanography*, 52(24-26):3150–3174.

Whitefield, J., Winsor, P., McClelland, J., and Menemenlis, D. (2015). A new river discharge and river temperature climatology data set for the pan-Arctic region. *Ocean Modelling*, 88.

Wilkins, G. H., Stefansson, V., Lake, S., Danenhower, S., Sverdrup, H. U., and Wilkins, J. (1931). *Under the North Pole: The Wilkins-Ellsworth Submarine Expedition*. Brewer, Warren & Putnam.

Woodgate, R. (2013). Arctic Ocean Circulation : Going Around At the Top Of the World. 4.

Woodgate, R. a., Aagaard, K., Muench, R. D., Gunn, J., Björk, G., Rudels, B., a.T Roach, and Schauer, U. (2001). The Arctic Ocean Boundary Current along the Eurasian slope and the adjacent Lomonosov Ridge: Water mass properties, transports and transformations from moored instruments. *Deep Sea Research Part I: Oceanographic Research Papers*, 48(8):1757–1792.

Woodgate, R. a., Aagaard, K., Swift, J. H., Falkner, K. K., and Smethie, W. M. (2005). Pacific ventilation of the Arctic Ocean's lower halocline by upwelling and diapycnal mixing over the continental margin. *Geophysical Research Letters*, 32(18).

Woodgate, R. a., Weingartner, T. J., and Lindsay, R. (2012). Observed increases in Bering Strait oceanic fluxes from the Pacific to the Arctic from 2001 to 2011 and their impacts on the Arctic Ocean water column. *Geophysical Research Letters*, 39(24).

Wu, L. X., Jing, Z., Riser, S., and Visbeck, M. (2011). Seasonal and spatial variations of Southern Ocean diapycnal mixing from Argo profiling floats. *Nature Geoscience*, 4(6):363–366.

Yen, Y.-C., Cheng, K. C., and Fukusako, S. (1991). A Review of Intrinsic Thermophysical Properties of Snow, Ice, Sea Ice, and Frost. *Northern Engineer*, 53(1):1–76.

Zhang, J., Lindsay, R., Steele, M., and Schweiger, A. (2008). What drove the dramatic retreat of arctic sea ice during summer 2007? *Geophysical Research Letters*, 35(11):L11505.

Zhang, R. (2015). Mechanisms for low-frequency variability of summer Arctic sea ice extent. *Proceedings of the National Academy of Sciences*, 112(15):4570–4575.

Zygmuntowska, M., Rampal, P., Ivanova, N., and Smedsrud, L. H. (2014). Uncertainties in Arctic sea ice thickness and volume: new estimates and implications for trends. *The Cryosphere*, 8(2):705–720.